PERPENDICULAR MAGNETIC ANISOTROPY MATERIALS FOR SPINTRONICS APPLICATIONS

HO PIN

NATIONAL UNIVERSITY OF SINGAPORE

2013

PERPENDICULAR MAGNETIC ANISOTROPY MATERIALS FOR SPINTRONICS APPLICATIONS
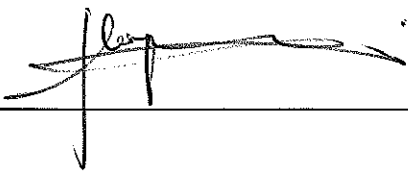
HO PIN

(B. Eng. (Hons.), NUS)

A THESIS SUBMITTED

FOR THE DOCTOR OF PHILOSOPHY

DEPARTMENT OF MATERIALS SCIENCE AND

ENGINEERING

NATIONAL UNIVERSITY OF SINGAPORE

2013

Declaration

I hereby declare that the thesis is my original work and it has been written by me in its entirety. I have duly acknowledged all the sources of information which have been used in the thesis.

This thesis has also not been submitted for any degree in any university previously.

Ho Pin

10 July 2013

ACKNOWLEDGEMENTS

Special thanks to my best friend Sherlyn who has been there to share my good and bad times and for the countless supportive gestures rendered through these years. Lastly, I would not have come this far without all my family members. A big thank you for constantly believing, encouraging and showing unwavering support for me throughout my life's journey. This thesis is dedicated to all of you.

TABLE OF CONTENTS

SUMMARY

Ferromagnetic materials with large perpendicular magnetic anisotropy (PMA) are increasingly investigated for future magnetic random access memory (MRAM) elements, especially in spin transfer torque MRAM (STT-MRAM), as they fulfill thermal stability at low dimensions in the nanometer range and lower the critical current density for STT switching. $L1_0$-FePt has received much attention as a potential candidate for such perpendicular systems due to its high magneto-anisotropy of 7×10^7 erg/cm^3. This thesis revolves around the study of high PMA $L1_0$-FePt in pseudo spin valves (PSVs).

Different spacer materials, Ag and TiN, were used in the $L1_0$-FePt based PSVs. The PSV with Ag spacer displayed a largest giant magnetoresistance (GMR) of 1.1 % which proved to be a significant improvement from the use of Au, Pt and Pd spacer materials reported earlier. The long spin diffusion length of Ag enabled larger spin accumulation, with reduced spin flip scattering at the $L1_0$-FePt/Ag interface, as compared to the other spacer materials. The interlayer diffusion within the $L1_0$-FePt/Ag/$L1_0$-FePt PSV, as a result of increasing Ag post-annealing temperature, had detrimental effects on the magnetic, interlayer coupling, reversal and spin-transport properties of the PSVs. Simulation work based on the Landau-Lifshitz-Gilbert atomistic and Landau-Lifshitz-Bloch micromagnetic models supported the experimental observations, where a greater extent of interlayer coupling between the $L1_0$-FePt layers with increasing interlayer diffusion led to a consequent reduction in magnetoresistance. The interlayer coupling was largely attributed to direct coupling via pinholes and magnetostatic coupling. In the non-uniformly magnetized $L1_0$-FePt layers, dipolar stray field coupling was also clearly observed. The stray fields emanating from

the reversed domains of one $L1_0$-FePt layer reduced the local nucleation field of the other $L1_0$-FePt layer, resulting in the preferential formation of reversed domains in the adjacent site. The use of TiN spacer material in $L1_0$-FePt based PSVs mitigated the interlayer diffusion issue as TiN was chemically stable towards FePt and was also a good diffusion barrier. As a result, the interlayer coupling effect arising from the pinholes, magnetostatic coupling and dipolar stray fields were greatly reduced. The PSVs with TiN spacer produced a maximum GMR of 0.78 %, which was achieved with a complete, three-dimensional continuous growth of $L1_0$-FePt and an optimized spacer thickness.

PSV structures which consisted of an ultra-thin ($\leq$ 4 nm) $L1_0$-FePt free layer were also demonstrated. An ultra-thin free layer is desirable for STT switching as a reduction in the free layer volume brings about a reduction in the STT critical current density. The PMA $L1_0$-FePt/Ag/[Co$_3$Pd$_8$]$_{30}$ PSV with ultra-thin $L1_0$-FePt free layer of 2 nm displayed a high $L1_0$-FePt perpendicular anisotropy of 2.21×10^7 erg/cm^3, high $L1_0$-FePt thermal stability of 84 and a GMR of 0.74 %.

LIST OF TABLES

LIST OF FIGURES

CONFERENCES, WORKSHOPS, PUBLICATIONS AND AWARDS

CONFERENCES AND WORKSHOPS

International Magnetics Conference (INTERMAG 2011), *Atomistic Modelling of the Interlayer Coupling Behaviour in Perpendicularly Magnetized $L1_0$-FePt/Ag/$L1_0$-FePt Pseudo Spin Valves*, Oral Presentation BD-05 (Taiwan, Taipei)

International Magnetics Conference (INTERMAG 2011), *Magnetic Properties of Cu Nanoclusters Embedded in ZnO Thin Films*, Poster Presentation FY-12 (Taiwan, Taipei)

Defence Research and Technology (DRTech) Workshop 2011, *Development of Magnetic Materials and Devices for Information Storage*, Poster Presentation (Singapore, Singapore)

Annual Conference on Magnetism and Magnetic Materials (MMM 2011), *Perpendicular $L1_0$-FePt Pseudo Spin Valve with Ag Spacer - Experimental and Simulation*, Poster Presentation FQ-06 (USA, Arizona)

Asia-Pacific Magnetic Recording Conference (APMRC 2012), *A comparative Study of Interlayer Coupling in $L1_0$-FePt Based Pseudo Spin Valves with Ag and TiN Spacers*, Poster Presentation (Singapore, Singapore)

PUBLICATIONS

P. Ho, G. C. Han, R. F. L. Evans, R. W. Chantrell, G. M. Chow, and J. S. Chen, *Perpendicular anisotropy $L1_0$-FePt based pseudo spin valve with Ag spacer layer*, Appl. Phys. Lett. 98, 132501 (2011)

P. Ho, G. C. Han, G. M. Chow, and J. S. Chen, *Interlayer magnetic coupling in perpendicular anisotropy $L1_0$-FePt based pseudo spin valve*, Appl. Phys. Lett. 98, 252503 (2011)

P. Ho, R. F. L. Evans, R. W. Chantrell, G. C. Han, G. M. Chow, and J. S. Chen, *Atomistic Modelling of the interlayer coupling behaviour in perpendicularly magnetized $L1_0$-FePt/Ag/$L1_0$-FePt pseudo spin valves*, IEEE Trans. Magn. 47, 2646 (2011)

P. Ho, R. F. L. Evans, R. W. Chantrell, G. C. Han, G. M. Chow, and J. S. Chen, *Micromagnetic modelling of $L1_0$-FePt/Ag/$L1_0$-FePt pseudo spin valves*, Appl. Phys.

Lett. 99, 162503 (2011) (Selected for republication in Virtual Journal of Nanoscience and Technology)

P. Ho, G. C. Han, K. H. He, G. M. Chow, and J. S. Chen, *(001) textured L1$_0$-FePt pseudo spin valve with TiN spacer*, Appl. Phys. Lett. 99, 252503 (2011)

P. Ho, G. C. Han, K. H. He, G. M. Chow, and J. S. Chen, *Effects of spacer thickness on perpendicular anisotropy L1$_0$-FePt/TiN/L1$_0$-FePt pseudo spin valves*, J. Appl. Phys. 111, 083909 (2012)

R. J. Tang, **P. Ho**, B. C. Lim, *Influence of Ru/Ru–SiO$_2$ underlayers on the microstructure and magnetic properties of CoPt–SiO$_2$ perpendicular recording media*, Thin Solid Films 518, 5813 (2010)

X. M. Liu, **P. Ho**, J. S. Chen, and A. O. Adeyeye, *Magnetization reversal and magnetoresistance behavior of perpendicularly magnetized [Co/Pd]$_4$/Au/[Co/Pd]$_2$ nanowires*, J. App. Phys. 112, 073902 (2012)

B. Y. Zong, **P. Ho**, G. C. Han, G. M. Chow, and J. S. Chen, *A simple approach to sub-100 nm resist nanopatterns with high aspect-ratio*, J. Micromech. Microeng. 23, 035038 (2013)

C. C. Toh, X. D. Liu, **P. Ho**, and J. S. Chen, *Magnetic properties of Cu nanoclusters embedded in ZnO thin films*, IEEE Trans. Magn. 47, 4003 (2011)

B. Y. Zong, Z. W. Pong, Y. P. Wu, **P. Ho**, J. J. Qiu, L. B. Kong, L. Wang and G. C. Han, *Electrodeposition of granular FeCoNi films with large permeability for microwave applications*, J. Mater. Chem. 21, 16042 (2011)

B. Y. Zong, J. Y. Goh, Z. B. Guo, P. Luo, C. C. Wang, J. J. Qiu, **P. Ho**, Y. J. Chen, M. S. Zhang and G. C. Han, *Fabrication of ultrahigh density metal-cell-metal crossbar memory devices with only two cycles of lithography and dry-etch procedures*, Nanotechnology 24, 245303 (2013)

P. Ho, R. F. L. Evans, R. W. Chantrell, G. C. Han, G. M. Chow, and J. S. Chen, *A study of perpendicular anisotropy L1$_0$-FePt pseudo spin valves using a micromagnetic trilayer model* – Submitted for review, Phys. Rev. B

<u>AWARDS</u>

Best Poster – Merit Award for IEEE Magnetics Society Singapore Chapter Poster Competition (students) 2011
Micromagnetic Modelling of $L1_0$-FePt/Ag/$L1_0$-FePt Pseudo Spin Valves

Best Poster – Merit Award for IEEE Magnetics Society Singapore Chapter Poster Competition (students) 2011
Development of Magnetic Materials and Devices for Information Storage

LIST OF ABBREVIATIONS

AF	antiferromagnetic
AFM	atomic force microscopy
AMR	anisotropic magnetoresistance
CIMS	current induced magnetization switching
CIP	current-in-plane
CMOS	complementary metal-oxide-semiconductor
CPP	current-perpendicular-to-plane
DC	direct current
DRAM	dynamic random access memory
EBL	electron beam lithography
FM	ferromagnetic
GMR	giant magnetoresistance
HDD	hard disk drive
HRTEM	high resolution transmission electron microscopy
HRXRD	high resolution x-ray diffraction
LLB	Landau-Lifshitz-Bloch
LLG	Landau-Lifshitz-Gilbert
MFM	magnetic force microscopy
MMR	magnon magnetoresistance
MR	magnetoresistance
MRAM	magnetic random access memory
MTJ	magnetic tunnel junction
NM	non-magnetic
PMA	perpendicular magnetic anisotropy
PPMS	physical properties measurement system
PSV	pseudo spin valve
RE-TM	rare earth-transition metal
RF	radio frequency
RKKY	Ruderman-Kittel-Kasuya-Yosida
RMS	root mean square
RSM	reciprocal space map

SAED	selected area electron diffraction
SEM	scanning electron microscopy
SFD	switching field distribution
SQUID	superconducting quantum interference device
SRAM	static random access memory
STS	spin transfer switching
STT	spin transfer torque
SV	spin valve
TMR	tunnelling magnetoresistance
TSF	thermal stability factor
VSM	vibrating sample magnetometer
XRD	x-ray diffraction

CHAPTER 1

1 INTRODUCTION

1.1 Overview of Spintronics

Spintronics, or spin electronics, is a new science which studies the properties of the electron spin for its integration into present day semiconductor technology. The incorporation of power and versatility of the spin dimension to conventional electronics devices promises a whole new range of commercial opportunities, especially in the data storage industry. Spintronics brings to attention a new paradigm shift where magnetic spins and electronic charges are no longer considered separate entities, unlike in the case of classical magnetic recording. Instead, spintronics utilizes the mutual influence of magnetization dynamics and charge current on one another and is on its way to providing a faster and lower energy means for transferring and storing information [1, 2].

One of the most prominent examples of the exploitation of the intrinsic spin of the electron and its associated magnetic moment is the Giant Magnetoresistance (GMR) effect, discovered by Grunberg and Fert in 1988. A trilayer structure, with a non-magnetic (NM) metallic layer sandwiched between two ferromagnetic (FM) layers, was found to be able to give a magnetoresistance (MR) value of 5-6 % when current was passed through it. This was a marked improvement of 2 to 10 times from the MR ratio produced by the anisotropic magnetoresistance (AMR) effect, first proposed by Lord Kelvin in 1857. The GMR effect paved the way for many present spin electronics data storage applications such as sensors and the magnetic random access memory (MRAM). Data storage industries constantly seek to

increase the MR ratio of the devices in order to equip them with higher read signals. In 1995, the development of the magnetic tunnel junctions (MTJs) produced an even higher MR ratio of approximately 10 %. Subsequent improvements detailed a surge in room temperature tunnelling magnetoresistance (TMR) ratio to 500 % [2].

The MRAM, which works on the principles of the GMR or TMR phenomenon, provides non-volatile data storage and has unlimited endurance and fast read/write speeds that no other non-volatile memories possess. Unfortunately, progress in the MRAM technology, based on the conventional current induced magnetic field switching, has been slow due to its lack of scalability beyond 256 Mbit. However, with the introduction of the spin transfer torque (STT) effect, hopes for areal density improvement as well as substantial operating power reduction in MRAM are revived [2, 3, 4, 5].

The idea of spin transfer torque was first introduced in 1996 when Slonczewski and Berger independently predicted that a spin polarized current flowing through a metallic magnetic multilayer was capable of inducing a spin transfer torque on the magnetization of a ferromagnetic layer. At the same time, Slonczewski postulated that either current induced magnetization switching (CIMS) or a steady state precession could result from the torque, depending on the device design and the magnitude of the applied magnetic field [3].

The integration of STT into GMR-based spin valves (SVs) and TMR-based MTJs for MRAM applications garnered tremendous interests as it meant that the areal density of MRAM is no longer constrained by the conventional magnetic field driven writing process. For the metallic multilayer SV, the advantage lies in its good conductivity which provides little resistance to sustain the current density

required for STT. On the other hand, the MTJ promises better compatibility with many Si-based electronics applications. However, the tunnel barriers have to be kept sufficiently thin to support STT [3]. The STT phenomenon in SVs and MTJs has been confirmed in numerous experiments and is heralded as a potential mechanism in next generation MRAM devices, where the conventional magnetic field driven writing process will be substituted [6-11]. The future moves towards garnering spin effects for magnetoresistive applications. A general perspective on the advancement of magnetoresistive devices is presented in Figure 1.1 [12].
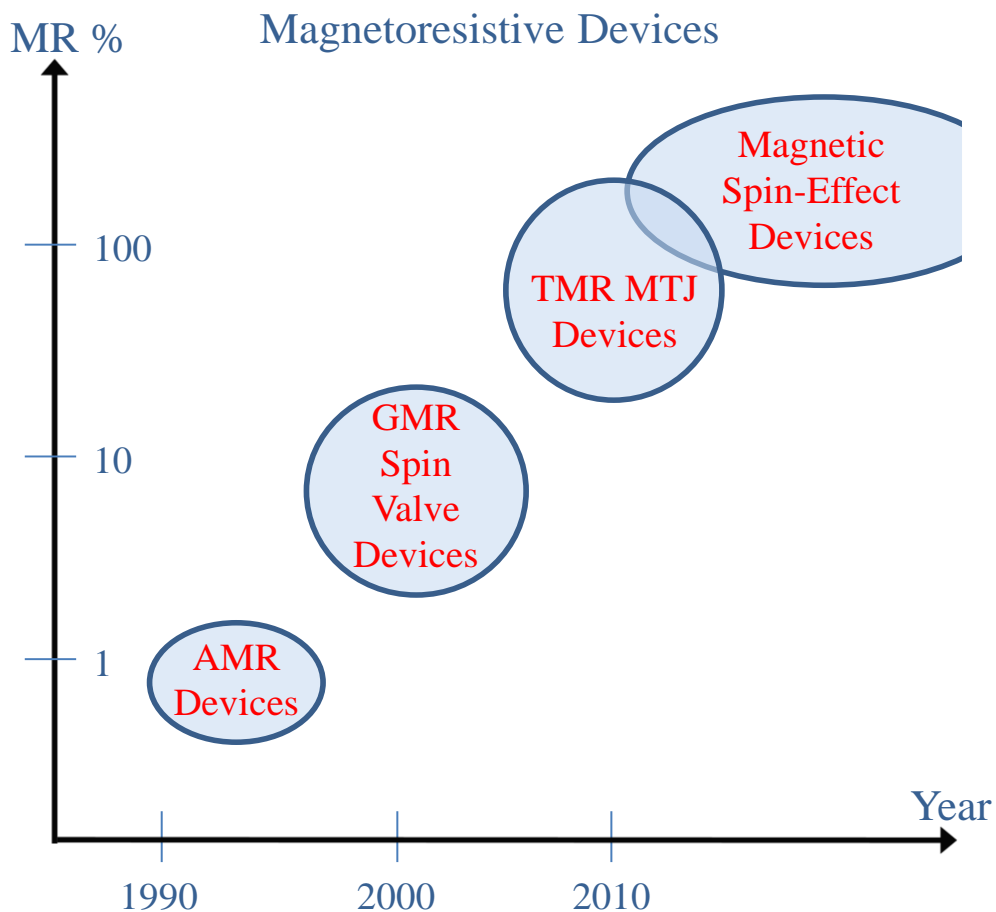
Figure 1.1   Advancement of magnetic devices for MRAM applications.

Besides MRAMs, the discovery of STT also sparked off much research interests in other commercial applications. For instance, the Racetrack Memory proposed by

IBM offers an alternative method of reading data where data is read as domains run through the reader by means of STT induced domain wall motion [3, 13]. Steady state magnetic precession induced by STT can also be utilized for high frequency applications such as microwave oscillators, detectors and phase shifters [3, 4, 13].

1.2 Giant Magnetoresistance and Spin Valve Configuration

SV-based memories make use of the GMR effect. A SV consists of a non-magnetic metal sandwiched between two FM layers. Independent switching of the free and fixed layers is ensured by the deliberate creation of larger anisotropy energy for the fixed layer and/or the pinning of the fixed FM layer using an antiferromagnetic (AF) layer. Pseudo spin valve (PSV) presents an alternative from the standard SV in that it does not have an AF layer to pin the fixed FM layer; rather two FM layers with different coercivities are used to control magnetization switching.

GMR can be qualitatively understood using the Mott model [14, 15]. Figure 1.2 shows a simple two current model and equivalent resistor network illustrating the GMR effect. In a parallel configuration, spin up electrons are totally unscattered when transmitted through both FM1 and FM2. Thus, conductivity is contributed by the spin up electrons channel. In the anti-parallel configuration, both the spin up and spin down electrons undergo scattering when they pass through FM2 and FM1, respectively. Neither the spin up nor spin down channel provides a low resistance pathway. This leads to an increased resistance compared to that of the parallel configuration.
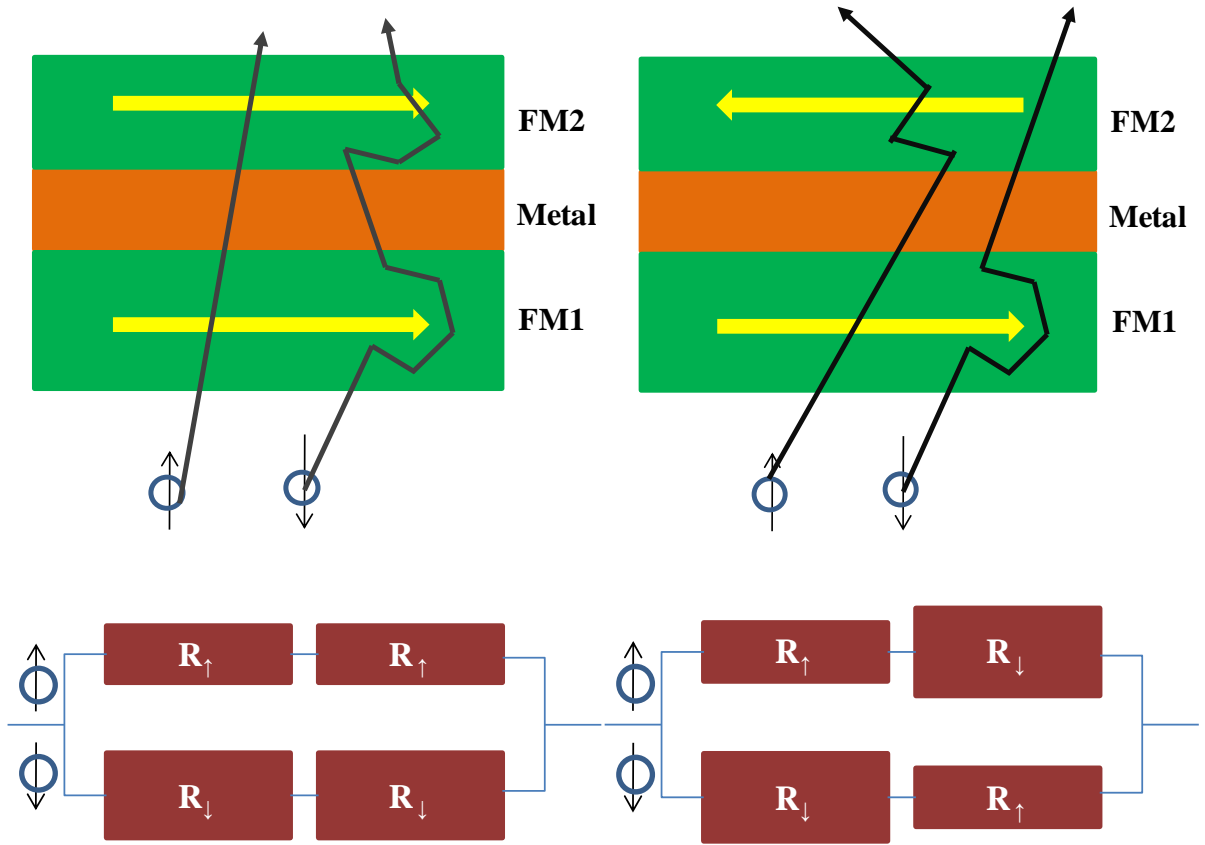
Figure 1.2   Schematic diagram of GMR for the parallel and anti-parallel configurations based on a simple resistor model.

The GMR ratio of the devices is determined by Equation (1.1)

$$GMR = \frac{R_{AP} - R_P}{R_P} = \frac{(R_\downarrow - R_\uparrow)^2}{4R_\uparrow R_\downarrow} \tag{1.1}$$

where R_{AP} and R_P are the resistance values in the anti-parallel and parallel alignment. Based on the Mott series-resistor model, R_P and R_{AP} are also represented by

$$R_P = \frac{2R_\uparrow R_\downarrow}{R_\uparrow + R_\downarrow} \qquad R_{AP} = \frac{R_\uparrow + R_\downarrow}{2} \tag{1.2}$$

where $R_\uparrow$ and $R_\downarrow$ are the resistance of the spin up and spin down electron channels, respectively.

Thus, with reference to Equation (1.1), the larger the spin asymmetry α ($\alpha \ll 1$ or $\alpha \gg 1$), which is the ratio of the resistivity of the spin down electrons to the spin up electrons, the higher the GMR.

The GMR effect is associated with the spin dependent bulk scattering of the FM layers and the spin dependent interfacial scattering at the ferromagnet/metal interfaces, which can be explained by the electronic band structure model. Their respective contributions depend on the thickness of the FM layers and the different channelling of the electrons in the different layers. The interface contribution is typically predominant for FM layers of a few nanometers thick, while the bulk contributions become larger for thickness exceeding the 5 to 10 nm range [16].

The bulk spin differential scattering of the FM layer is determined by the strength of the spin asymmetry α in the conductivity of the bulk FM metal. FM $3d$ metals are characterized by the presence of the $4s$, $4p$ and $3d$ valence states [14]. The d band is exchange split and the scattering properties of the majority spin up and minority spin down conduction electrons vastly differ as a result. For instance, for the ferromagnet Co, exchange splitting results in a fully occupied majority d band and partially occupied minority d band. This gives rise to a Fermi level which lies within the sp band for the majority electrons, thus exhibiting free electron like Fermi surface and high conductivity. On the other hand, the conductivity of the minority electrons is limited by the hybridized spd bands. As a result, bulk Co demonstrates strong spin asymmetry required to produce a high GMR.

At the ferromagnet/metal interface, the difference in the scattering probability of the opposite spins arises when the band structure energy mismatch at the ferromagnet/metal interface is present for one particular spin direction but not the

other. For instance, a good band matching at the ferromagnet/metal interface for the majority electrons but a poor band matching for the minority electrons promotes a high transmission of majority electrons and low transmission of the minority electrons across the interface, respectively [14]. Thus, majority electrons pass through the ferromagnet/metal interfaces easily when they are aligned while scattering of both majority and minority electrons takes place when the ferromagnet/metal interfaces are anti-aligned. Therefore, the spin dependent transmission/scattering of the electrons at the interface plays a crucial role in the resultant GMR.

In conjunction with the multiband band structure model for the GMR effect, Barnas *et al.* showed theoretically that the sign of the GMR is dependent on the nature of the interfacial and bulk spin asymmetry coefficient of the metal spacer and FM layers [17]. When the interfacial and bulk asymmetry coefficients at both the ferromagnet/metal interfaces and FM layers are all positive or all negative, the GMR obtained is normal and positive. Conversely, when both the interfacial asymmetry coefficient of the FM1/metal interface and the bulk asymmetry coefficient of the FM1 layer are of an opposite sign from that of the FM2/metal interface and FM2 layer, an inverse and negative GMR will result.

The GMR effect can be classified under two categories: current-in-plane (CIP) or current perpendicular-to-plane (CPP). In the CIP geometry, current flows in the plane of the layers. The mean free path λ of the electrons has to be larger than the total thickness of the layers so that the electrons can pass through all the layers successfully. It should be noted that the NM layers in the stack provide a current shunting path, which reduces the GMR as scattering within these layers are not spin dependent. For the CPP geometry where the current passes through

perpendicular to the layers and induces spin accumulation, the length scale of importance becomes the spin diffusion length [18]. It is crucial that the spin diffusion length l_{sf} is larger than the thicknesses of the layers to minimize spin independent flipping. The spin diffusion length is related to the mean free path as

$$l_{sf} \approx \sqrt{\frac{v_F \tau_{sf} \lambda}{3}} \qquad\qquad (1.3)$$

where v_F is the Femi velocity, τ_{sf} is the spin-flip relaxation, λ is the mean free path [11].

Unlike in the CIP configuration, there will not be current shunting in the CPP configuration as all the electrons must transverse through the magnetic layers. As such, the GMR ratio is expected to be much higher. However, the measurement of CPP devices is more challenging since it requires the fabrication of the thin film structures into nano or sub-micron scale devices [19]. The resistance of a CPP device is determined by the device pillar dimension in the CPP design, which includes the cross sectional area and the thickness of the SV film structure. The small thickness of the SV trilayer structure, typically less than 100 nm, will result in a low CPP resistance that is not easily detected. Thus, this has to be compensated with a significant reduction in the cross-sectional area of the pillar, so that a sufficiently large resistance can be detected.

1.3 Tunnelling Magnetoresistance and Magnetic Tunnel Junction

A MTJ consists of two FM electrodes separated by a thin non-magnetic insulating barrier. Classical electron transport theory does not occur in an insulator. Instead, the phenomenon of electron tunnelling takes place across the insulating barrier which is kept thin at 1 to 2 nm. When the insulating barrier is sufficiently thin, the

evanescent states in the barrier region do not decay totally but will emerge at the other end of the barrier [20]. Thus, a finite probability of electron waves tunnelling across the thin potential barrier is possible. This tunnelling probability, T_p, depends exponentially on the tunnel barrier thickness d and is described by the following relation:

$$T_P \propto e^{-\kappa d} \tag{1.4}$$

where the decay constant κ is the difference between the energy of the potential barrier and electron.

The difference in resistance between the parallel and anti-parallel configurations of the FM layers, when electrons tunnel through the FM layer/insulating barrier/FM layer, contributes to the TMR effect. This can be understood in terms of the Julliere's model, where the TMR effect is attributed to the spin selective tunnelling due to the spin dependent density of states [20-22]. According to this model, the tunnelling of spin up and spin down electrons, and thus conductance, occurs in two independent spin channels. Figure 1.3 shows that when the FM electrodes are in a parallel alignment, there are available empty states of the same spin orientation. Thus, both majority and minority electrons can tunnel through freely, giving rise to a low resistance. However in the anti-parallel system, very few empty states are available at the second FM layer for majority spin up electrons; while very few minority spin down electrons are present despite the large number of available spin down states at the second FM layer [21, 22]. This results in a higher resistance configuration.
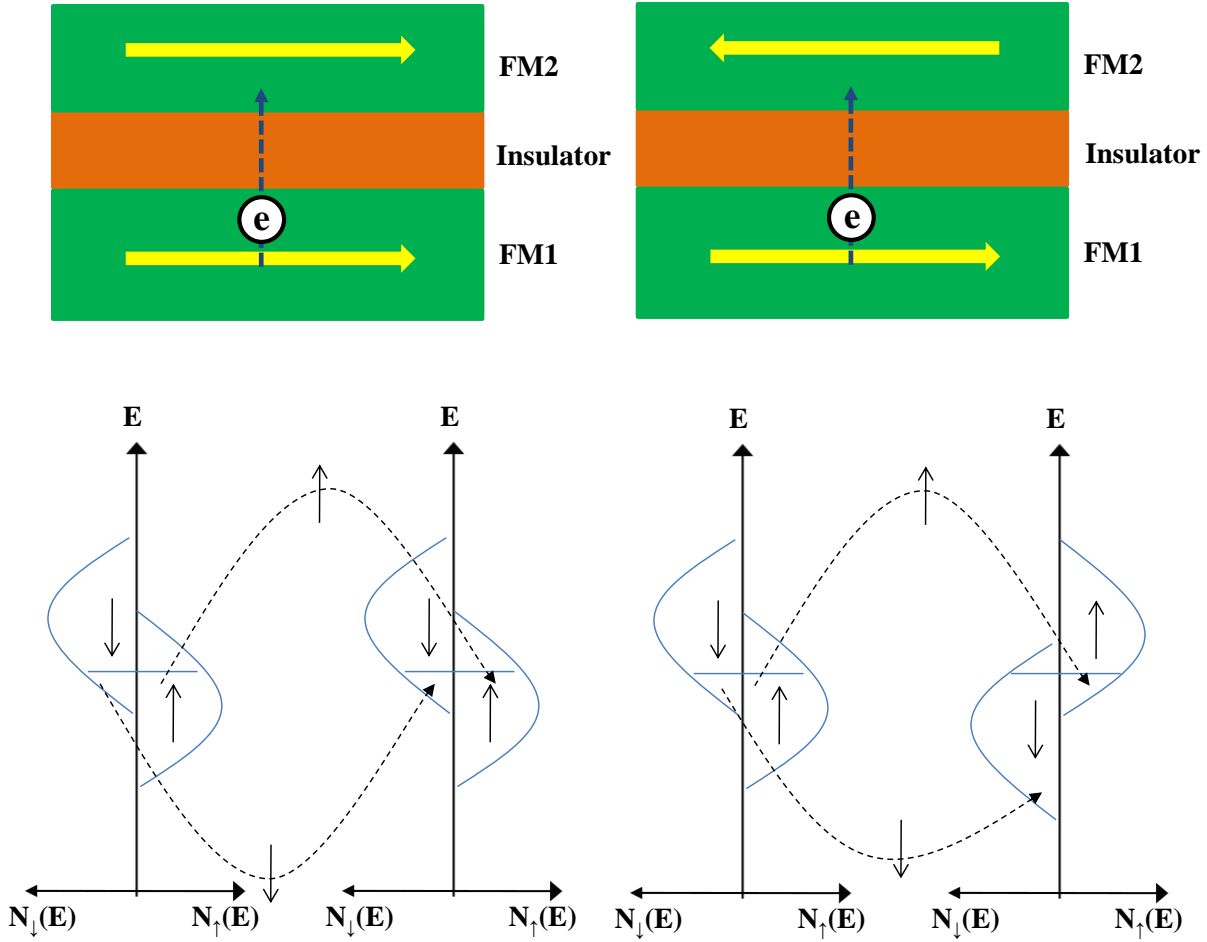
Figure 1.3   Schematic diagram of TMR for the parallel and anti-parallel configurations based on spin selective matching.

The TMR ratio of the devices is defined by Equation (1.5)

$$TMR = \frac{R_{AP} - R_P}{R_P} = \frac{2P_1 P_2}{1 - P_1 P_2} \tag{1.5}$$

where P_1 and P_2 are the spin polarizations of the FM layer 1 and FM layer 2, respectively. The spin polarization P of the FM layer is related to its effective density of states D at the Fermi energy level, defined as follows

$$P_\alpha = \frac{D_{\alpha\uparrow} - D_{\alpha\downarrow}}{D_{\alpha\uparrow} + D_{\alpha\downarrow}}, \ \alpha = 1, 2 \tag{1.6}$$

Earlier research on MTJs revealed that there are two main forms of tunnelling mechanisms, namely incoherent tunnelling and coherent tunnelling [23]. Incoherent tunnelling in MTJs occurs in the presence of an amorphous tunnel barrier while coherent tunnelling occurs in the presence of a crystalline barrier. The former has been demonstrated in MTJs with an amorphous Al-O barrier while the latter has been observed in an MgO (001) barrier as shown in Figure 1.4.

(a)   (b)
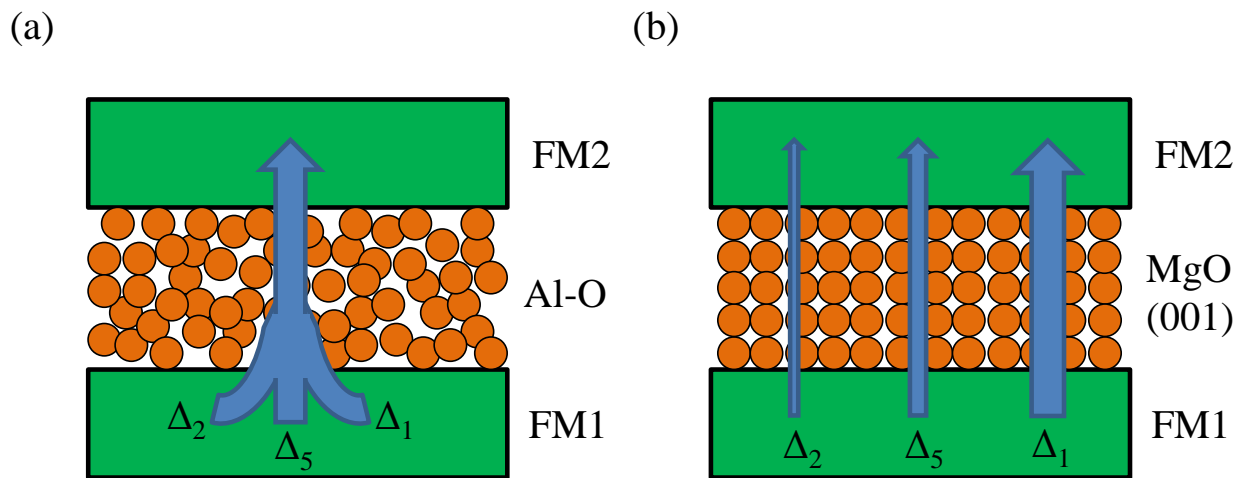
Figure 1.4 Schematic diagram of (a) incoherent tunnelling through amorphous Al-O barrier and (b) coherent tunnelling through crystalline MgO (001) barrier.

In the MTJ with an Al-O insulator, there exists no crystallographic symmetry in the amorphous Al-O tunnel barrier and thus Bloch states with various symmetries can couple with the evanescent states in Al-O [Figure 1.4(a)]. As such, the spin electrons from the different Bloch states of the FM layer tunnel incoherently through the barrier. The TMR effect, which arises from the incoherent tunnelling of conduction electrons through the amorphous Al-O barrier, is represented phenomenological by the Julliere's model. The Julliere's model describes the scenario of completely incoherent tunnelling, with the assumption that the tunnelling probabilities of all the Bloch states of the FM layer are the same.

However, it should be noted that the Bloch states of the FM metals or alloys typically display different symmetries and thus differing tunnelling probabilities.

A TMR of up to 70 % has been reported in MTJs with amorphous Al-O tunnel barrier [24] where incoherent tunnelling takes place. An improved TMR of 200 % was achieved with the alternative use of crystalline MgO (001) barrier sandwiched between Fe FM layers, which promoted coherent tunnelling [25]. An ideal coherent spin polarized tunnelling in an epitaxial MTJ with crystalline tunnel barrier is the key to obtaining the higher TMR. When the coherency of the electron wave functions is conserved during tunnelling, only conduction electrons with wave functions totally symmetrical with the barrier normal axis will display high tunnelling probability [Figure 1.4(b)][23]. The Bloch states with Δ_1, Δ_2 and Δ_5 symmetries are present in $3d$ FM metals and alloys. In ideal coherent tunnelling, the Δ_1 Bloch state is theoretically the dominant tunnelling channel. This is attributed to the fact that the Δ_1 Bloch states in the FM layer possess totally symmetrical characteristics with the MgO barrier normal [001] direction, in which the majority spin electrons in the Δ_1 band have states at the Fermi energy E_F while the minority spin electrons do not. Thus, the Δ_1 evanescent states in MgO exhibit the slowest decay and consequently the Δ_1 Bloch states of the FM layer has the highest spin polarization P. Hence, an enormous TMR effect is possible with the dominant tunnelling of the Bloch states with Δ_1 symmetry through the MgO (001) barrier. Achieving a giant TMR effect in the epitaxial crystalline MgO (001) barrier requires the fabrication of MTJs without pinholes and maintenance of clean FM layer/MgO barrier interfaces. Oxidation of the FM Fe layer, even on a monolayer scale, inhibits the effective coherent tunnelling of the Δ_1 Bloch states and significantly suppresses the TMR [26].

The MTJ has an advantage over the GMR-based device in MRAM due to its high MR which produces a high read-out signal as well as low resistance-area (RA) in which the impedance is compatible with the complementary metal-oxide-semiconductor (CMOS) fabrication. Nevertheless, GMR devices consisting of the SV or PSV structures are still intensely studied as they allow the understanding of new materials, structures and design.

1.4 Magnetic Random Access Memory (MRAM) Technology

A universal memory which possesses non-volatility, high speed, high density and endurance is essential for future generation of data storage technology. MRAM is developed as one of the potential candidates for such a universal memory. There have been intense efforts, especially by IBM and Infineon to develop MRAM to compete with other RAMs such as dynamic RAM (DRAM) and static RAM (SRAM). An ideal MRAM will be one that combines the speed of SRAM, the high density of DRAM and the intrinsic advantages of non-volatility, radiation hardness and endurance in MRAM. In 2006, the first MRAM product with a 4 Mbit memory was commercialized by Freescale [22, 27, 28].

Data in MRAM is stored in the form of the logic state "1" or "0" which corresponds to the anti-parallel and parallel configurations of the multilayer, respectively. Figure 1.5 shows a MRAM cross point architecture where the memory bits are seated at the intersection of the "bit" and "word" lines. The memory state of a selected memory bit can be altered when current is supplied through two particular arrays to generate an ampere-field at the cross point. The magnetic field generated from one wire itself is insufficient for the switching of the cell. Switching will only occur at the intersection point, where the two orthogonal

fields lower the switching field of the cell at the junction. Reading of data is based on their relative magnetoresistance where "1" has a higher MR and "0" has a lower MR [11, 22].
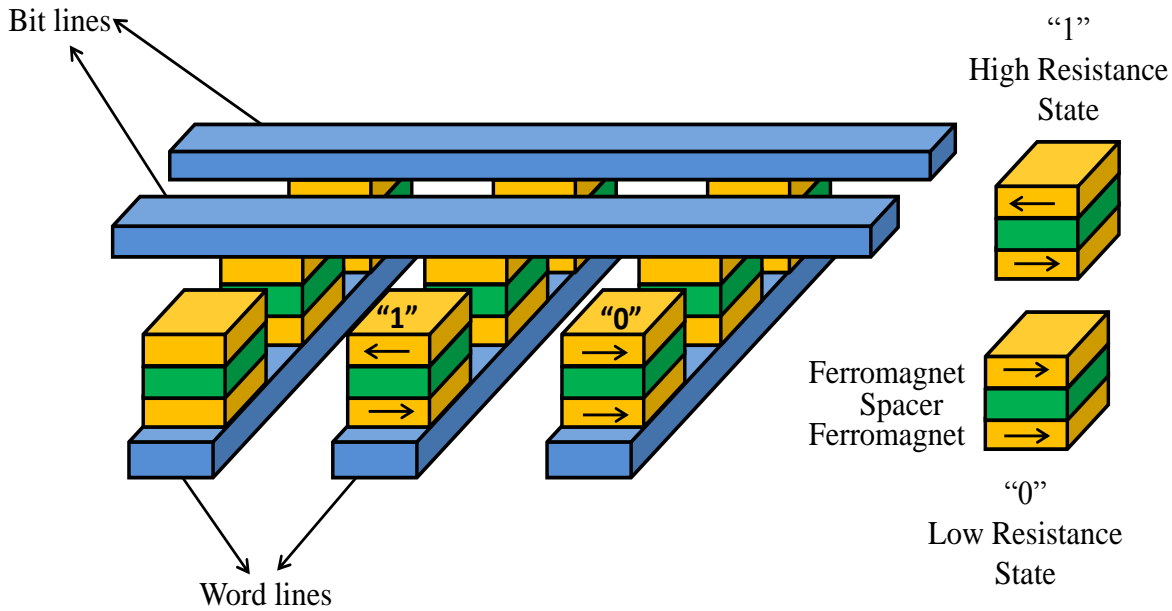
Figure 1.5   Cross point architecture for writing and reading in MRAM.

The memory state in MRAM is conventionally altered by a current induced magnetic field. For many years, this field induced switching method has hindered the progress in the MRAM technology. The influence of the current induced magnetic field on the neighbouring nano-magnetic bits imposed a limit on the size of the bit and the pitch size between the bits. Moreover, the current required to achieve the desirable switching field also increased with a reduction of the current line. These issues caused a limitation in the scalability of the MRAM devices to smaller sizes [29, 30]. In addition, some bits with lower magnetic switching field experienced "half-select" disturb switching problems. The switching field depended largely on the shape anisotropy of the bit, which varied significantly in a large memory array. As such, when a bit at the current line intersection is written

by the orthogonal current lines, bits along the same current lines with smaller shape anisotropy experienced undesirable disturbance switching [29]. This posed as another roadblock for the development of MRAM products.

1.5 Spin Transfer Torque MRAM (STT-MRAM)

A solution arrived with the discovery of the STT phenomenon, which uses current instead of the conventional current induced magnetic field to bring about a change in the memory state. Current induced switching promises an attractive method in fulfilling lower power requirements with increasing areal density in MRAM (Figure 1.6) [29-31].
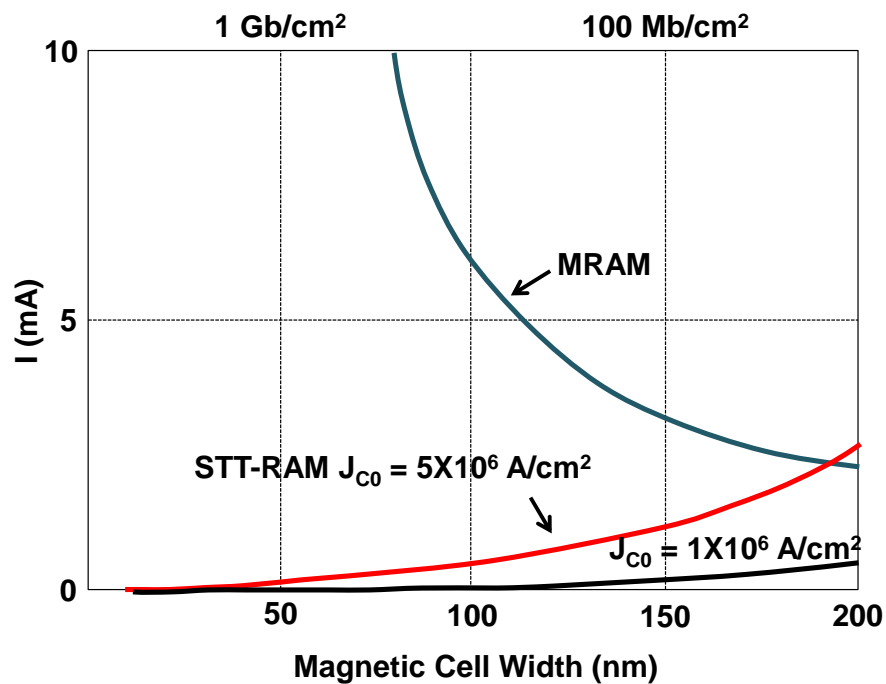
Figure 1.6   Comparison of the writing current scaling trends between MRAM and STT-MRAM.

A localized write current, unlike the current induced magnetic field, does not influence the neighbouring nanomagnetic bits. Hence, device size reduction is possible. Moreover, the critical current required for STT is proportional to the square of the dimension of the nanomagnetic bit [13]. Thus, the STT effect will

only become more prominent with size reduction and as such, bring about reduced power consumption. In addition, the use of STT-MRAM liberates the need for the "word line" as the read and write currents are both provided by a selection transistor. As a result, the "half select" disturbance problem can also be avoided as the current only flows to the bits to be written [29]. In November 2012, Everspin Technologies led the industry in commercializing the first 64 Mb STT-MRAM.

The STT switching technique demonstrates a clear path for the migration to smaller and denser MRAM products with lower power consumption. However, the device size reduction will not be possible without first satisfying the thermal stability criterion. MRAMs with in-plane anisotropy have been widely studied but in recent years, those with high perpendicular magnetic anisotropy (PMA) have received greater attention and are of immense research interests. Ferromagnetic materials with large PMA have been considered a candidate for future MRAM elements, especially for STT-MRAM, as they can fulfill the thermal stability at low dimensions of nanometre range and reduce the critical current density for STT switching [22]. Details regarding STT-MRAM and its key challenges will be elaborated in the following sections.

1.5.1   Working Principles – Macroscopic Viewpoint

To make use of spin transfer, one of the FM layers (free FM layer) has to respond to spin current and undergo magnetization rotation while the other FM layer (fixed FM layer) remains unchanged. The FM layers act as spin filters. The electrons passing through the first FM layer are spin polarized such that the majority electrons are in the same orientation as the magnetization of this FM layer (Figure 1.7).
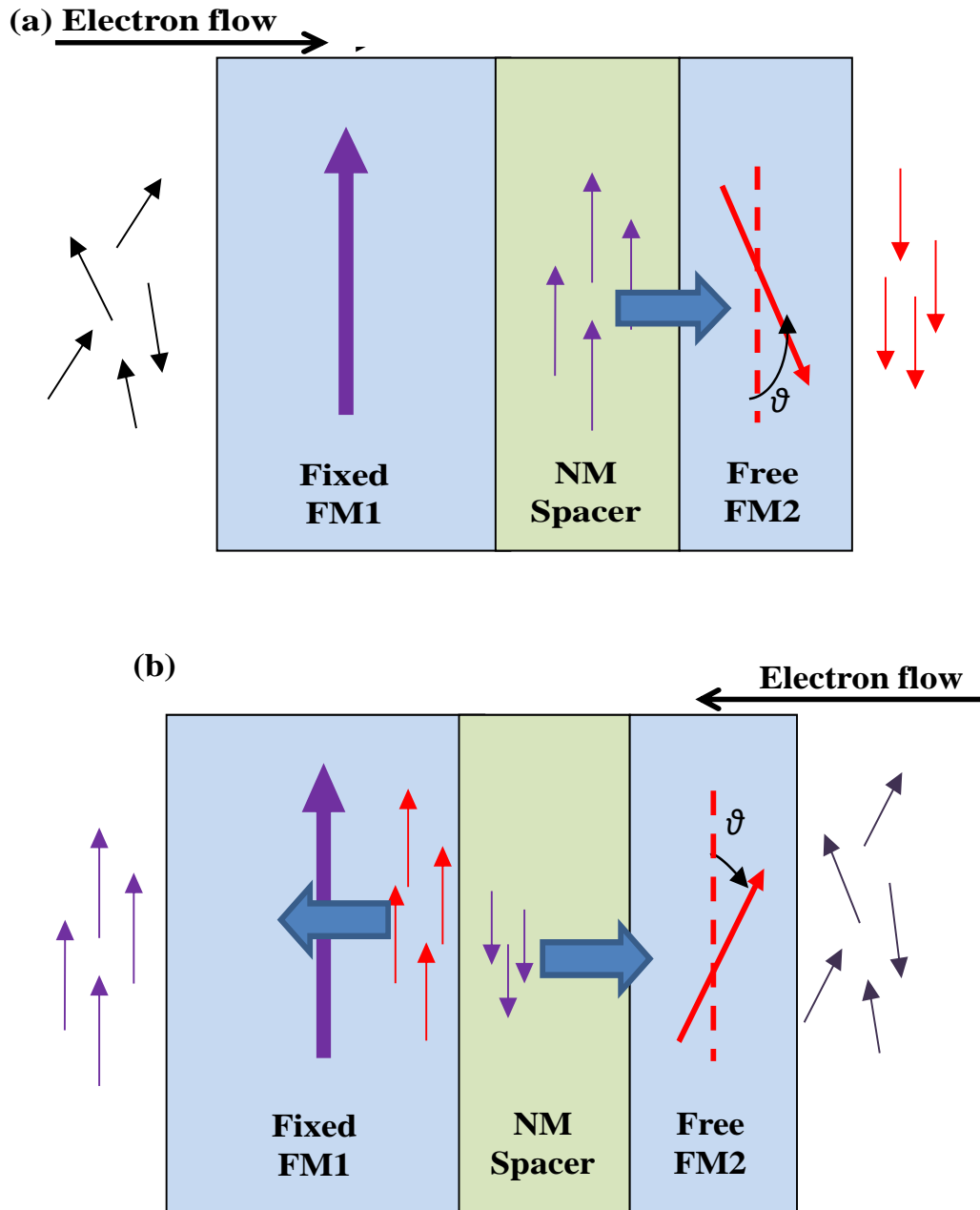
Figure 1.7   Schematic diagram of the STT on free layer contributed by (a) majority spin electrons resulting in anti-parallel (AP) → parallel (P) configuration and (b) scattered minority spin electrons resulting in P → AP.

When these spin polarized electrons impinge on the second FM layer with a different orientation, repolarization results via exchange interaction of the electron spins with the magnetization of the second FM layer. Thus, a torque is exerted on the electrons by the FM layer during repolarization. Taking into account the

conservation of angular momentum, a reaction torque is in turn exerted on the FM layer. If sufficient current is present, CIMS can occur. Figure 1.7(a) illustrates the spin transfer switching (STS) from the anti-parallel to parallel configuration. The torque contributed by the majority spin electrons is absorbed by the free FM layer, bringing about CIMS. On the other hand, in the case of STS from the parallel to anti-parallel configuration, current is applied in the opposite direction and the reflected minority electrons provide the torque for CIMS [Figure 1.7(b)] [5, 6, 12, 13, 32].

1.5.2   Working Principles – Microscopic Viewpoint

The spin dependent electron properties in ferromagnets allow them to induce a spin filter effect on an incoming current through exchange interaction. The splitting of the band structure energy creates an imbalance in the number of spin up and spin down electrons. Thus, a spin polarized current, and consequently a net magnetization, results when the incoming current passes through the first FM layer.

The polarized spin current consists of moving electron spins. Thus, there is a direction of flow in the real space as well as spin space. The STT effect is contributed by the transverse components of the spin current, which are the x and y axes perpendicular to the magnetization of the FM layer (Figure 1.8). As such, there is a partial loss of angular momentum in the transverse direction when polarized electrons enter the second FM layer. This is in turn absorbed by the FM layer as governed by the law of conservation of angular momentum. The rate of change of angular momentum of the magnetic moments in the FM layer gives rise to the STT. On the other hand, the z axis which is parallel to the magnetization of the FM layer serves as an axis for the precession of the spin in the oscillatory x and

y directions. The spin electrons experience no loss in angular momentum in this direction. Thus, the *z*-component of the spin current does not contribute to STT [2]. The incoming spin orientation has to be non-collinear with the magnetization of the free FM layer to create an angular momentum difference in the *x* and *y* axes and hence for STT to be observed. In the event that the orientation of the spin is collinear with the free FM layer, the FM layer is unable to induce any spin filtering effect. No differential scattering is present and thus no STT effect will be observed.
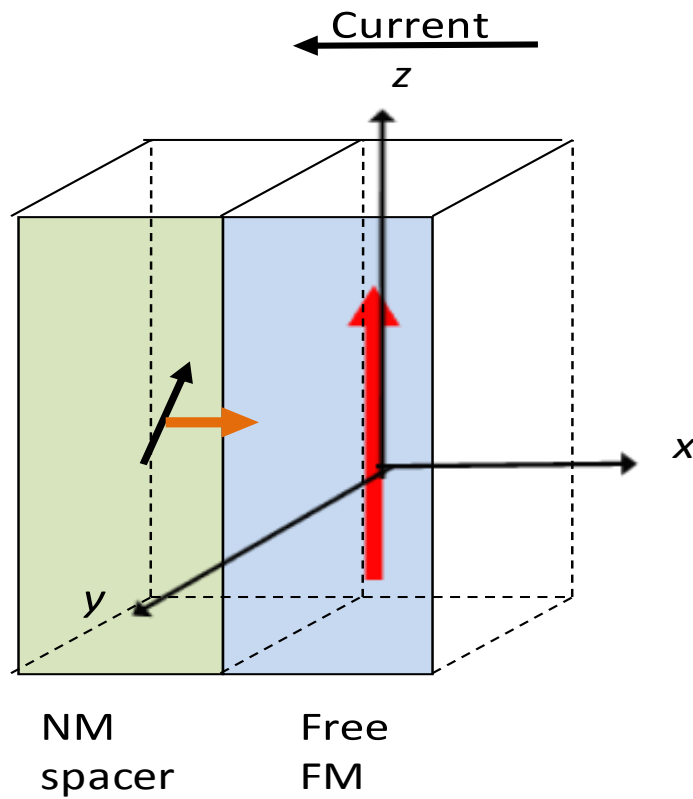
Figure 1.8   Illustration of a non-linear orientation of incoming spin current with the magnetization of the FM layer.

1.5.3   Landau-Lifshitz-Gilbert Description of STT

The Landau-Lifshitz-Gilbert (LLG) equation defines the magnetization reversal under a polarized current [3]

$$\frac{d\vec{m}_{free}}{dt} = -\gamma \vec{m}_{free} \times \vec{H}_{eff} + \alpha \vec{m}_{free} \times \frac{d\vec{m}_{free}}{dt} - \eta(\theta) \frac{\mu_B I}{eV} \vec{m}_{free} \times (\vec{m}_{free} \times \vec{m}_{fixed}) \quad (1.7)$$

where γ is the absolute value of the gyromagnetic factor $\frac{g\mu_B}{\hbar} \approx \frac{2\mu_B}{\hbar}$, $\vec{m}_{free}$ is the unit vector of the free layer magnetization, $\vec{H}_{eff}$ is the effective field, α is the damping constant, $\eta(\theta)$ represents the spin transfer efficiency dependent on layer structure and relative angle between the free and pinned layer θ, I is the applied current, V is the free layer volume and $\vec{m}_{fixed}$ is the unit vector of the fixed layer magnetization.

The first term $(-\gamma\vec{m}_{free} \times \vec{H}_{eff})$ is a precession term that describes the rotation of the magnetic moment around the applied field. The second term in the equation $(\alpha\vec{m}_{free} \times \frac{d\vec{m}_{free}}{dt})$ defines the damping torque which acts to bring the magnetic moment back to its lowest energy state in the direction of the applied field. The last term $[-\eta(\theta)\frac{\mu_B I}{eV}\vec{m}_{free} \times (\vec{m}_{free} \times \vec{m}_{fixed})]$ represents the STT which either acts with or against the damping torque depending on the direction of the applied current.

Figure 1.9 shows the different components defined by the LLG equation for a simplified model of magnetic dynamics in a FM layer. When both torques act in the same direction, the magnetic moment will align itself with the effective field. If the STT is equal but opposite to the damping torque, a steady state is attained where persistent precession emits spin waves. CIMS occurs when an opposite and sufficiently larger STT is present. Upon reaching a critical angle, there will be a drastic spiral of the magnetic moment away from the applied field orientation to the opposite direction.
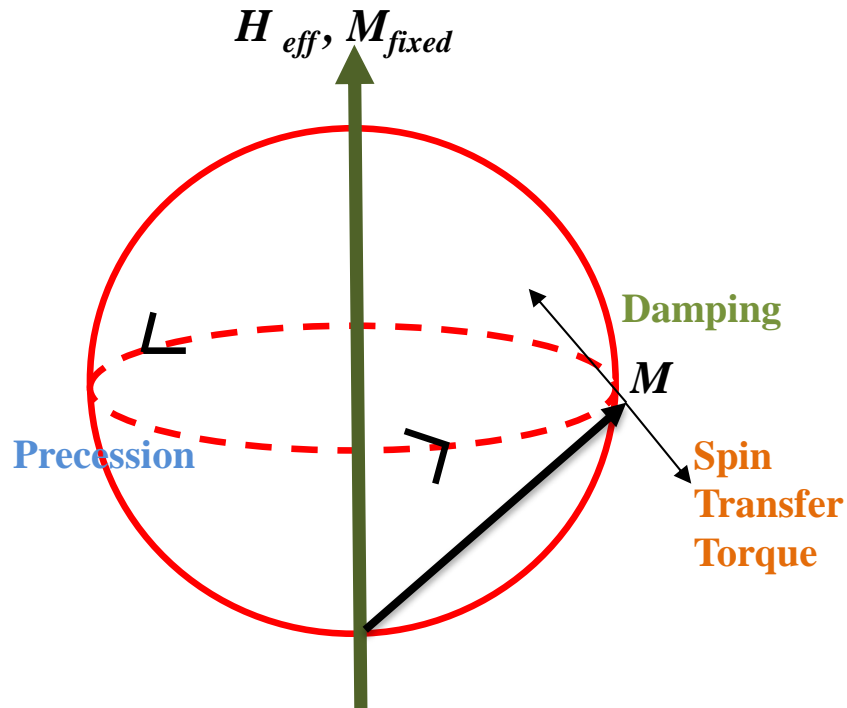
Figure 1.9 Directions of damping and STT vectors for a simplified model of magnetic dynamics in the FM layer.

1.5.4 Key Challenges in STT-MRAM

A key issue of the STT-MRAM technology has always been the reduction of the STT critical writing current of the nanomagnetic bit while maintaining its thermal stability to ensure data retention and hence minimal read/write error rates.

With increasing scalability, the volume V of the nanomagnetic switching element is reduced and this results in the subsequent decrease in the anisotropy energy barrier $K_u V$, where K_u is the magnetic anisotropy. Thermal energy $k_B T$, where k_B is the Boltzmann constant and T is the temperature, starts to compete with the anisotropy energy barrier. As a result, the magnetization moments are thermally excited and randomly reversed. This phenomenon of superparamagnetism is undesirable as it results in data losses. For the MRAM to be a useful data storage tool, a criterion of magnetic anisotropy energy of the order of 40 to $60 k_B T$ has been imposed on

MRAM cells. To solve the problem of superparamagnetism in in-plane anisotropy

MRAM, proposed solutions include the use of higher in-plane anisotropy materials

and an improvement in shape anisotropy field through the elongation of the

element shape [33].

Present values of the STT critical writing current density J_c lie in the range of 10^6

to 10^7 A/cm^2. The high current density carried through the bit line may exceed the

thermal failure threshold, leading to thermal management problems. Moreover,

critical current reduction brings about power saving. Thus, for effective integration

of the memory element into a CMOS circuit, a critical current reduction of close to

an order is essential. In the case of in-plane anisotropy STT, the linearized LLG

equation [Equation (1.7)] gives a zero temperature stability threshold current [21,

34]

$$I_c = \left(\frac{2e}{\hbar}\right)\left(\frac{\alpha M_s V}{\eta(\theta)}\right)(H + H_K + 2\pi M_s) \qquad (1.8)$$

where M_s is the saturation magnetization of the free layer, H is the external applied

field, H_k is the magnetic anisotropy field and $2\pi M_s$ is the demagnetization field. As

demonstrated in Equation (1.8), a higher K_u, and hence higher H_k, required for high

thermal stability of the bits, will concurrently bring about a higher J_c. A dilemma

of reducing the J_c while ensuring a sufficiently high thermal stability of the small

elements thus exists for in-plane anisotropy MRAM.

The use of an antiferromagnet with the free FM layer of the device has been

proposed to enhance the thermal stability without the need for higher in-plane

anisotropy materials [35]. At room temperature, the antiferromagnet improves

thermal stability by providing exchange biasing. During writing, the

22

antiferromagnet is heated above its Néel temperature and this lowers the critical current required to bring about STS of the free layer. Another promising approach in solving the J_c and thermal stability dilemma is the use of high PMA materials in STT-MRAM, which will be discussed in Section 1.5.5.

1.5.5   Advantages of PMA STT-MRAM

Based on Equation (1.8), significant contribution to the critical current for in-plane anisotropy STT also comes from the in-plane demagnetization field. The in-plane demagnetization field due to the thin film geometry in the nanomagnetic bits does not contribute to thermal stability but yet adds reluctance to STS [Figure 1.10(a)]. Spin transfer excitation in in-plane anisotropy MRAM involves significant out-of-plane precession of the spin. The presence of the demagnetization field impedes the out-of-plane precession. Hence, additional driving force supplied by the applied current is required to bring about CIMS [13].
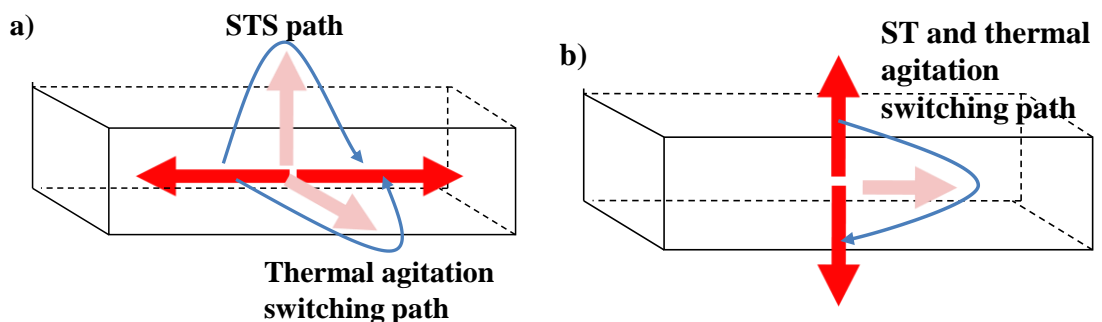
Figure 1.10 Switching paths in (a) in-plane and (b) perpendicular magnetic anisotropy devices.

On the other hand, this drawback does not exist in PMA MRAM. Unlike the case of in-plane anisotropy STT, thermal agitation and STS take the same path [Figure 1.10(b)] in the out-of-plane anisotropy design. The stability threshold current for PMA STT is now represented by [21, 34]

$$I_c = \left(\frac{2e}{\hbar}\right)\left(\frac{\alpha M_s V}{\eta(\theta)}\right)(H + H_K - 4\pi M_s) \qquad (1.9)$$

where $4\pi M_s$ is the demagnetization field arising from the perpendicular shape anisotropy. Thus, the easy plane demagnetization field, which is collinear with the perpendicular anisotropy field, will now assist in STS. As such, the use of a large PMA FM thin film in STT-MRAM permits high stability magnetization at room temperature which is important for long term data storage. At the same time, these out-of plane magnetization states are expected to be readily altered in the presence of an applied current as the demagnetization field assists in switching.

Another disadvantage of the in-plane anisotropy MRAM is that the nanomagnetic bits have to be shaped in non-symmetrical forms such as ellipses or rectangles. For MR to be detected, it requires that the magnetization of the FM layers be oriented almost collinearly in a parallel or anti-parallel configuration. However, in in-plane anisotropy materials, there exist an infinite number of easy axis orientations. Thus, deliberate construction of shape anisotropy is required to ensure that the magnetization of the FM layers lies in one preferred easy axis orientation. The shape sensitivity of the in-plane anisotropy devices poses a great challenge for the nano-scale fabrication process. On the other hand, for PMA STT devices, the presence of only one out-of-plane easy axis orientation frees the shape dependent constraint. Being able to come in symmetrical shapes of circles and squares also gives PMA STT devices an edge in improving areal density. In addition, reduced magnetic curling at the edges, a result of reduced interferences of the cells associated with PMA, also leads to greater magnetic uniformity.

1.5.6   PMA Materials in MRAM/STT-MRAM

There are four main classes of PMA materials employed in GMR or TMR devices (Table 1.1):

1) Complex multilayers based on Co, Fe and CoFe with Ni, Pt or Pd heavy non-magnetic elements;

2) Rare earth-transition metal (RE-TM) alloys such as TbFeCo and GdFeCo;

3) CoFeB-MgO systems with PMA;

4) Alloys such as $L1_0$-CoPt and $L1_0$-FePt.

Sputtered grown Co/Pd multilayer film with PMA was first reported by Carcia *et al.* [49]. Following this, there were extensive investigations on multilayer films such as $[Co/Pt]_n$, $[Co/Pd]_n$, $[Co/Ni]_n$ and $[CoFe/Pt]_n$ (n: alternation period) due to their relatively large PMA of $(3-9) \times 10^6$ erg/cm^3 which ensured thermal stability of the memory bits. In addition, the strong intergrain exchange coupling in $[Co/Pd]_n$ and $[Co/Pt]_n$ multilayer films promotes single domain magnetic layers, which provides the squareness and sharp switching properties required of GMR devices [50].

The origin of PMA in these Co based multilayer films was initially attributed to the Néel surface anisotropy, and more recently, linked to the interfacial anisotropy created by the lattice misfit strain between the layers [51-56]. Higher anisotropy could be obtained by increasing the number of bilayers, where the larger number of interfaces increases the interface induced anisotropy. The thermal stability of the layers will hence be improved by increasing the number of bilayers in the Co based films.

Table 1.1   Chronological summary of PMA MR devices.

Year Reported	SV or MTJ Structure (Thickness in nm. Order as such: free layer/spacer layer/fixed layer)	MR Ratio (%)	J_c (A/cm^2)
2006 [36]	[CoFe/Pt]$_5$/CoFe(0.5)/Cu(3)/[CoFe/Pt]$_7$	0.47 (CPP)	AP-P: 1.0×10^8 P-AP: -1.3×10^8
2006 [37]	Pt(3)/Co(0.25)/[Co/Ni]$_4$/Cu(4)/Co(0.1)/[Co/Ni]$_2$/Co(0.25)/[Co/Pt]$_4$/Pt(3)	1.0 (CPP)	AP-P: -2.6×10^7 P-AP: 7.5×10^7
2006 [8]	$L1_0$-FePt(4)/Au(5)/Fe(1)/$L1_0$-FePt(20)/Au(100)/Fe(1)	0.08 (CPP)	AP-P: -1.0×10^8
2008 [38]	GdFe(10)/Cu(6)/CoFe(1)/TbFeCo(20)	0.038 (CPP)	AP-P: 4.3×10^7 P-AP: -3.3×10^7
2008 [39]	TbCoFe(3)/CoFeB(1)/MgO(1)/CoFeB(2)/TbCoFe(30)	15 (CPP)	Ave: 4.7×10^6
2008 [40]	$L1_0$-FePt(3)/MgO(1.5)/Fe(2)/$L1_0$-FePt(10)	105 (TMR)	/
2008 [7]	[Fe/Pt]$_3$/Fe(0.29)/Au(2.7)/Fe(0.58)/[Fe/Pt]$_{12}$	1.1 (CPP)	Ave: 1.1×10^7
2009 [41]	$L1_0$-FePt(4)/Pt(2.4)/$L1_0$-FePt(5) $L1_0$-FePt(5)/Pd(3)/$L1_0$-FePt(5)	0.65 (CPP) 0.8 (CPP)	/
2010 [42]	[Co/Pt]$_6$/CoFeB(0.7)/CoFe(0.3)/MgO(1.1)/CoFe(0.4)/CoFeB(1.3)/TbFeCo(16)	60 (TMR)	/
2010 [43]	Pd(5)/[Co/Pd]$_2$/Co(0.6)/Cu(2)/Co(0.6)/[Co/Pd]$_{10}$/Pd(3)	6.2-6.5 (CIP)	/
2010 [44]	Ta(5)/Ru(10)/Ta(5)/CoFeB(1)/MgO(0.85)/CoFeB(1.7)/Ta(5)/Ru(5)	124 (TMR)	Ave: 3.9×10^6
2011 [45]	[Co/Ni]$_3$/Cu(2.2)/[Co/Ni]$_5$/TbCo(1.8)	6.8 (CIP)	/
2012 [46]	[Pd(1)/Co(0.38)]$_3$/Pd(0.6)/Co(0.38)/Cu(2.25)/Co(0.38)/[Pd(0.75)/Co(0.29)]$_4$	1.2 (CPP)	AP-P: -3.2×10^7 P-AP: 5.5×10^7
2012 [47]	CoFeB(2.25)/FeNiSiB(0.75)/MgO(1.4)CoFeB(3.6)	130 (TMR)	Ave: 2.3×10^6
2012 [48]	CoFeB(0.9)/MgO(0.9)/CoFeB(1.6)/Ta(0.4)/CoFeB(1.0)/MgO(0.9)	97 (TMR)	/

However, the consequent increase in the total layer thickness, and hence the resistance, will be detrimental to the magnetoresistance of the device. In addition, the free layer thickness also has to be kept thin to ensure a small critical current density J_c. The need for a thin free layer will thus compromise the thermal stability of the device. Interdiffusion also occurs between the Co and Pd/Pt layers at high temperatures, thereby altering the anisotropy of the multilayer film and adversely affecting the GMR of the device. This also deems Co based multilayer films unsuitable for practical applications which involve high operating temperatures generated from the STS writing currents [57, 58].

The next group of PMA materials, RE-TM alloys which are also used in magnetic recording, is adopted in the early stages of MRAM development due to their considerable PMA (in the range of 10^5 to 10^6 erg/cm^3 for TbFeCo) as well as large remanent squareness [59-61]. Another advantage is the simple deposition process of PMA TbCoFe film stacks at room temperature [39]. However, RE-TM alloys have poor spin polarization [62]. They also possess low corrosion resistance and thus, poor device reliability compared to structures that do not incorporate these rare earth elements [63, 64].

Another class of PMA materials is the CoFeB-MgO system, demonstrated by Ikeda *et al.* in 2010 [44]. The easy axis of CoFeB has an in-plane orientation at a thickness greater than 1.5 nm [30]. However, when an ultra-thin (< 1.5 nm) CoFeB/MgO film is grown, CoFeB displays strong interfacial perpendicular anisotropy. The CoFeB/MgO/CoFeB MTJ is capable of producing high TMR of over 120 % and low J_c of less than 4 MA/cm^2, while maintaining a considerable PMA of 2.1×10^6 erg/cm^3 at low device dimensions of 40 nm [44]. These combined characteristics of high MR signal and low J_c is advantageous for the

STT-MRAM. However, the scalability of the STT-MRAM with the use of CoFeB/MgO/CoFeB will eventually reach a bottleneck with its given PMA, where thermal instability of the bits occurs with bit size reduction, ultimately leading to superparamagnetism. Research in this material is still in its early stages and more studies, such as the thickness dependent characteristics of the CoFeB-MgO system and the optimization of the properties using different underlayers, have to be carried out to obtain a good trade-off between the MR signal, thermal stability and J_c.

A more established class of PMA materials with high K_u and thermal stability is the FePt and CoPt alloy films with $L1_0$ ordering. These have been widely studied and applied in magnetic recording devices. The spin orbit coupling of Pt and strong hybridization between the Pt $5d$ and Co or Fe $3d$ electronic states contribute to the high anisotropy along the [001] perpendicular out-of-plane direction. Thus, the $L1_0$-CoPt and $L1_0$-FePt films possess high K_u of up to 1.5×10^7 erg/cm^3 and 7×10^7 erg/cm^3, respectively [65, 66]. The $L1_0$-FePt, exhibiting the higher K_u of the two, is the FM material of interest for spintronics applications in this project. In its room temperature as-deposited form, FePt adopts a disordered face centre cubic ordering which is magnetically soft [67-69]. With annealing or high temperature deposition, the FePt undergoes a phase transition to the $L1_0$ form which possesses a very high K_u. As such, $L1_0$-FePt exhibits great versatility in offering a wide range of K_u selection as different degrees of magnetic ordering can be achieved by the careful control of the deposition temperature. Other means in which the K_u of the $L1_0$-FePt can be altered include the variation of the Fe and Pt compositions, the nature of the film (granular/continuous), the thickness of the FePt films, the underlayer material which the FePt film is grown on as well as the deposition

conditions such as the deposition pressure [70-78]. As discussed in Section 1.2 and 1.3, the principle of operation of the SV or MTJ is that each of the two FM layers has a different switching field, where the FM fixed layer typically has a much higher coercivity than the other FM free layer. The use of $L1_0$-FePt with well controlled growth conditions is thus able to fulfill the requirement of different switching fields for the fixed and free layer of the SVs and MTJs.

Due to the high PMA of $L1_0$-FePt, sufficiently high thermal stability can be achieved, even in the bits with minute cross-sectional dimensions, thus enhancing areal density. Riding on the promising advantage offered by $L1_0$-FePt with strong PMA, CPP-GMR pillars with Au spacer layer sandwiched between the two $L1_0$-FePt (001) FM layers were first demonstrated by Seki *et al.* [8]. A GMR of 0.08 % and a STT induced magnetization switching J_c of 1.0×10^8 A/cm^2 were achieved. Subsequent improvements made to increase the reading signal of the SV structure by means of the replacement of the spacer with Pt and Pd produced larger GMR values of 0.65 and 0.8 %, respectively [41]. In 2008, M. Yoshikawa *et al.* also reported the successful fabrication of $L1_0$-FePt MTJs with MgO spacer, which yielded a TMR of over 100 % using current-in-plane tunnelling measurements [40]. These have been summarized in Table 1.1.

Furthermore, the $L1_0$-FePt alloy film or super-lattice film, consisting of alternating monolayers of Fe and Pt, has PMA high enough to sustain an ultra-thin film thickness (< 4 nm) while maintaining sufficient thermal stability [7]. This is a competitive advantage over the Co-based multilayer film, which is unable to sustain a thin multilayer stack whilst achieving sufficiently high thermal stability; henceforth failing to fulfill the requirement of an ultra-thin free layer for the reduction of J_c in STT-MRAM. In addition, $L1_0$-FePt based devices possess higher

thermal reliability compared to those of Co-based multilayers as their properties are less affected by the high operating temperature or heat generated from the STS writing current [79]. In comparison with the CoFeB-MgO system, both the $L1_0$-FePt based MTJs and the CoFeB-MgO systems seemingly display comparable TMR signals of over 100 % and the ability to achieve thermally stable ultra-thin free layers. However, the $L1_0$-FePt remains a more competitive candidate due to its higher K_u, which enables future miniaturization of the STT-MRAM bits even when the CoFeB-MgO systems have reached a bottleneck in the areal density. Furthermore, $L1_0$-FePt also displays higher corrosion resistance compared to rare earth-transition metals. The fast STT switching speed of the $L1_0$-FePt alloy also deems it to be a suitable candidate for the free layer in STT-MRAM [80].

Despite the many advantages which the $L1_0$-FePt alloy presents, its spin transfer properties is largely constrained by the strong spin orbit scattering by the heavy Pt [81]. However, recent studies of the (111)-textured $L1_0$-FePt PSV with tilted magnetocrystalline anisotropy demonstrated enhanced interface spin polarization when thin CoFe spin polarizer layers were inserted at the spacer/FM layer interfaces. This resulted in an increase in GMR from 0.88 to 3.38 % [82]. The use of spin polarizers may thus be extended to PMA $L1_0$ (001)-oriented FePt to further increase the MR. As seen, $L1_0$-FePt remains a highly promising material for PMA devices over multilayer Co-based films and RE-TM and will be the focus of this project.

1.6 Motivation of Thesis

MRAM with high PMA holds great potential for future data storage applications as it provides an attractive alternative to improve the storage capacity and thermal stability of conventional MRAM. The objectives of the research work are listed as follows:

i)   Investigate the feasibility of high PMA $L1_0$-FePt based PSVs for spintronics applications.

ii) Study the characteristics of PMA $L1_0$-FePt based PSVs through an analysis of its magnetic, reversal, coupling, spin and magneto-transport behaviours.

iii) Introduce new materials or device structures to improve the performance of $L1_0$-FePt based PSVs.

iv) Design and develop theoretical simulation models vital for the understanding of the magnetic, reversal, coupling, spin and magneto-transport behaviors in the PSVs.

1.7 Organization of Thesis

In Chapter 1, a brief background and the working principles of the GMR and TMR effects are first being covered. An overview of the progress of the MRAM technology, highlighting the importance of STT and PMA materials in the GMR and TMR devices, is also being provided. The objectives of this thesis are subsequently established.

Chapter 2 summarizes the tools and techniques adopted in the fabrication of thin films, process fabrication of devices and the subsequent characterization of the samples.

Chapters 3 to 6 contain the key results and discussion of this research work. Chapter 3 begins with the study of the properties of a single layer $L1_0$-FePt, including its temperature and angular dependent magnetic and magneto-transport characteristics. These details are the backdrop for further understanding of the $L1_0$-FePt based PSVs in subsequent chapters.

Chapter 4 introduces Ag as a spacer material in the $L1_0$-FePt based PSVs. The effects of the Ag post annealing temperature on the properties of the PSVs are discussed. Atomistic and bilayer micromagnetic models are also used to supplement the experimental results.

Chapter 5 focuses on the use of TiN spacer material in the $L1_0$-FePt based PSVs. A trilayer micromagnetic model, which takes into account the physical presence of the spacer, is introduced to correlate the experimental and theoretical studies of the $L1_0$-FePt based PSVs with TiN spacer.

Chapter 6 covers the PSVs with ultra-thin $L1_0$-FePt, where a reduction in the free layer volume brings about a decrease in the STS critical current, thereby bringing experimental progress a step closer towards STT-MRAM.

Chapter 7 concludes the major findings contained in this thesis and offers recommendations on future work in the field of PMA materials for spintronics applications.

References

1.   J. F. Gregg, Nature Materials **6**, 798 (2007).

2.   C. Chappert, A. Fert and F. N. Van Dau, Nature Materials **6**, 813 (2007).

3.   D. C. Ralph and M. D. Stiles, J. Magn. Magn. Mater. **320**, 1190 (2008).

4.   V. Cros, O. Boulle, J. Grollier, A. Hamzić, M. Muñoz, L. G. Pereira, and F. Petroff, Comptes Rendus Physique **6**, 956 (2005).

5.   J. G. Zhu, IEEE. Trans. Magn. **96**, 1786 (2008).

6.   T. Seki, S. Mitani, K. Yakushiji, and K. Takanashi, J. Appl. Phys. **99**, 08G521 (2006).

7.   K. Yakushiji, S. Yuasa, T. Nagahama, A. Fukushima, H. Kubota, T. Katayama, and K. Ando, Appl. Phys. Exp. **1**, 0413021 (2008).

8.   T. Seki, S. Mitani, K. Yakushiji, and K. Takanashi, Appl. Phys. Lett. **89**, 172504 (2006).

9.   Y. Huai, A. Fert, P. Nguyen, M. Pakala and T. Valet, Appl. Phys. Lett. **84**, 3118 (2004).

10. G. D. Fuchs, N. C. Emley, I. N. Krivorotov, P. M. Braganca, E. M. Ryan, S. I. Kiselev, J. C. Sankey, D. C. Ralph, R. A. Buhrman and J. A. Katine, Appl. Phys. Lett. **85**, 1205 (2004).

11. S. M. Thompson, J. Phys. D: Appl. Phys. **41**, 093001 (2008).

12. J. E. Brewer and M. Gill, Nonvolatile Memory Technologies with Emphasis on Flash, pp. 678-689, (2007).

13. J. Z. Sun, IBM J. Res & Dev, **50**, 81 (2006).

14. E. Y. Tsymbal, D. G. Pettifor, and S. Maekawa, Giant Magnetoresistance: Theory, in *Handbook of Spin Transport and Magnetism*, edited by E. Y. Tsymbal, and I. Zutic (CRC Press, Boca Raton, 2012), 95-114.

15. N. F. Mott, Proc. R. Soc. A **153**, 368 (1936).

16. A. Fert, Giant Magnetoresistance, Scholarpedia 6(2):6982, (2011)

   http://www.scholarpedia.org/article/Giant_magnetoresistance, cited on 12/4/2013.

17. J. Barnaś, A. Fert, M. Gmitra, I. Weymann and V. K. Dugaev, Phys. Rev. B **72**, 024426 (2005).

18. T. Valet and A. Fert, Phys. Rev. B **48**, 7099 (1993).

19. E. Y. Tsymbal and D. G. Pettifor, Solid State Physics **56**, 113 (2001).

20. P. R. LeClair and J. S. Moodera, Tunneling Magnetoresistance: Experiment (Non-MgO Magnetic Tunnel Junctions), in *Handbook of Spin Transport and Magnetism*, edited by E. Y. Tsymbal and I. Zutic (CRC Press, Boca Raton, 2012), 197-216.

21. J. M. Slaughter, Annu. Rev. Mater. Res. **39**, 277 (2009).

22. R. P. Cowburn, Materials Today **6**, 32 (2003).

23. S. Yuasa, Tunneling Magnetoresistance: Experiment (MgO Magnetic Tunnel Junctions), in *Handbook of Spin Transport and Magnetism*, edited by E. Y. Tsymbal and I. Zutic (CRC Press, Boca Raton, 2012), 217-231.

24. D. Wang, C. Nordman, J. M. Daughton, Z. Qian, and J. Fink, IEEE Trans. Magn. **40** 2269 (2004).

25. S. Yuasa, T. Nagahama, A. Fukushima, Y. Suzuki, and K. Ando, Nature Materials **3**, 868 (2004).

26. X. G. Zhang, W. H. Butler, and A. Bandyopadhyay, Phys. Rev. B **68**, 092402 (2003)

27. T. Kim, S. J. Park, J. Noh, W. Park, I. Song, and Y. K. Kim, Phys. Stat. Sol (a) **201**, 1617 (2004).

28. S. Ikeda, J. Hayakawa, Y. M. Lee, F. Matsukura, Y. Ohno, T. Hanyu and H. Ohno, IEEE Trans. Elec. Dev. **54**, 945 (2007).

29. S. A. Wolf, J. Lu, and M. R. Stan, Proceedings of IEEE **98**, 2155 (2010).

30. R. Sbiaa, H. Meng, and S. N. Piramanayagam, Phys. Status Solidi RRL **5**, 413 (2011).

31. R. P. Cowburn, Nature Materials **6**, 255 (2007).

32. M. Tsoi, Nature Physics **4**, 17 (2008).

33. X. B. Wang, Y. R. Chen, H. Li, D. Dimitrov, and H. Liu, IEEE Trans. Magn. **44**, 2479 (2008).

34. H. Yoda, T. Kishi, T. Nagase, M. Yoshikawa, K. Nishiyama, E. Kitagawa, T. Daibou, M. Amano, N. Shimomura, S. Takahashi, T. Kai, M. Nakayama, H. Aikawa, S. Ikegawa, M. Nagamine, J. Ozeki, S. Mizukami, M. Oogane, Y. Ando, S. Yuasa, K. Yakushiji, H. Kubota, Y. Suzuki, Y. Nakatani, T. Miyazaki, and K. Ando, Curr. Appl. Phys. **10**, e87 (2010).

35. Z. H. Wu, C. H. Lai, S. H. Huang, and W. C. Lin, J. Magn. Magn. Mater. **304**, 93 (2006).

36. H. Meng and J. P. Wang, Appl. Phys. Lett. **88**, 172506 (2006).

37. S. Mangin, D. Ravelosona, J. A. Katine, M. J. Carey, B. D. Terris, and E. E. Fullerton, Nature Materials **5**, 210 (2006).

38. K. Aoshima, N. Funabashi, K. Machida, Y. Miyamoto, N. Kawamura, K. Kuga, N. Shimidzu, T. Kimura, Y. Otani, and F. Sato, IEEE. Trans. Magn. **44**, 2491 (2008).

39. M. Nakayama, T. Kai, N. Shimomura, M. Amano, E. Kitagawa, T. Nagase, M. Yoshikawa, T. Kishi, S. Ikegawa, and H. Yoda, J. Appl. Phys. **103**, 07A710 (2008).

40. M. Yoshikawa, E. Kitagawa, T. Nagase, T. Daibou, M. Nagamine, K. Nishiyama, T, Kishi, and H. Yoda, IEEE. Trans. Magn. **44**, 2573 (2008).

41. A. P. Mihai, J. P. Attané, L. Vila, C. Beigné, J. C. Pillet and A. Marty, Appl. Phys. Lett. **94**, 122509 (2009).

42. K. Yakushiji, K. Noma, T. Saruya, H. Kubota, A. Fukushima, T. Nagahama, S. Yuasa, and K. Ando, Appl. Phys. Exp. **3**, 053003 (2010).

43. T. Tahmasebi, S. N. Piramanayagam, R. Sbiaa, R. Law, and T. C. Chong, IEEE Trans, Magn. **46**, 1933 (2010).

44. S. Ikeda, K. Miura, H. Yamamoto, K. Mizunuma, H. D. Gan, M. Endo, S. Kanai, J. Hayakawa, F. Matsukura, and H. Ohno, Nature Materials **9**, 721 (2010).

45. J. Liao, H. He, Z. Zhang, B. Ma, and Q. Y. Jin, J. Appl. Phys. **109**, 023907 (2011).

46. N. Thiyagarajah, K. Lee, and S. Bae, J. Appl. Phys. **111**, 07C910 (2012).

47. D. H. Kim, J. U. Cho, S. Y. Park, S. Isogami, M. Tsunoda, M. Takahashi, E. E. Fullerton, and Y. K. Kim, J. Appl. Phys. **111**, 093913 (2012).

48. H. Sato, M. Yamanouchi, S. Ikeda, S. Fukami, and F. Matsukura, Appl. Phys. Lett. **101**, 022414-1 (2012).

49. P. F. Carcia, A. D. Meinhalt, and A. Suna, Appl. Phys. Lett. **47**, 178 (1985).

50. J. Kawaji, T. Asahi, T. Onoue, J. Sayama, J. Hokkyo, T. Osakaa, and K. Ouchi, J. Magn. Magn. Mat. **251**, 220 (2002).

51. T. Onoue, J. Kawaji, K. Kuramochi, T. Asahi, and T. Osaka, J. Magn. Magn. Mater. **235**, 82 (2001).

52. S. Mifuji, H. Sakuma, and K. Ishii, J. Appl. Phys. **97**, 10N102 (2005).

53. S. K. Kim, J. W. Lee, J. R. Jeong, J. Kim, and S. C. Shin, Appl. Phys. Lett. **79**, 1652 (2001).

54. F. J. A. den Broeder, W. Hoving, and P. J. H. Bloemen, J. Magn. Magn. Mater. **93**, 562 (1991).

55. S. K. Kim, and S. C. Shin, J. Appl. Phys. **89**, 3055 (2001).

56. M. T. Johnson, P. J. H. Bloemen, F. J. A den Broeder, and J. J de Veries, Rep. Prog. Phys. **59**, 1409 (1996).

57. K. Yakushiji, T. Saruya, H. Kubota, A. Fukushima, T. Nagahama, S. Yuasa, and K. Ando, Appl. Phys. Lett. **97**, 232508 (2010).

58. E. Chunsheng, J. Rantschler, S. Zhang, S. Khizroev, T. R. Lee, and D. Litvinov, J. Appl. Phys. **103**, 07B510 (2008).

59. G. W. Qin, Y. P. Ren, N. Xiao, B. Yang, L. Zuo and K. Oikawa, International Materials Reviews **54**, 157 (2009).

60. L. You, T. Kato, S. Tsunashima, and S. Iwata, J. Magn. Magn. Mat. **321**, 1015 (2009).

61. V. A. Seredkin, S. V. Stolyar, G. I. Frolov, and V. Yu. Yakovchuk, Tech. Phys. Lett. **30**, 820 (2004).

62. T. Hatori, and S. Nakagawa, J. Magn. Magn. Mat. **310**, 1657 (2007).

63. M. Seifert, V. Neu, and L. Schultz, Appl. Phys. Lett **94**, 022501 (2009).

64. C. M. Lee, L. X. Ye, J. M. Lee, W. L. Chen, C. Y. Huang, G. Chem, and T. H. Wu, IEEE. Trans. Magn. **45**, 3808 (2009).

65. H. Shima, K. Oikawa, A. Fujita, K. Fukamichi, K. Ishida, S. Nakamura, and T. Nojima, J. Magn. Magn. Mater. **290-291**, 566 (2005).

66. J. S. Chen, J. F. Hu, B. C Lim, B. Liu, G. M. Chow, and G. Ju, J. Appl. Phys. **103**, 07F517 (2008).

67. B. M. Lairson, M. R. Visokay, R. Sinclair, and B. M. Clemens, Appl. Phys. Lett. **62**, 639 (1993).

68.   M. R. Visokay and R. Sinclair, Appl. Phys. Lett. **66**, 1692 (1995).

69.   R. A. Ristau, K. Barmak, L. H. Lewis, K. R. Coffy, and J. K. Howard, J. Appl. Phys. **86**, 4527 (1999).

70.   C. M. Kuo, P. C. Kuo, and H. C. Wu, J. Appl. Phys. **85**, 2264 (1999).

71.   A. C. C. Yu, M. Mizuno, Y. Sasaki, and H. Kondo, Appl. Phys. Lett. **85**, 6242 (2004).

72.   M. F. Toney, W. Y. Lee, J. A. Hedstrom, and A. Kellock, J. Appl. Phys. **93**, 9902 (2003).

73.   T. Shima, K. Takanashi, Y.K. Takahashi, and K. Hono, Appl. Phys. Lett. **85**, 1050 (2004).

74.   W. B. Mi, J. J. Shen, W. J. Lu, and H. L. Bai, J. Alloys Compd. **503**, 233 (2010).

75.   Y. N. Hsu, S. Jeong, D. E. Laughlin, and D. N. Lambeth, J. Magn. Magn. Mat. **260**, 282 (2003).

76.   Y. F. Ding, J. S. Chen, E. Liu, C. J. Sun, and G. M. Chow, J. Appl. Phys. **97**, 10H303 (2005).

77.   A. C. Sun, J. H. Hsu, H. L. Huang, and P. C. Kuo, J. Magn. Magn. Mat. **304**, 106 (2006).

78.   J. S. Chen, B.C. Lim, J.F. Hu, Y.K. Lim, B. Liu, and G.M. Chow, Appl. Phys. Lett. **90**, 042508 (2007).

79.   S. Yoshimura, S. Omiya, G. Egawa, H. Saito, J. Bai, J. Phys.: Conference Series **266**, 012114 (2011).

80.   P. Sabareesan, and M. Daniel, J. Magn. Magn. Mat. **324**, 4219 (2012).

81.   A. D. Kent, Nature Materials **9**, 699 (2010).

82.   C. L. Zha, J. Nogues, and J. Akerman, J. IEEE. Trans. Magn. **45**, 3881 (2009).

CHAPTER 2

2 EXPERIMENTAL DETAILS

2.1 Sample Preparation

2.1.1 Magnetron Sputtering

Magnetron sputtering has the advantages of high deposition rate, good adhesion and allows the deposition of both conductive and insulating materials via direct current (DC) and radio frequency (RF) mode, respectively. In this thesis, all the films are prepared using an ultra-high vacuum magnetron sputtering system with a base pressure better than 10^{-7} Torr. Sputtering is carried out in the presence of 99.99 % pure Ar gas at a flow rate of 20 sccm. The sputtering power, pressure and temperature are optimized for each layer in the PSVs and MTJs to obtain the desired crystallographic and magnetic properties.

2.2 Device Fabrication

2.2.1 Lithography

An Elionix ELS-7000 electron beam lithography (EBL) system with acceleration voltage of 100 kV and electron beam diameter of 1.8 nm is used for the electron beam exposure of the resist nano-patterns. The negative tone MaN-2402 resist is selected for defining the resist nano-patterns and is subsequently developed with the maD-525 solution. The autocad software is used to design the patterns, which are then converted into a file compatible with the Red Hat Linux 7.3 operation system of the EBL system. The EBL chip size, number of dots in each chip, dosage time and power are optimized for each EBL exposure. Prior to the EBL exposure,

field correction has to be carried out to correct the width, rotation and distortion of the beam scanning area to ensure highly precise stitching exposure of the neighbouring chips.

2.2.2 Etching

Methods of thin film etching include chemical wet etching, reactive ion etching and ion milling [1]. For the device fabrication in this thesis, ion milling is used. During ion milling, high energy Ar ions are directed at the sample surface, removing atoms on the surface through momentum-energy transfer. This method of ion milling etches metals and oxides at a faster rate than carbon and organic materials. Thus, the negative tone MaN-2402 resists acts as a mask to prevent the patterns beneath it from being etched away. The ion etching angle is optimized for each process to ensure minimal re-deposition on the edge or sidewalls of the structures.

2.3 Characterization Tools

2.3.1 Vibrating Sample Magnetometer (VSM)

The room temperature out-of-plane and in-plane magnetic properties of the $L1_0$-FePt films, PSVs and MTJs are characterized by the Vibrating Sample Magnetometer (VSM). In VSM, a magnetized sample sits in the open part of the magnetic circuit and is subjected to a vibrating force [2, 3]. The change in the magnetic flux density induces a voltage in the pickup coil. This induced voltage is proportional to the magnetic moment of the sample. As a result, hysteresis loops of magnetic moment against applied field (M-H) at constant temperature are attained.

The combination of VSM with a four point probe allows angular dependent MR measurements to be recorded. VSM provides the rotational capability as well as the sweeping magnetic field. The four point probe technique uses pogo spring probes to measure the MR of the un-patterned PSVs.

2.3.2   Superconducting Quantum Interference Device (SQUID)

The Superconducting Quantum Interference Device (SQUID) is used to measure the low temperature out-of plane and in-plane magnetic properties of the $L1_0$-FePt thin films. The working principle of SQUID is based on the Josephson effect. The magnetic flux of the sample detected by the pick-up coil of the superconducting loop results in a critical current which oscillates as a function of the flux [4]. This corresponding voltage is also a function of the magnetic field and oscillates with the same period. The magnetic flux is then calculated based on the number of oscillations of the voltage.

2.3.3   Physical Properties Measurement System (PPMS)

The MR properties of the samples are measured by the Physical Properties Measurement System (PPMS). The PPMS is a versatile system which allows a wide range of characterization techniques ranging from magnetic, thermal to electrical measurements. The sample is mounted onto a chip carrier where the electrode pads are aluminium wire bonded to the electrical leads on the chip carrier. A sweeping out-of-plane field (maximum applied field possible: 70 kOe) is applied while the resistance of the devices is measured.

2.3.4   Atomic/Magnetic Force Microscopy (AFM/MFM)

The Atomic Force Microscopy (AFM) measures the surface roughness and morphology of the thin film layers. During the AFM tapping mode measurement, a fine tip comes into close contact with the sample surface and oscillates up and down near its resonance frequency [5]. The short-range Van der Waals forces of the sample surface cause the oscillation amplitude to decrease with increased proximity to the sample surface. As such, a topographical image of the region of interest is produced by imaging the force of the intermittent contact of the tip with the sample surface.

The Magnetic Force Microscopy (MFM) detects and maps out the magnetic domains of the $L1_0$-FePt layers. In contrast to the AFM, the MFM makes use of a magnetized cantilever [5, 6]. Long-range magnetic forces emanating from the magnetic structure shift the resonance frequency of the cantilever. A magnetic image is thus formed based on the resonance frequencies detected at every point over the scanned region.

2.3.5   Scanning Electron Microscopy (SEM)

The Scanning Electron Microscopy (SEM) is another technique to obtain information on the growth mechanism and surface morphology of the thin films. The SEM images a selected area of the sample surface by collecting signals mainly from the secondary and back-scattered electrons, which are generated when the focused high energy primary electron beam interacts with the sample. The two dimensional image formed by the secondary electrons provides details on the surface topography such as the shape and sizes of the grains.

2.3.6 High Resolution Transmission Electron Microscopy (HRTEM)

The microstructures of the multilayer films are studied using the Transmission Electron Microscopy (TEM). The TEM provides images based on the transmission and interaction of the beam of electrons with the thin specimen [7, 8]. The parallel beam of electrons which passes through the sample is scattered in different directions by the atoms. The transmitted electron beam then forms the bright field image. Cross-sectional bright field TEM images are used to observe the interface, imperfections and epitaxial growth of the thin film layers in the PSVs and MTJs. In addition, the diffracted electron beam can also provide crystallographic data through the selected area electron diffraction (SAED) spectrum, which is a two dimensional array of spots that corresponds to different sets of planes in the single crystal.

2.3.7 High Resolution X-ray Diffraction (HRXRD)

X-ray Diffraction (XRD) is predominantly used to investigate the crystallographic properties of the polycrystalline thin films [9]. This non-destructive method is based on the elastic scattering of x-rays and only those planes which fulfill Bragg's law ($n\lambda = 2d\sin\theta$) are detected. The θ-2θ scan, where the incident beam makes an angle of θ with the film surface and 2θ with the diffracted beam, is used to detect the planes which are parallel to the sample surface. The diffracted beams at each 2θ are indexed by comparing the peak positions with the data base provided by the Joint Committee on Powdered Diffraction Standard (JCPDS).

Reciprocal space maps (RSMs) are also derived from the HRXRD [9]. A reciprocal space map of the diffracted intensity is obtained by systematically scanning θ and 2θ to give a θ-2θ scan and varying the incident angle ω with the detector fixed at

2θ to give a ω-scan. A large number of ω-2θ scans are carried out for a range of incident angles ω. The intensity distribution in the ω-scan direction provides details on the mosaicity spread for the same interplanar spacing in the lattice. On the other hand, the intensity distribution in the θ-2θ scan indicates interplanar spacing variations for the same orientation.

The RSMs measured in the specular and off-specular directions also serve to shed light on the strain behavior of a multilayer structure (Figure 2.1).

(a)

(011)
(001)
Relaxed Film

Film

Substrate

(b)

Strained Film
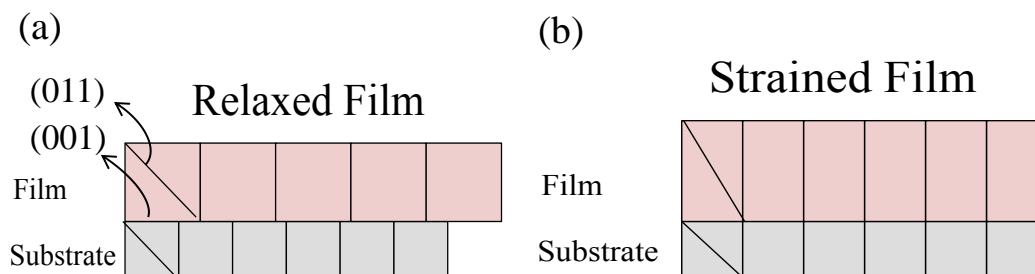
Film

Substrate

Figure 2.1   Schematic diagrams showing the thin film in a (a) fully relaxed and (b) fully strained state.

In the specular (001) plane, for both the relaxed and strained state, reflections from the film and substrate will lie along the same [001] direction since $(001)_{sub}$ is parallel to $(001)_{film}$. However, for the off-axis (011) plane, the relaxed and strained state will yield different outcomes as $(011)_{sub}$ is parallel to $(011)_{film}$ in the relaxed state but not in the strained state. Taking the substrate as the reference, in the fully strained state, the (011) reflection from the film will not lie along the same [011] direction of the substrate because both planes are not parallel. On the other hand, in the fully relaxed state, both the film and the substrate peaks will lie along the same [011] direction of the substrate as both planes are now parallel.

References

1.   Z. B. Guo and Y. H. Wu, Magnetic Nanostructures, (American Scientific Publishers, California, 2009), Chapter 16 pg. 585.

2.   S. Chikazumi, *Physics of Ferromagnetism*, (Oxford University Press, New York, 1997), Chapter 2 pg. 45.

3.   B. D. Cullity and C. D. Graham, *Introduction to Magnetic Materials*, (Wiley, Canada, 2009), Chapter 2 pg. 67.

4.   B. D. Cullity and C. D. Graham, *Introduction to Magnetic Materials*, (Wiley, Canada, 2009), Chapter 2 pg. 73.

5.   P. Grutter, H. J. Mamin, and D. Rugar, Scanning Tunneling Microscopy II, (Springer-Verlag, Berlin, 1992) pg. 151.

6.   A. Carl and E. F. Wassermann, Magnetic Nanostructures, (American Scientific Publishers, California, 2009), Chapter 2 pg. 68.

7.   L. Reimer, and H. Kohl, *Transmission Electron Microscopy: Physics of Image Formation*, (Springer, New York, 2008), Chapter 1 pg. 1.

8.   D. B. Williams, and C. B. Carter, *Transmission Electron Microscopy: A textbook for Materials Science*, (Plenum Press, New York, 1996).

9.   M. Birkholz, *Thin Film Analysis by X-Ray Scattering*, (Wiley-VCH, Weinheim, 2006).

CHAPTER 3

3 PERPENDICULAR MAGNETIC ANISOTROPY $L1_0$-FePt SINGLE LAYER FILM

The primary motivation of this research thesis is the integration of high PMA $L1_0$-FePt into the SV/MTJ system for spintronics application. Achieving SVs/MTJs with well exchange decoupled $L1_0$-FePt FM layers necessitates the stringent requirements of smooth and continuous $L1_0$-FePt layers of different K_u as well as minimal interlayer diffusion of $L1_0$-FePt into the spacer. The growth of high PMA $L1_0$-FePt films requires high temperature deposition and/or post annealing. $L1_0$-FePt films with varying degrees of magnetic ordering, and thus K_u, can be achieved with different deposition and/or post-annealing temperatures. This high temperature treatment affects the crystallographic structure, surface morphology, magnetic and magneto-transport properties of FePt, which ultimately plays a role in determining the performance of the SVs/MTJs. In this chapter, a fundamental study of the properties of a single layer FePt film with relation to its deposition temperature will be examined. The $Fe_{50}Pt_{50}$ film, with nominal thickness of 20 nm, was deposited on single crystal (001)-textured MgO substrate using magnetron sputtering system at varying substrate temperatures of 150, 250, 350 and 450 °C. Further investigation into the temperature and angular dependent properties of the PMA $L1_0$-FePt film deposited at 450 °C will be carried out. This will provide a detailed understanding of the characteristics of the single layer PMA $L1_0$-FePt film before moving on to the $L1_0$-FePt based PSVs in Chapters 4 to 6.

3.1 Effects of FePt Deposition Temperature

3.1.1 Crystallographic Properties

With increasing deposition temperature from 150 to 450 °C, there was an increasingly sharper superlattice FePt (001) peak compared to the fundamental FePt (002) peak (Figure 3.1). The presence of the FePt (001) peak is usually forbidden according to the calculation of the structure factor for the fcc crystal lattices. Thus, the observation of an increasingly sharper superlattice FePt (001) with respect to the FePt (002) peak indicated the increasing preferential ordering of the alternating α and β planes. A greater volume of fct FePt was formed from the fcc FePt with increasing deposition temperature, which provided energy for the expansion of the lattice constant a and shrinkage of lattice constant c.
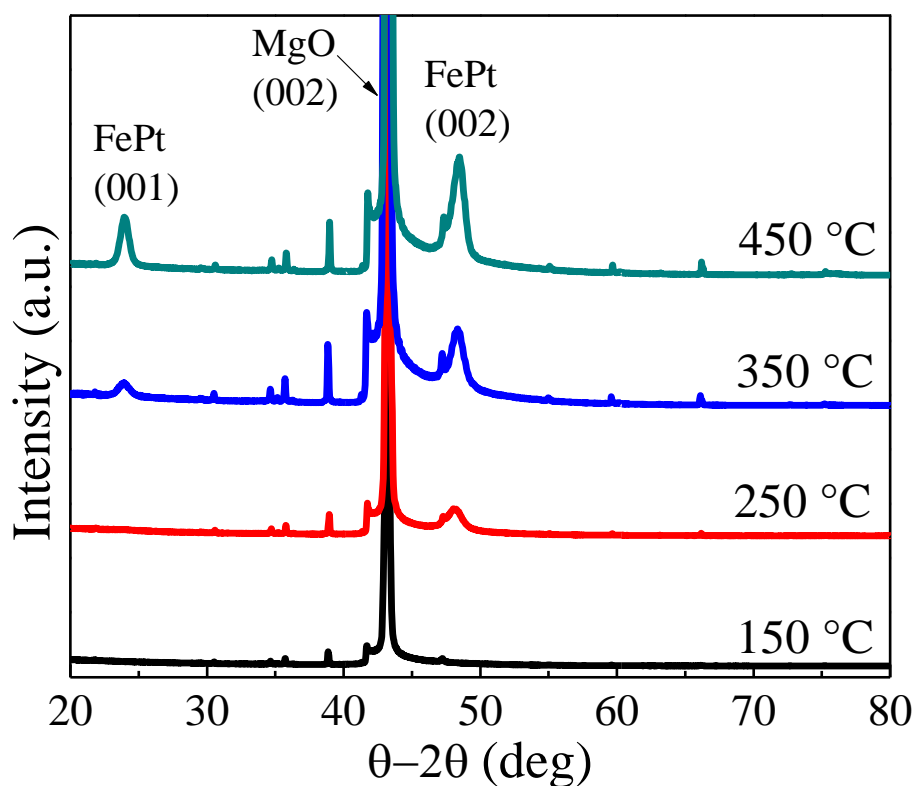
Figure 3.1 XRD spectrums of the FePt films deposited at different temperatures. The remaining unlabelled sharp peaks are inherent of the MgO substrate.

The extent of ordering can be represented by the ordering parameter S [1],

$$S \propto \left(\frac{I_{001}}{I_{002}}\right)^{\frac{1}{2}}$$

(3.1)

where I_{001} and I_{002} are the integrated intensities of the (001) and (002) peaks, respectively. A highest $\frac{I_{001}}{I_{002}}$ and consequently S was obtained for the FePt film deposited at the highest temperature of 450 °C.

3.1.2 Surface Morphology

With increasing FePt deposition temperature, the FePt grains were found to coagulate into bigger interconnected dense strip grains due to the increased surface mobility (Figure 3.2). As a result of the bigger grains, the surface roughness of the FePt films also increased (Figure 3.3).
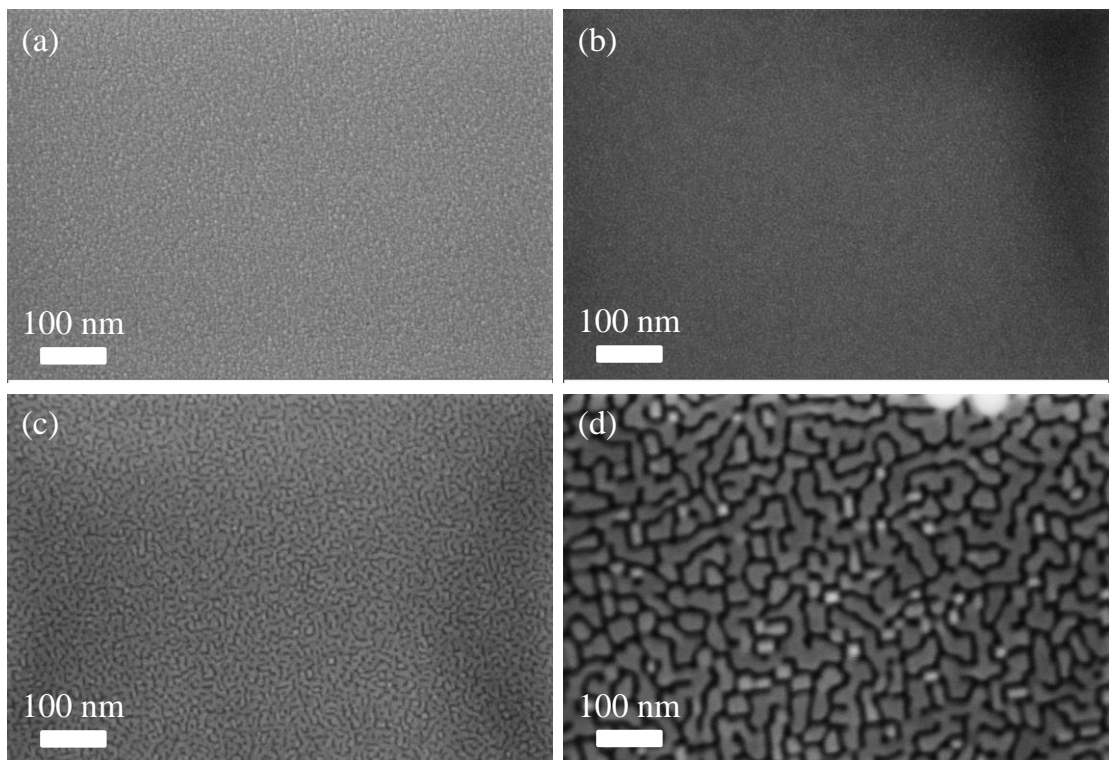
Figure 3.2 SEM images of FePt grown on MgO substrate with deposition temperatures of (a) 150, (b) 250, (c) 350 and (d) 450 °C.

(a)

R_{RMS}:0.4 nm

(b)

R_{RMS}:0.4 nm

(c)

R_{RMS}:0.5 nm

(d)

R_{RMS}:1.8 nm
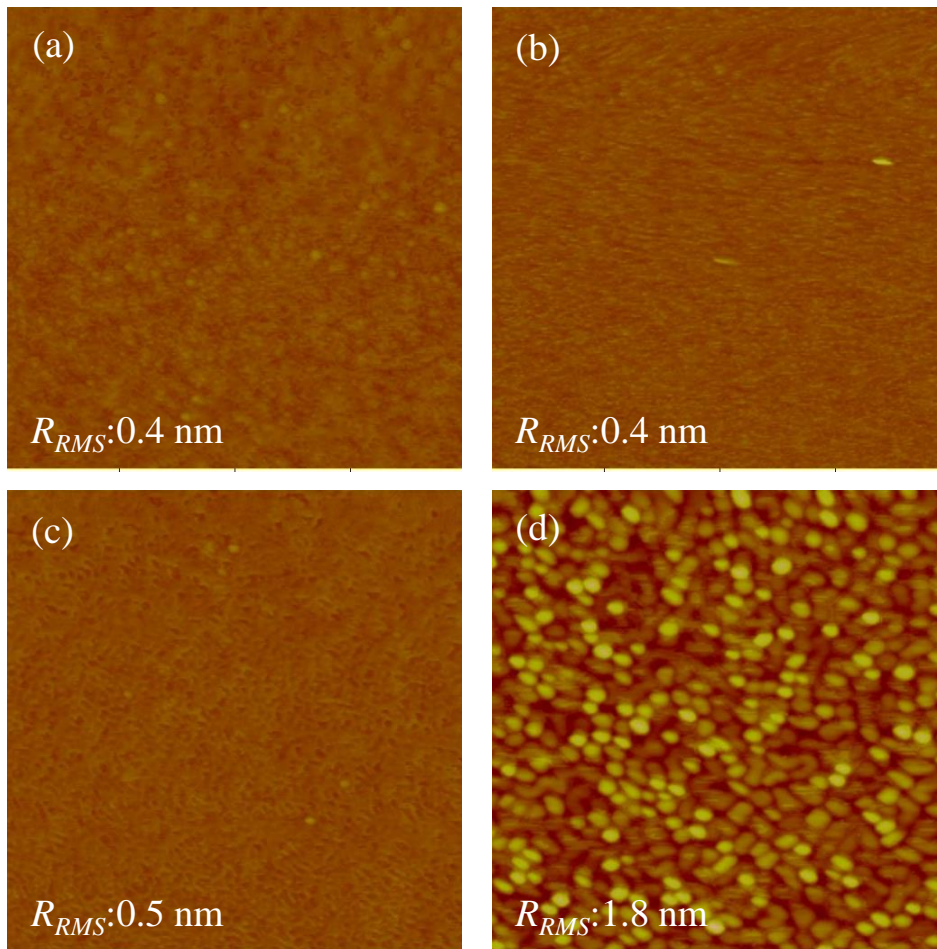
Figure 3.3 1×1 μm^2 AFM images of the FePt films grown on MgO substrate with deposition temperatures of (a) 150, (b) 250, (c) 350 and (d) 450 °C.

3.1.3 Magnetic Properties

With increasing deposition temperature, the PMA of the FePt films increased (Figure 3.4). This was attributed to the increased formation of (001) fct FePt phase at higher temperatures. The largest coercivity and squareness were obtained for the FePt film deposited at 450 °C. The magnetic anisotropy K_u was estimated based on Equation (3.2),

$$K_u = \frac{1}{2}H_k M_s, \tag{3.2}$$

where the anisotropy field H_k was obtained by extrapolating the magnetization curve [2]. As summarized in Table 3.1, K_u increased with increasing deposition temperature. It was further observed that a small 'step' or 'kink' was evident in the hysteresis loop of the FePt film deposited at 450 °C. This suggested the incomplete transformation of the FePt fcc disordered phase to the fct ordered phase.
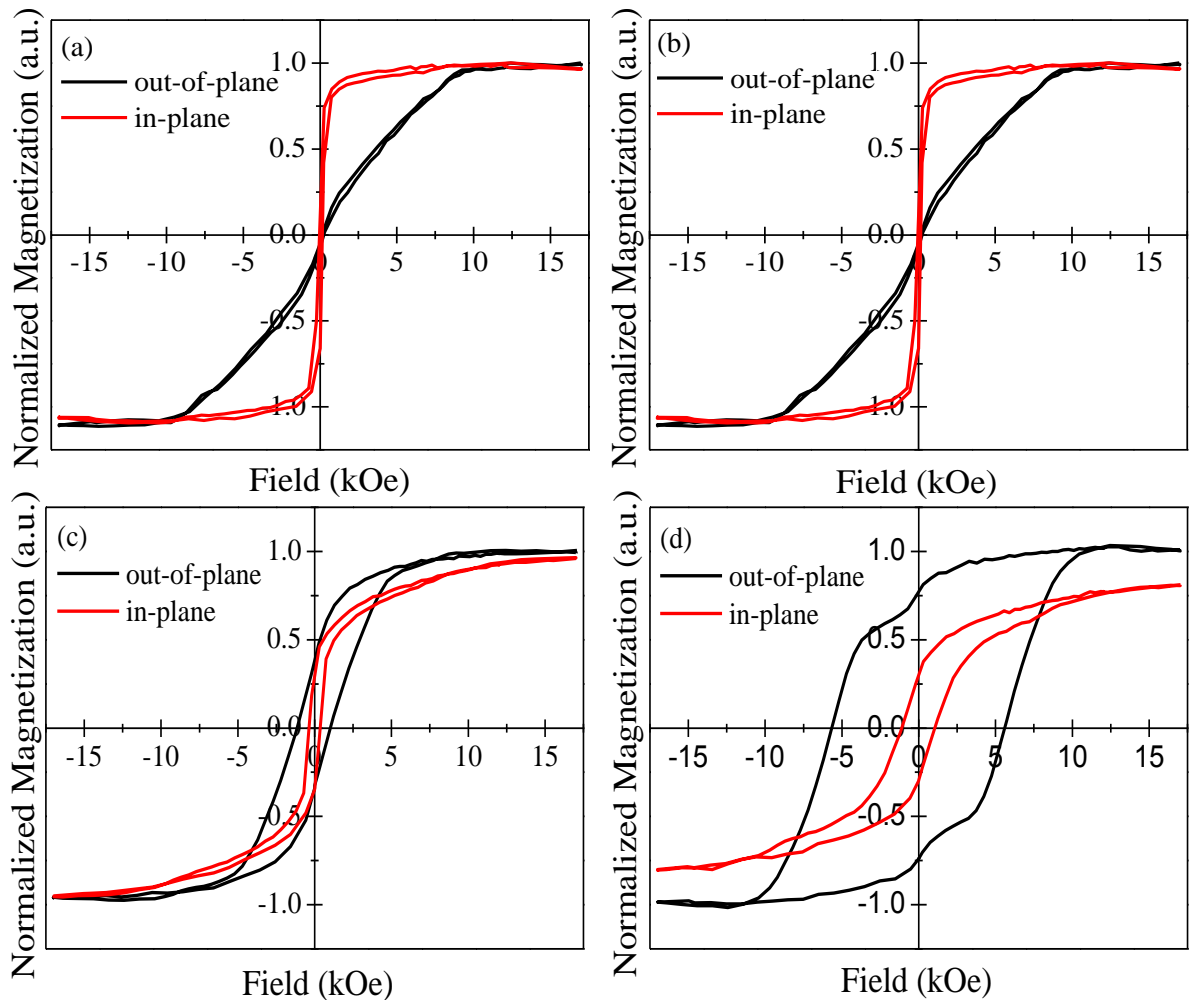
Figure 3.4   Out-of-plane and in-plane hysteresis loops of the FePt films with deposition temperatures of (a) 150, (b) 250, (c) 350 and (d) 450 °C.

Table 3.1   Summary of the magnetic properties of the FePt films deposited at different temperatures. Q is the quality factor where $Q = K_u/2\pi M_s^2$. d is the average domain size. δ is the estimated domain wall width where $\delta = \pi\sqrt{A/K_u}$, with $A = 10^{-6}$ erg/cm.

FePt Deposition Temperature (°C)	M_S (emu/cm^3)	K_u (10^7 erg/cm^3)	Q	d (nm)	δ (nm)
150	766	0.36	0.98	/	/
250	751	0.35	0.99	/	/
350	729	0.77	2.31	161	11
450	678	1.19	4.12	178	9

3.1.4 Domain Configurations

Domains form in FM materials to minimize the magnetic anisotropy and magnetostatic energies. The domain configurations are determined by the quality factor Q, defined as the ratio between the out-of-plane anisotropy energy to the demagnetizing energy [3-5]

$$Q = \frac{K_u}{2\pi M_s^2} \tag{3.3}$$

where K_u and $2\pi M_s^2$ are the magnetic anisotropy and magnetostatic energies, respectively. The FePt films deposited at 150 and 250 °C possessed small Q (Table 3.1). Films with Q << 1 would have flux closure domains with magnetization perpendicular to the out-of-plane direction so as to reduce the magnetostatic energy [Figure 3.5(a)] [5]. On the other hand, the FePt films deposited at 350 and 450 °C possessed large Q, where $Q >> 1$ (Table 3.1). These films were expected to favour the formation of stripe domains with magnetization parallel to the out-of-plane direction in order to reduce the magnetocrysalline energy [Figure 3.5(b)] [5].
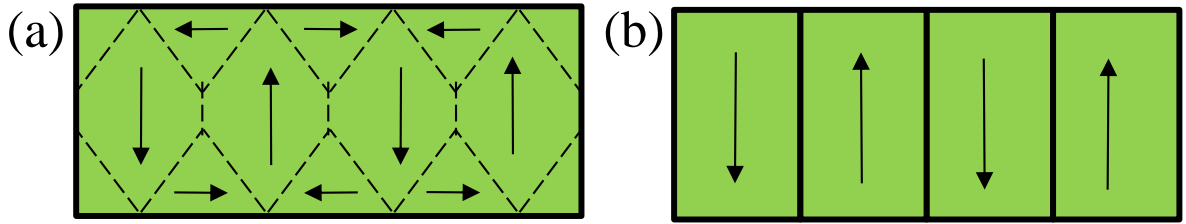
Figure 3.5   Schematic illustrations of domain configurations in (a) low anisotropy (Q << and (b) high anisotropy (Q >> 1) magnetic films.

The MFM images of the ac demagnetized FePt films in Figures 3.6(a) and (d) were in close agreement with that predicted based on the Q values of the FePt films [Figures 3.5(a) and (b)]. In Figures 3.6(a) and (b), the MFM images show large patches of poorly contrasted domains, reflecting the flux closure domains with magnetization away from the out-of-plane direction.
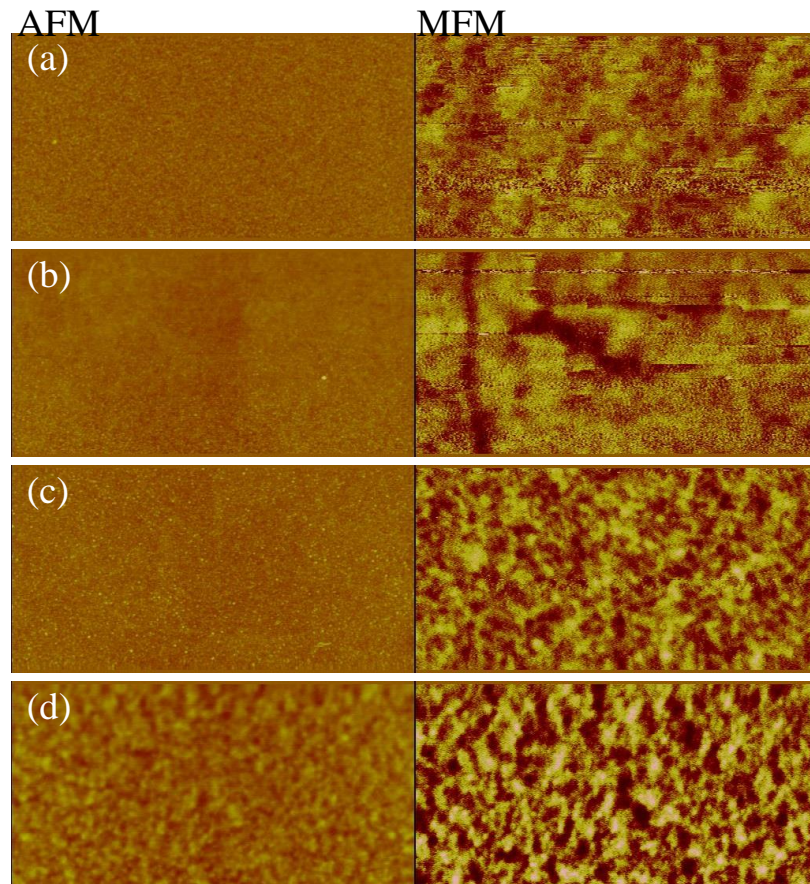
Figure 3.6 2.5×5 μm^2 AFM and MFM images of the FePt films with deposition temperatures of (a) 150, (b) 250, (c) 350 and (d) 450 °C. The films were ac demagnetized prior to the measurements taken in the absence of an applied field.

52

In Figures 3.6(c) and (d), the lighter yellow regions and dark brown contrast in the MFM images indicate the presence of stripe domains with magnetizations which were parallel and antiparallel to the film normal. The domain size d was measured for the FePt films deposited at 350 and 450 °C [Figures 3.6(c) and (d)] which displayed obvious oppositely magnetized stripe domains. This was obtained based on the average of the widths of 50 domains measured from the MFM images. The d value of the PMA $L1_0$-FePt film deposited at 450 °C was larger than that deposited at 350 °C (Table 3.1). The larger domains formed were presumably in direct correlation with its larger K_u [2, 5].

The domain wall is an interface, with distinctive electronics properties, between two domains with different magnetization directions. The domain wall width δ, which follows the relationship

$$\delta = \sqrt{A/K_u} \,, \tag{3.4}$$

was estimated to decrease with higher deposition temperatures (Table 3.1). Thus, the FePt layer with higher K_u possessed smaller δ. As a result of the small δ, the $L1_0$-FePt film with high K_u displayed MR due to domain wall contributions, which will be illustrated in Figure 3.7 of Section 3.1.5.

3.1.5 Magnetoresistance

As seen in Figure 3.7, the resistance of the FePt film decreased with increasing deposition temperature, indicating the notable effect of the substrate temperature on the FePt grain size and crystallinity. The higher deposition temperature provided increased mobility for the atoms, driving grain boundary movement and consequently promoted FePt grain growth. Thus, a more efficient percolation path

with bigger grains and less grain boundary scattering centres was available for the conduction electrons to transverse through, constituting a lower resistivity.
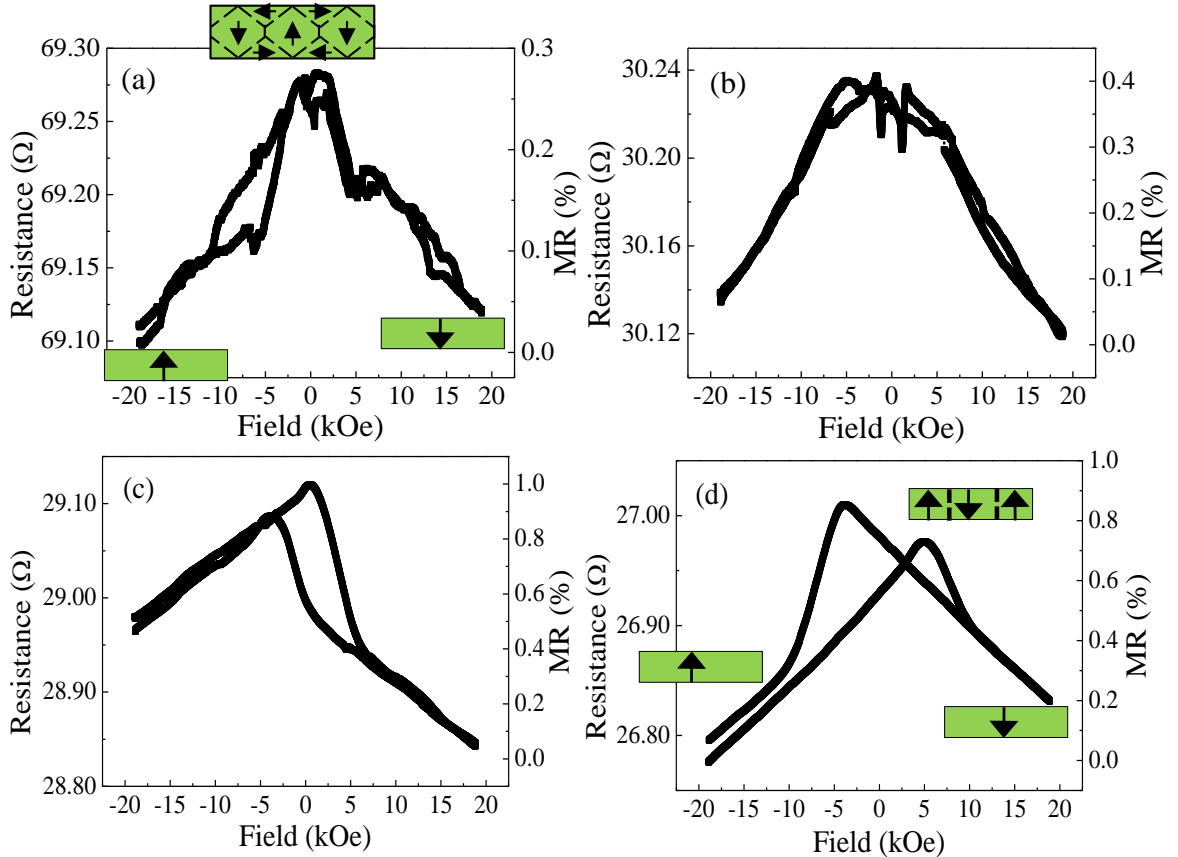
Figure 3.7   MR loops measured at room temperature for FePt films with deposition temperatures of (a) 150, (b) 250, (c) 350 and (d) 450 °C. The insets indicate schematically the reversal behaviours as described in the text.

For the FePt film deposited at 150 °C, possible contributions to the MR included the scattering due to the domain walls from the Néel closure caps [Figure 3.7(a) inset], granular film [Figure 3.2(a)] and spin disorder. However, the non-hysteretic MR curve suggested that contributions from the domain walls and grains were negligible. Levy and Zhang found that domain walls gave a smaller MR effect when aligned parallel to the current flow [5]. The presence of Néel closure caps reduced the proportion of domains walls which are perpendicular to the current

flow, resulting in a negligible domain wall MR contribution. In addition, the insignificant domain wall MR present at the low coercive fields would likely be masked by the background MR noise. At the same time, the negligible MR contribution from granular scattering could have been due to the width of the grain walls being much larger than the electron mean free path or spin diffusion length, thus preventing substantial spin dependent scattering. As such, the MR was largely attributed to the magnon spin disorder scattering [6]. At finite temperatures, the directions of the localized d electron spins fluctuated. At the same time, the itinerant s electrons, coupled to them by exchange interaction, scattered from the inhomogeneous exchange potential. This contributed to the magnon spin disorder scattering phenomenon. With increasing applied field, the MR decreased linearly. The applied magnetic field acted to reduce the spin disorder existing at equilibrium. As such, the overall resistivity decreased with increasing applied magnetic field.

For the FePt film deposited at 450 °C, a hysteresis was observed in the MR loop at the low field region in the range of -10 to 10 kOe [Figure 3.7(d)], which correlated well with the *M-H* hysteresis measurements [Figure 3.4(d)]. The MR observed was attributed largely to the domain scattering, in addition to the magnon spin disorder scattering. The direction of the electron spin changed as the electron transversed across the domain wall, which acted as a thin interface separating two domains with different magnetization directions [5]. Thus, the spin dependent electron scattering effect would be prominent when the electrons moved through the domain walls which possessed a length scale smaller than the electron mean free path. Hence, the $L1_0$-FePt film with high K_u, and a correspondingly narrow domain wall width, was expected to display intrinsic domain wall contribution to the overall resistivity. When the applied field was that of the coercivity of the $L1_0$-FePt

film [Figure 3.4(d)], the presence of a multi-domain state resulted in the highest MR. With increasing applied field larger than the coercivity, the saturation of the film into a single domain state led to a gradual reduction in the MR. As such, an enhancement in the MR of the FePt film by domain wall scattering was found with increasing deposition temperature, where the higher PMA FePt films promoted stripe domain formation with narrow domain wall widths.

An asymmetry in the resistance peak intensity of the MR loop was also observed in Figure 3.7(d). This was attributed to the extraordinary Hall effect (EHE), where spin orbit scattering in FePt caused a break in the spatial symmetry of the trajectory taken by the scattered electrons. The EHE is associated with the skew scattering and side jump mechanism, of which the dominance of the mechanism depends largely on the resistivity of the system [7-9]. At the large field region of 10 to 18 kOe, the MR decreased linearly due to the magnetic field suppression of spin disorder scattering. The MR curve was also not saturated at 18 kOe even though the corresponding *M-H* magnetization loop was well saturated at this field. This was likely caused by the superparamagnetic grain contribution of the granular $L1_0$-FePt film [Figure 3.2(d)] [10-11].

3.2 Behaviour of $L1_0$-FePt Thin Film

3.2.1 Temperature Dependence

A further investigation into the temperature dependent behavior of the $L1_0$-FePt thin film deposited at 450 °C was carried out. Figure 3.8 shows the temperature dependent hysteresis loops in the measurement temperature range of 50 to 300 K. The saturation magnetization M_s, magnetic anisotropy K_u and domain wall width δ

of the *L*1$_0$-FePt films are summarized as a function of temperature in Figures 3.9 to

3.11.
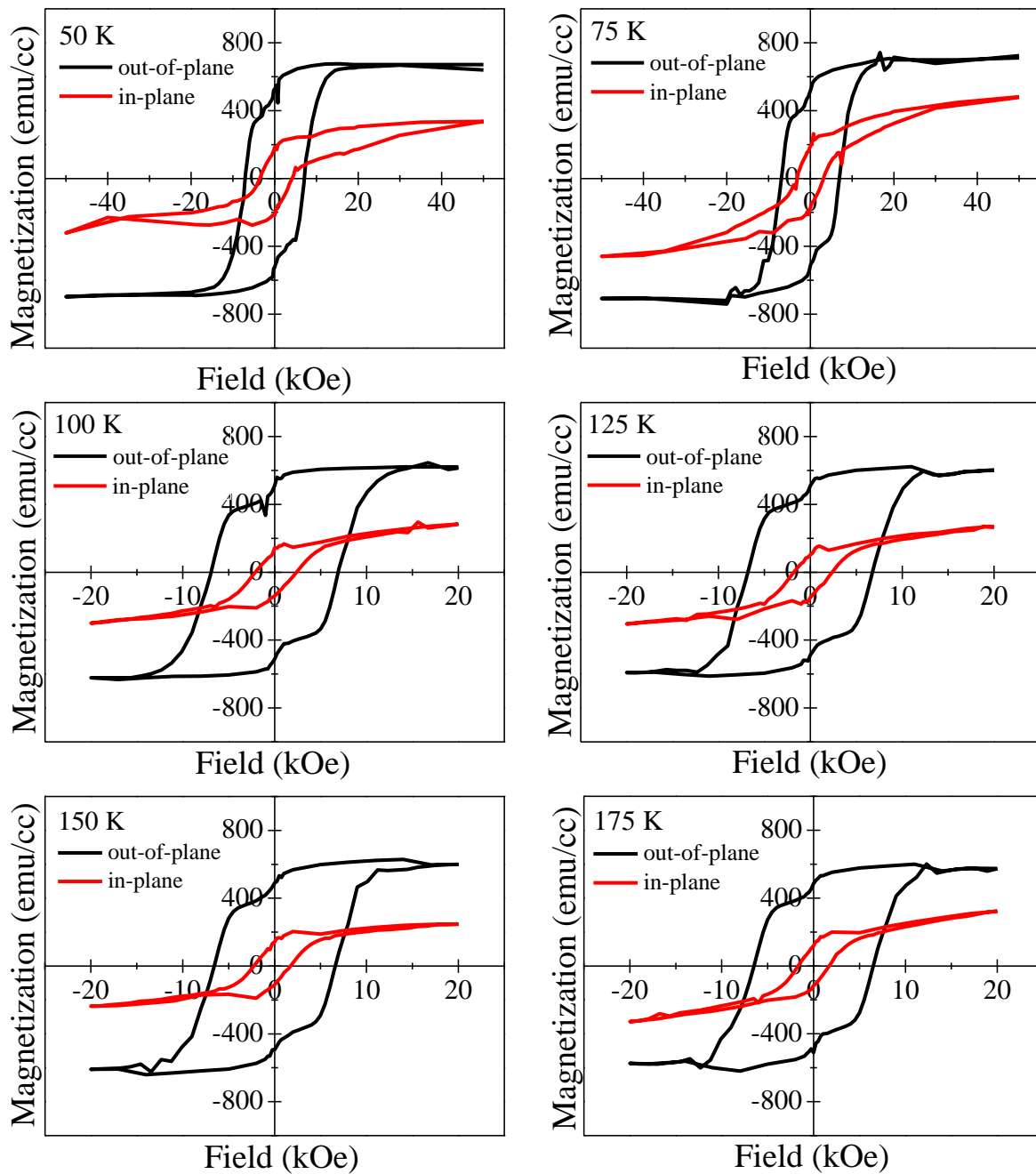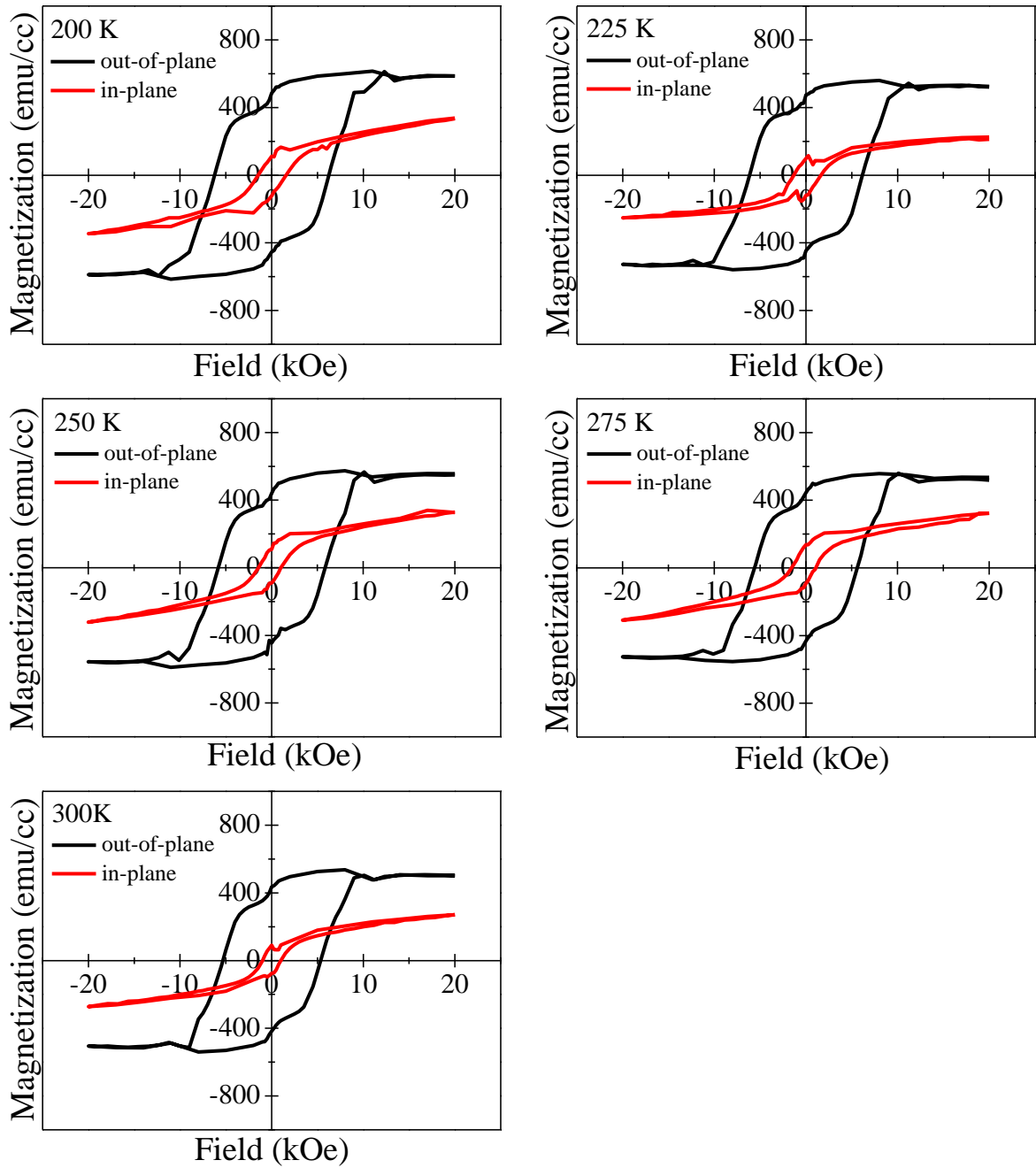
Figure 3.8   Out-of-plane and in-plane hysteresis loops of the $L1_0$-FePt film measured at different temperatures.
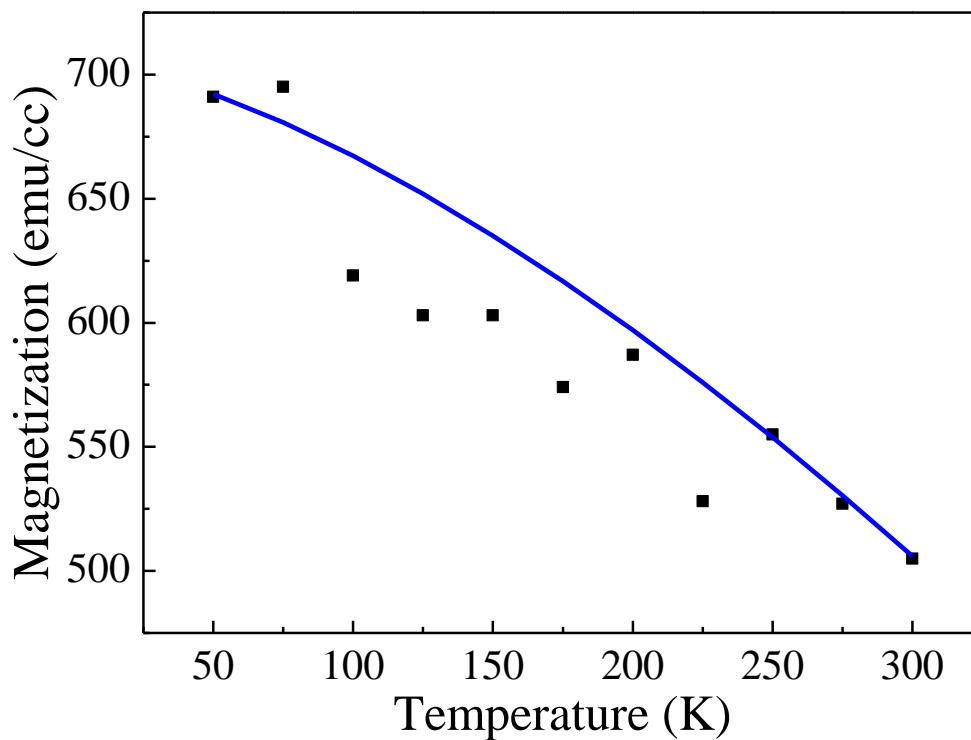
Figure 3.9   Saturation magnetization of the $L1_0$-FePt film as a function of temperature. The blue line indicates the Bloch law fit of the temperature dependence of M_s.
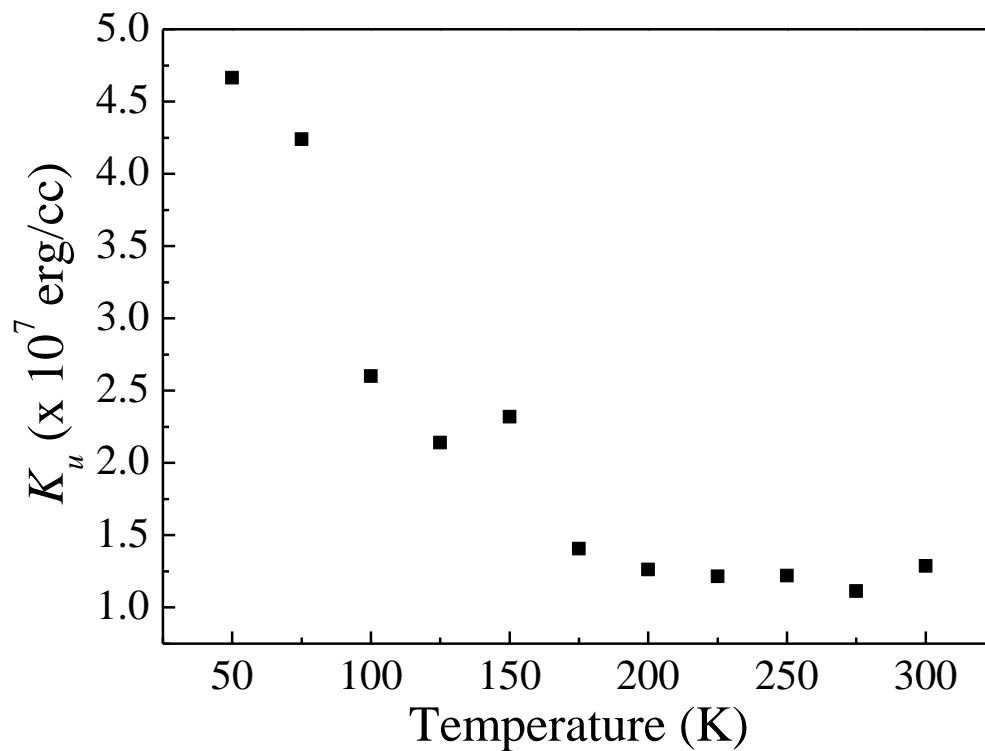
Figure 3.10 Magnetocrystalline anisotropy of the $L1_0$-FePt film as a function of temperature.
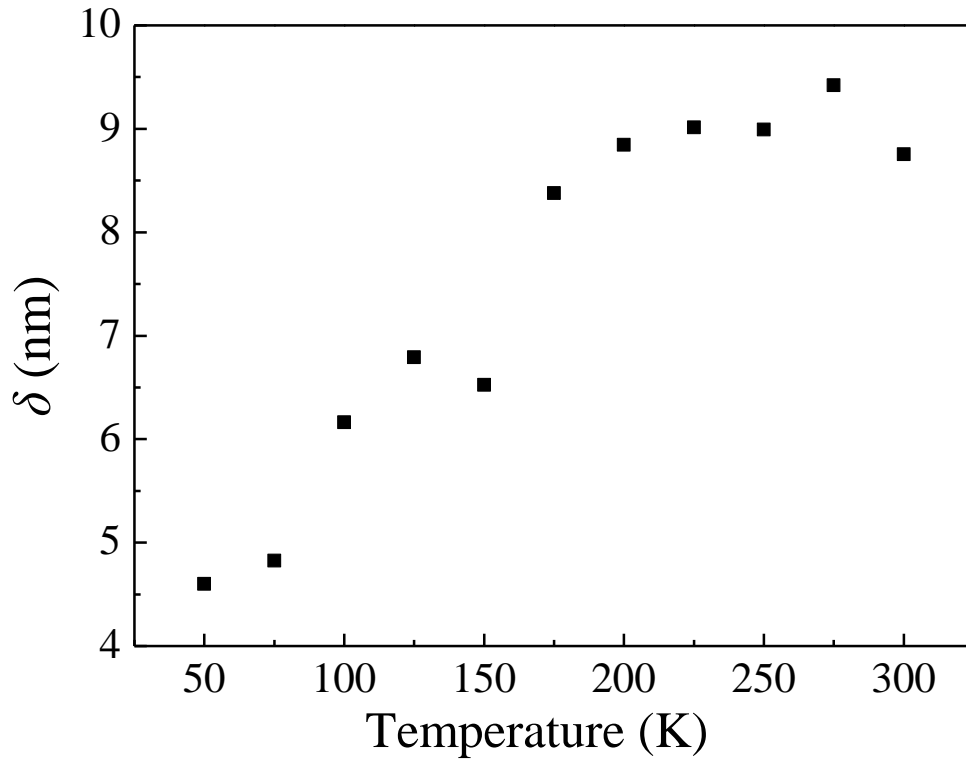
Figure 3.11 Domain wall width of the *L*1$_0$-FePt film as a function of temperature.

The M_s followed a $T^{3/2}$ relationship with temperature, evident from the Bloch law fit of the temperature dependence of M_s in Figure 3.9. The K_u was observed to decrease exponentially with temperature (Figure 3.10). The domain wall width δ increased with increasing temperature due to the increase in K_u (Figure 3.11).

The MR behaviour of the *L*1$_0$-FePt film at various measurement temperatures was studied using the PPMS with an applied field from -50 to 50 kOe (Figure 3.12).
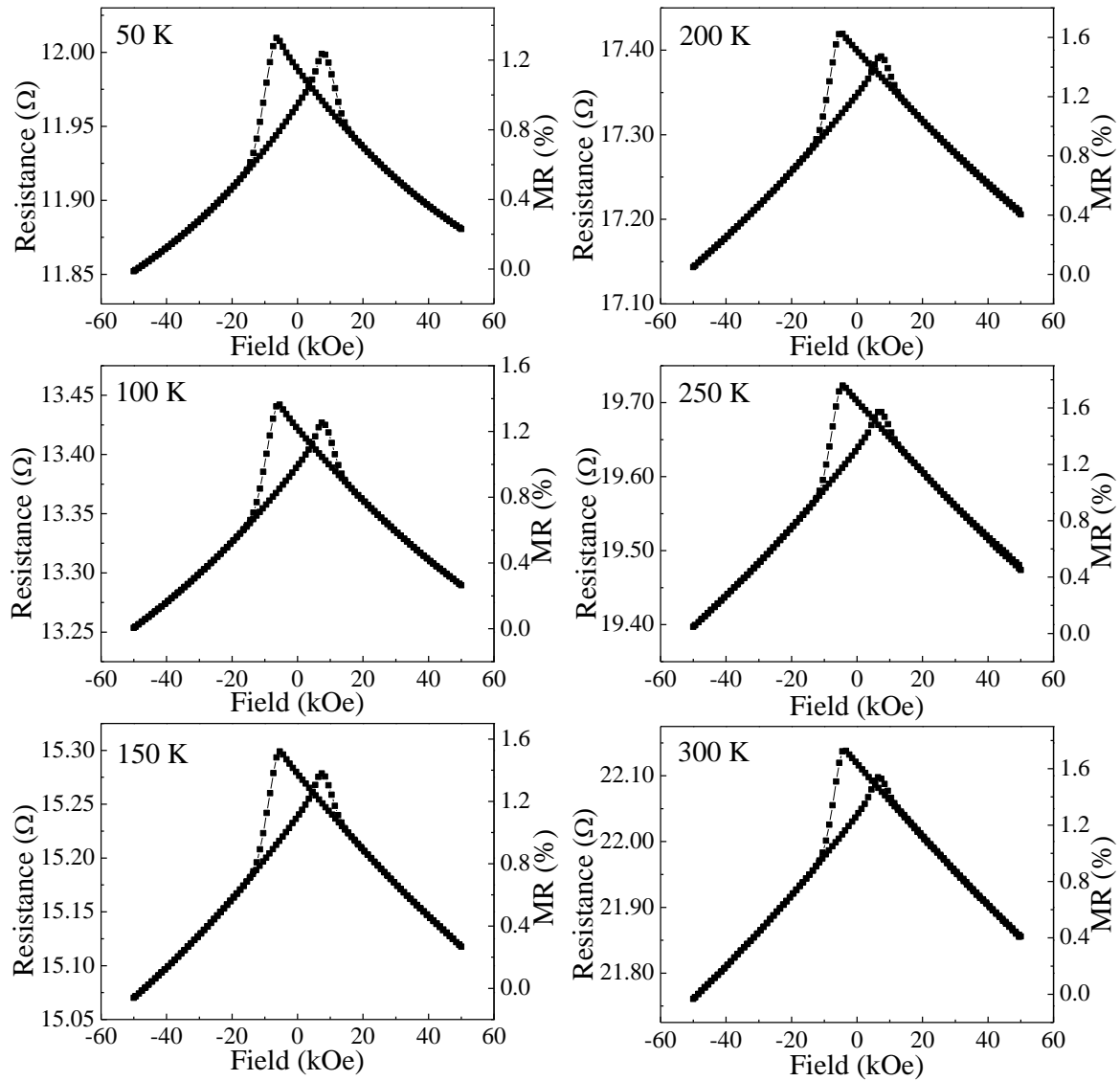
Figure 3.12 MR loops of the $L1_0$-FePt film measured at different temperatures.

The resistance of the $L1_0$-FePt film increased with an increase in the measurement temperature, displaying a generic metallic behaviour (Figure 3.12). In addition, a greater extent of spin independent scattering will occur, hence lowering the domain wall MR contribution. However, at each finite temperature, spin disorder scattering of the s and d electrons also contributed to the total resistivity. Increasing the temperature would escalate the spin disorder and contribute to a higher background magnon scattering. As a result, the overall MR increased with increasing temperature (Figure 3.13).

61
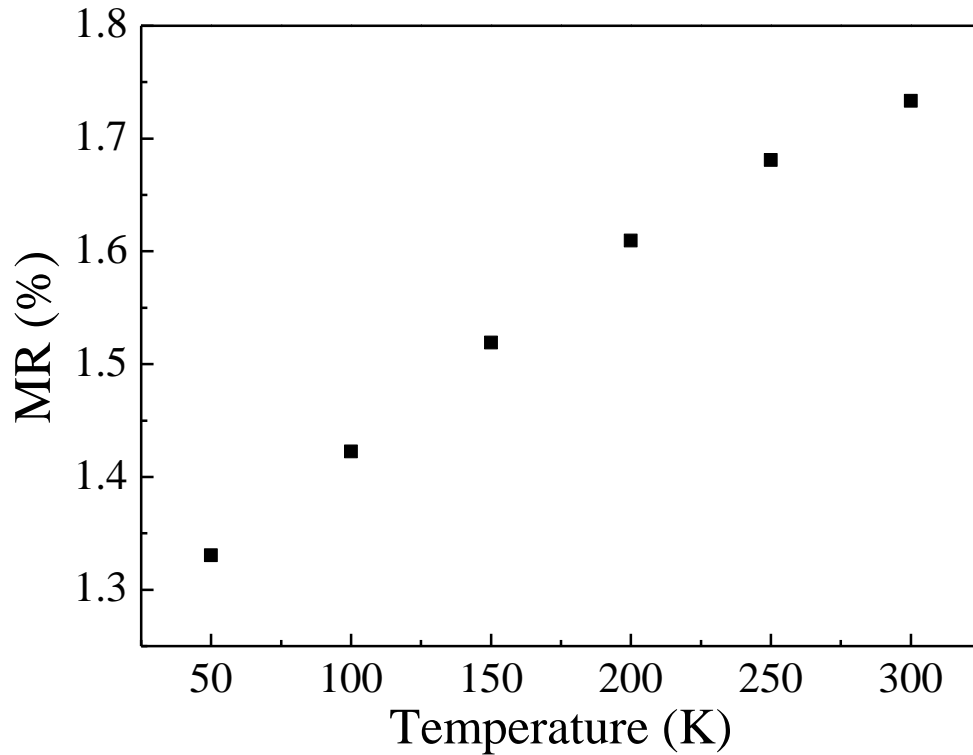
Figure 3.13 MR of the *L*1$_0$-FePt film as a function of temperature.

The slope of the R(H) curve in the high field region of 35 to 50 kOe was measured by linearizing the MR loops in the interval. A plot of the gradient of the R(H) curve in the high field region of 35 to 50 kOe against temperature is shown in Figure 3.14. The slope increased with increasing temperature, which reaffirmed the effects of the magnon-assisted spin flip scattering with temperature. When the temperature tended to zero, the slope was expected to go to zero in the case of a ferromagnet as the magnetic moments become fully aligned [8, 9]. However, an extrapolation of the slope versus temperature plot indicated otherwise for the *L*1$_0$-FePt film. This non-zero slope at 0 K indicated that the applied field, in the region of 35 to 50 kOe, was not sufficiently strong to impose full magnetic order on the spins.
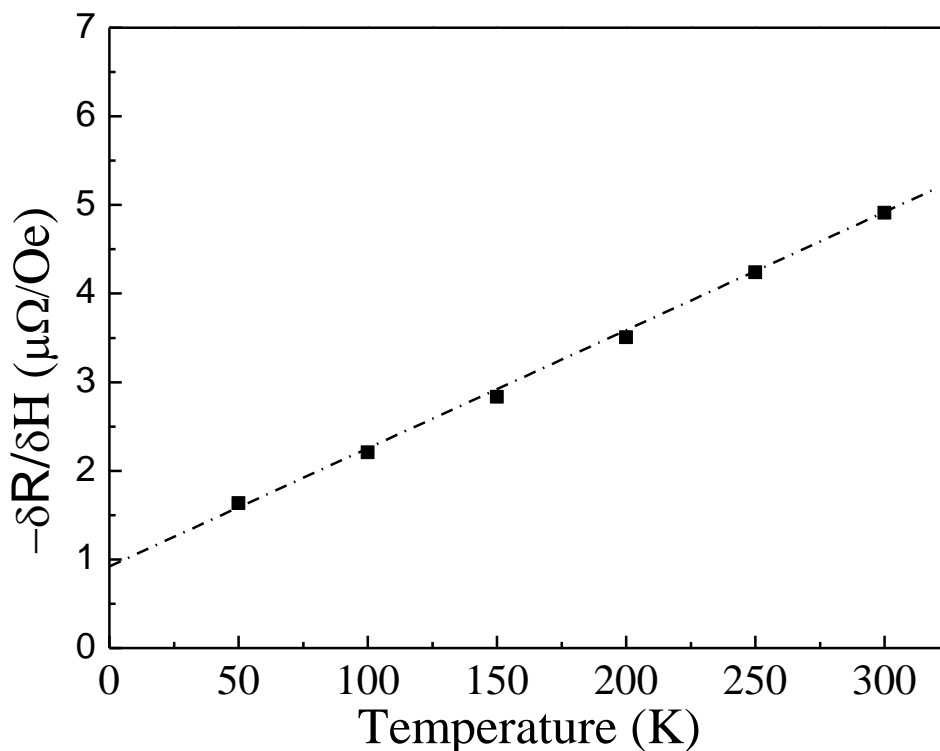
Figure 3.14 Temperature dependent resistance-field slope for the *L*1$_0$-FePt film deposited at 450 °C. The slope of the R(H) curve was measured by linearizing the measured MR loops in the interval 35 to 50 kOe.

3.2.2 Angular Dependence

This section focuses on the angular dependence of the magneto-transport behavior of the *L*1$_0$-FePt film deposited at 450 °C (Figure 3.15). The study of the angular dependent MR probes the contributions by magnetic domains, where the domain structure changes with perpendicular, longitudinal or transverse fields. An applied field at 0 and 90 ° represents the in-plane and out-of-plane magnetizations, respectively. An in-plane current was applied via the four point probe while a magnetic field of -18 to 18 kOe was supplied via the VSM. The resistance and MR as a function of applied field angle are also summarized in Figures 3.16 and 3.17, respectively.
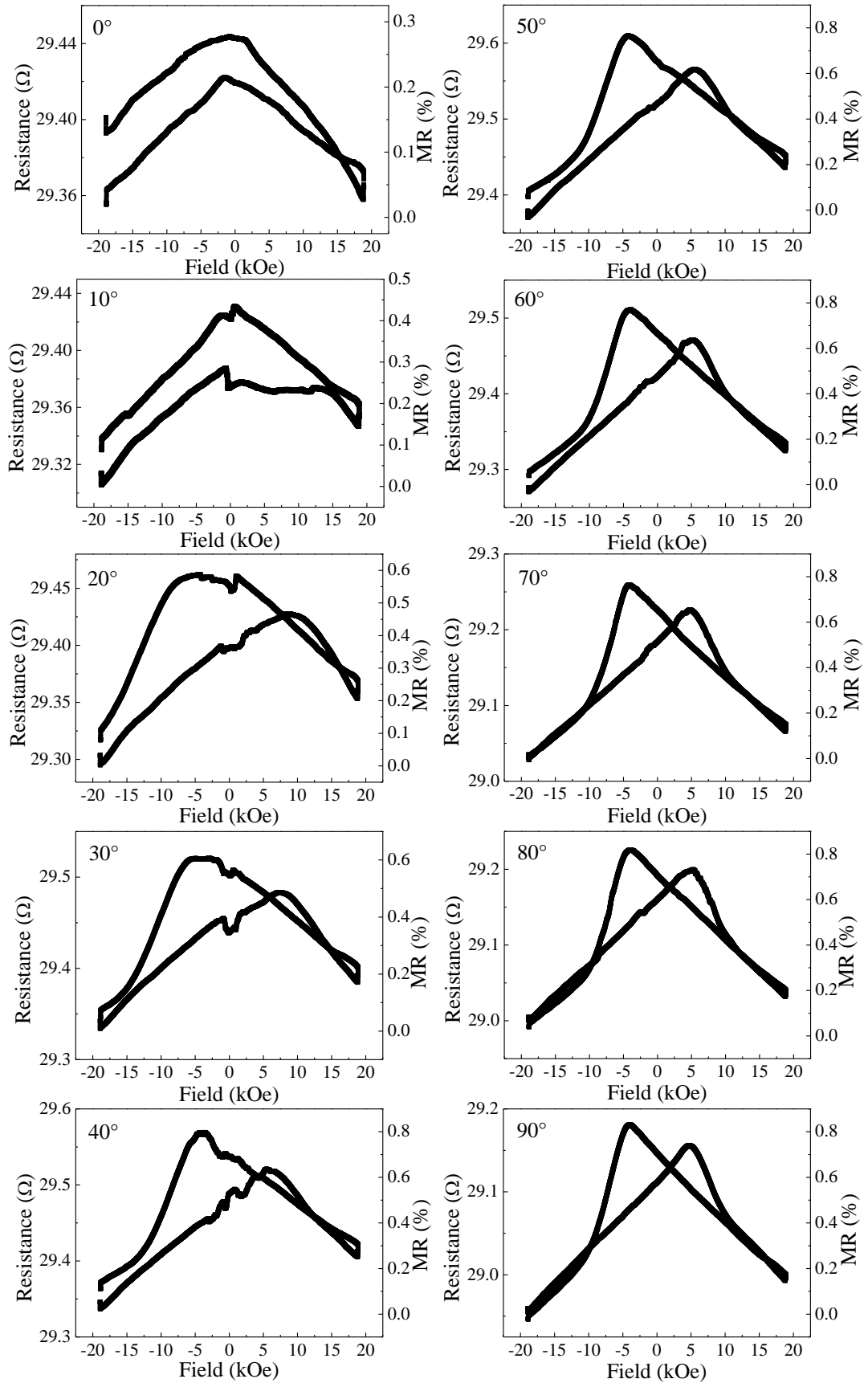
Figure 3.15 Room temperature MR loops of the $L1_0$-FePt film at different angles. An angle of 0 and 90 ° indicates an applied field in the film in-plane and out of plane, respectively.

Figure 3.16 shows that the resistance, taken at the maximum applied field of -18 kOe, decreased with a transition from an in-plane to out-of-plane applied field. When an in-plane field was applied, the $L1_0$-FePt film contained domains as it was not fully saturated in its hard axis at -18 kOe [refer to in-plane hysteresis loop in Figure 3.4(d)]. Conduction electrons scattered by the domain walls led to a higher resistance. On the contrary, an out-of-plane field of -18 kOe acting on the $L1_0$-FePt film resulted in a magnetization state close to full saturation. Scattering by domain walls was eliminated and the resistance diminished.
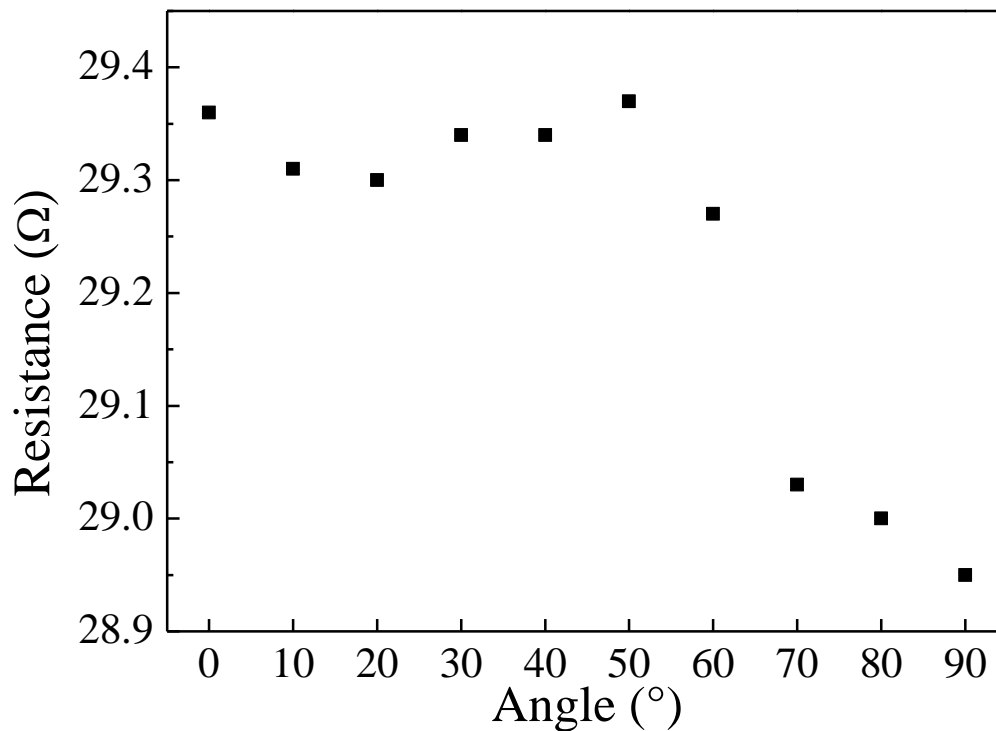
Figure 3.16 Resistance of the $L1_0$-FePt film with respect to the relative angle between the $L1_0$-FePt film and applied field of magnitude -18 kOe. An angle of 0 and 90 ° indicate an applied field in the film in-plane and out of plane, respectively.

The MR was smaller for the in-plane applied field geometry compared to that of the out-of-plane applied field geometry (Figure 3.17). The MR curve also changed from a non-hysteretic to a hysteretic form with the change in applied field angle from 0 to 90 ° (Figure 3.15). Resistivity anisotropy was evidently present in the

$L1_0$-FePt film. The trend is associated with the magnetic domain structure and orientation relative to the applied current direction. At an angle of 0 °, where applied field is parallel to the plane of the film, the domains possessed magnetization in the same direction as the in-plane current direction. Contributions by AMR and spin disorder scattering gave rise to the overall resistivity. When the applied field was 90 ° to the plane of the flim, domain walls and magnetization perpendicular to the in-plane current direction were set up prior to complete saturation. AMR was effectively suppressed since the magnetization and the current remained mutually perpendicular throughout the magnetic sweep field. Domain scattering contributed more substantially to the MR in the perpendicular geometry as the perpendicular domain MR effect was more significant than that of the longitudinal [5].
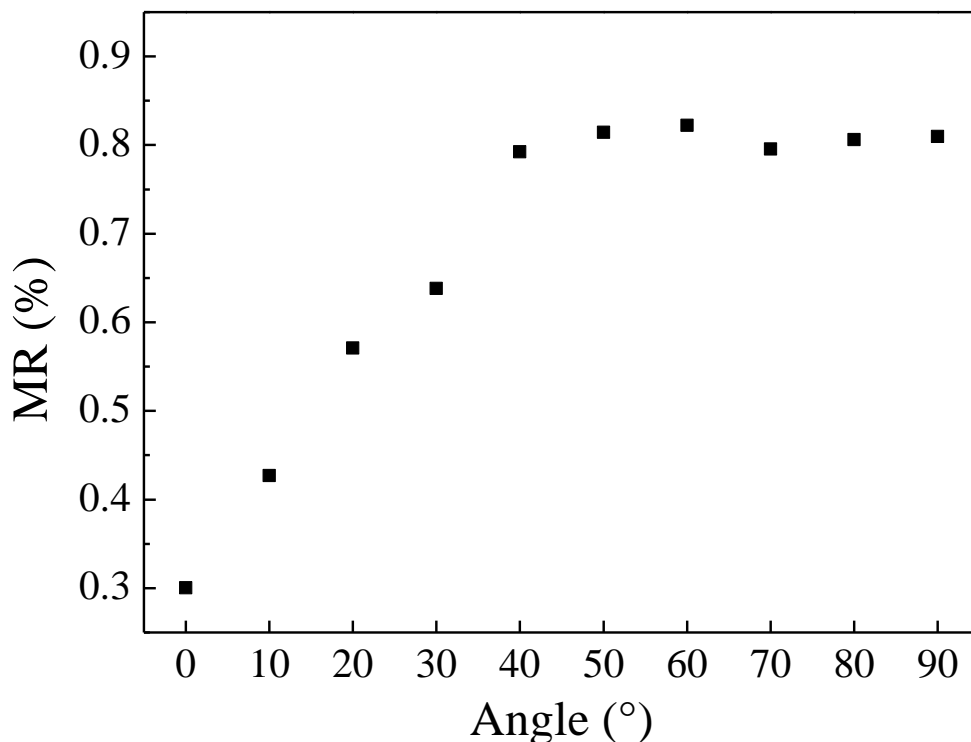
Figure 3.17 MR as a function of the angle made by the $L1_0$-FePt film, deposited at 450 °C, with the applied field. An angle of 0 and 90 ° indicates an applied field in the film in-plane and out of plane, respectively.

References

1. S. Okamoto, N. Kikuchi, O. Kitakami, T. Miyazaki, and Y. Shimada, Phys. Rev. B **66**, 024413 (2002).

2. B. D. Cullity and C. D. Graham, Introduction to Magnetic Materials Second Edition, Wiley, Canada, 2009.

3. L. M. Alvarez-Prado and J.M. Alameda, Physica B **343**, 241 (2004).

4. A. D. Kent, U. Rudiger, J. Yu, L. Thomas, and S. S. P. Parkin, J. Appl. Phys. **85**, 5243 (1999).

5. A. D. Kent, J. Yu, U. Rudiger, and S. S. P. Parkin, J. Phys.: Condens. Matter. **13**, R461 (2001).

6. P. Allia, F. Celegato, M. Coisson, P. Tiberto, F. Vinai, F. Albertini, F. Casoli, and S. Fabbrici, J. Magn. Magn. Mater. **322**, 1898 (2010).

7. O. Shaya, M. Karpovski, and A. Gerber, J. Appl. Phys. **102**, 043910 (2007).

8. K. M. Seemann, V. Baltz, M. MacKenzie, J. N. Chapman, B. J. Hickey, and C. H. Marrows, Phys. Rev. B **76**, 174435 (2007).

9. K. M. Seemann, Y. Mokrousov, A. Aziz, J. Miguel, F. Kronast, W. Kuch, M. G. Blamire, A. T. Hindmarch, B. J. Hickey, I. Souza, and C. H. Marrows, Phys. Rev. Lett. **104**, 076402 (2010).

10. S. Honda, K. Koguma, M. Nawate, and I. Sakamoto, J. Appl. Phys. **82**, 4428 (1997).

11. S. Ge, H. Li, C. Li, L. Xi, W. Li, and J. Chi, J. Phys.: Condens. Matter. **12**, 5905 (2000).

CHAPTER 4

4   PERPENDICULAR MAGNETIC ANISOTROPY

$L1_0$-FePt/Ag/$L1_0$-FePt PSVs

Based on earlier reports of sputter deposited $L1_0$-FePt based spin valves, only Au, Pt and Pd have been studied as the spacer materials (Table 1.1). The use of Au and Pt spacers yielded low GMR values of 0.08 and 0.65 % respectively, due to the high tendency of these heavy elements to depolarize the spins of the conduction electrons through high spin orbit scattering. In contrast, the use of a lighter noble element Pd achieved a higher GMR of 0.80 % [1, 2]. In view of that, this work focuses on the use of Ag as the spacer material in the $L1_0$-FePt based PSVs. Ag is a noble metal with atomic number (47) close to that of Pd (46). Furthermore, earlier studies showed that Ag (001) grown as an intermediate layer between FePt films induced well-oriented epitaxial $L1_0$-FePt (001) texture at a lower ordering temperature [3, 4]. As such, Ag is considered a suitable candidate for the spacer.

Samples with the structure MgO (001) substrate/$L1_0$-$Fe_{50}Pt_{50}$ (20 nm)/Ag (2.5 nm)/$L1_0$-$Fe_{50}Pt_{50}$ (5 nm), shown in Figure 4.1, were fabricated using a magnetron sputtering system with a base pressure better than 3×10^{-7} Torr. The bottom and top $Fe_{50}Pt_{50}$ layers were deposited at 450 °C and 300 °C, respectively. The Ag spacer layer was deposited at 150 °C and in situ post-annealing was carried out at 300, 400 or 500 °C. The effects of varying Ag post-annealing temperature were studied through experimental characterizations, atomistic and micromagnetics modelling.

$Fe_{50}Pt_{50}$	5 nm, 300 °C
Ag	2.5 nm, 150 °C, PA (300,400,500 °C)
$Fe_{50}Pt_{50}$	20 nm, 450 °C
MgO substrate	
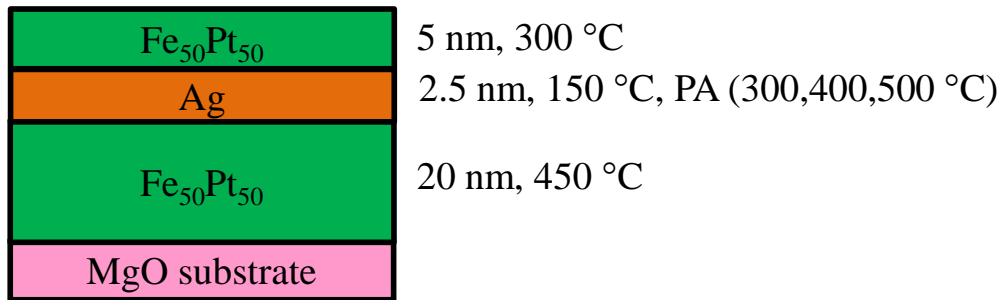
Figure 4.1   Schematic diagram of MgO/$L1_0$-FePt/Ag/$L1_0$-FePt PSV.

4.1 Experimental Characterization

4.1.1 Interfacial and Microstructural Properties

With increasing post-annealing temperature from 300 to 500 °C, the roughness of the Ag layer decreased by a factor of 2 (Figure 4.2). In addition, HRTEM images (Figure 4.3) show that with increasing Ag post-annealing temperature from 300 to 500 °C, the thickness of the spacer layer decreased from 2.2 to 1.4 nm although this was intended to be constant across all samples. At higher post-annealing temperatures, a greater extent of inter-diffusion between bottom $L1_0$-FePt and Ag occurred, causing a reduction in the Ag spacer layer thickness.
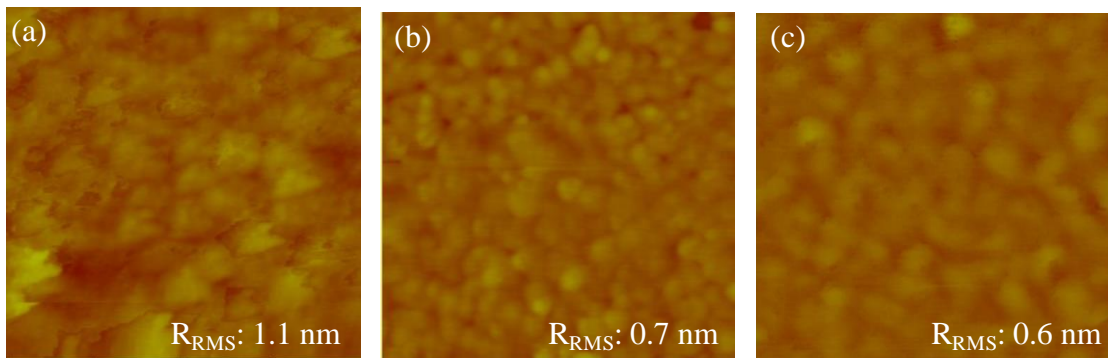
Figure 4.2 1×1 µm^2 AFM images of Ag surface grown on MgO substrate/$L1_0$-FePt with Ag post-annealed at (a) 300, (b) 400 and (c) 500 °C. Root mean square roughness was measured.
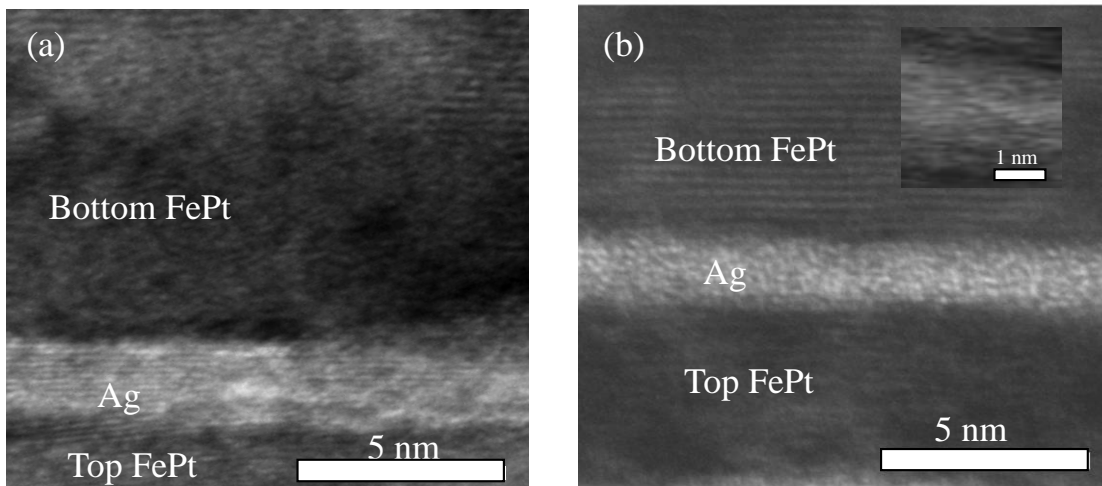
Figure 4.3   HRTEM images of MgO substrate/$L1_0$-FePt/Ag/$L1_0$-FePt PSVs with Ag post-annealed at (a) 300 °C and (b) 500 °C. The inset in (b) shows the higher magnification TEM image of the PSV with Ag post-annealed at 500 °C.

4.1.2 Crystallographic Properties

Figure 4.4 shows the XRD spectrums of the PSVs with Ag post-annealed at 300, 400 and 500 °C. Strong superlattice (001) and (003) peaks and fundamental (002) peak of FePt were observed for all the PSVs. At the same time, (111) peaks were absent in the θ-2θ scan. These were indicative of the presence of well textured out-of-plane $L1_0$-FePt phase in all of the PSVs despite the different Ag post-annealing temperatures of 300, 400 and 500 °C. No Ag x-ray peaks were observed in the θ-2θ scan for all the PSVs. This was not an indication of poor Ag (002) texture; rather a result of the thin Ag film which was unable to produce significant x-ray reflection relative to the background noise. This was supported by the observation of lattice fringes in the HRTEM images of the Ag spacer [Figure 4.3(a) and inset of 4.3(b)], indicating the growth of (001) textured crystalline Ag film in the PSV with Ag post-annealed at 300 and 500 °C. The Ag spacer produced a brighter contrast as the neighbouring $L1_0$-FePt layers, enriched with heavy Pt atoms, caused more inelastic scattering that weakened the direct electron beam contributing to the image.
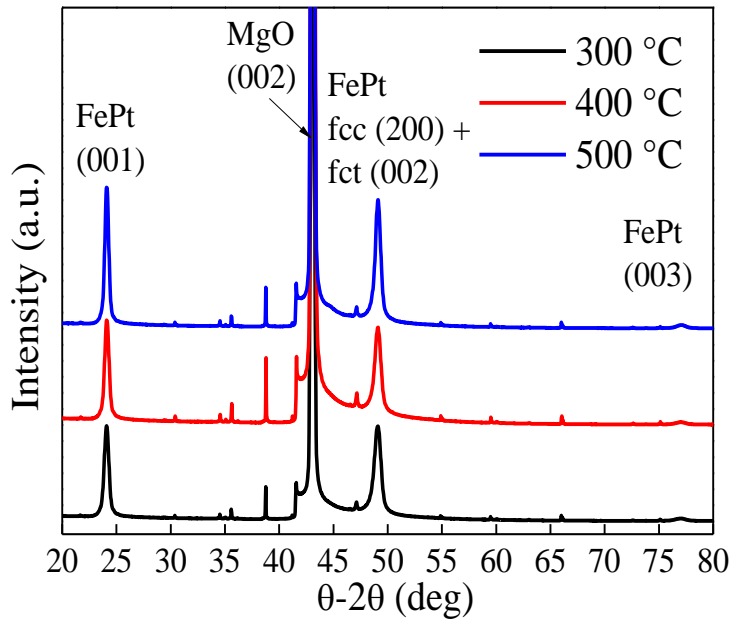
Figure 4.4   XRD spectrums of the PSVs with the Ag spacer post-annealed at (a) 300, (b) 400 and (c) 500 °C. The remaining unlabelled sharp peaks are inherent of the MgO substrate.

Azimuthal scans were carried out for the off-specular fcc MgO substrate (224) and fct $L1_0$-FePt (112) reflections of the PSVs. The (224) and (112) reflections are 35.26 and 34.27 ° away from the normal of the specular rod, respectively (Figure 4.5). By adjusting the angle χ, the Bragg's condition for MgO (224) and $L1_0$-FePt (112) can be satisfied.
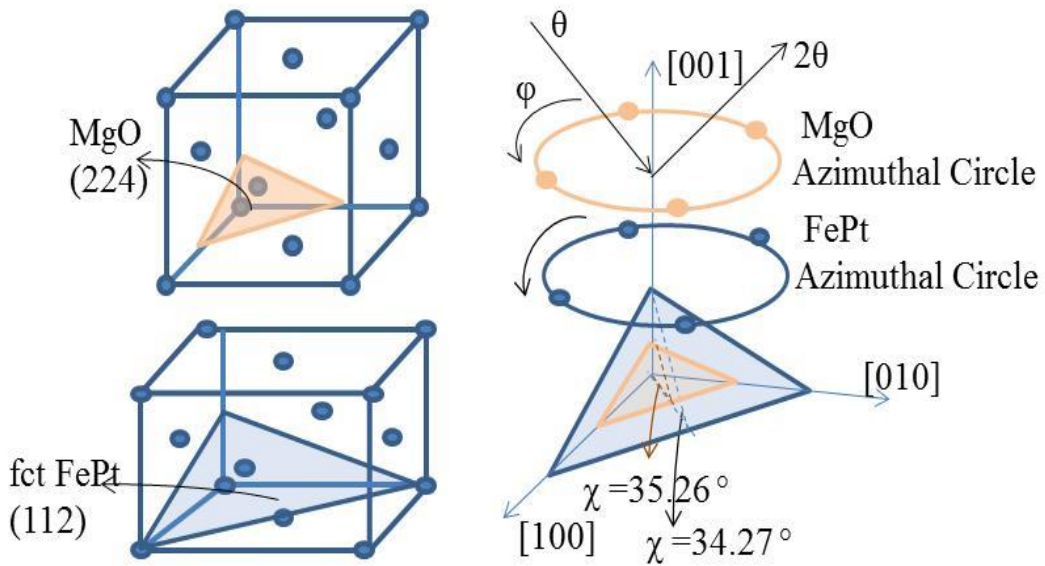
Figure 4.5   Schematic illustrations of the FePt (112) and MgO (224) planes in which azimuthal scans were carried out on.

Well-defined four fold symmetry of the *L*1$_0$-FePt (112) reflections followed that of the MgO (224) reflections in the PSVs with Ag post-annealed at 300, 400 and 500 °C [Figures 4.6(a)-(c)]. This cube on cube orientation indicated that the fct *L*1$_0$-FePt in all the PSVs had been epitaxially grown onto the MgO (001) substrate, thus establishing the relationship FePt[100](001)/MgO[100](001). The Ag (224) off-specular reflections, 35.26 ° away from the specular normal, cannot be measured by the azimuthal scan as the thin Ag layer could not produce a detectable Ag peak (Figure 4.4).
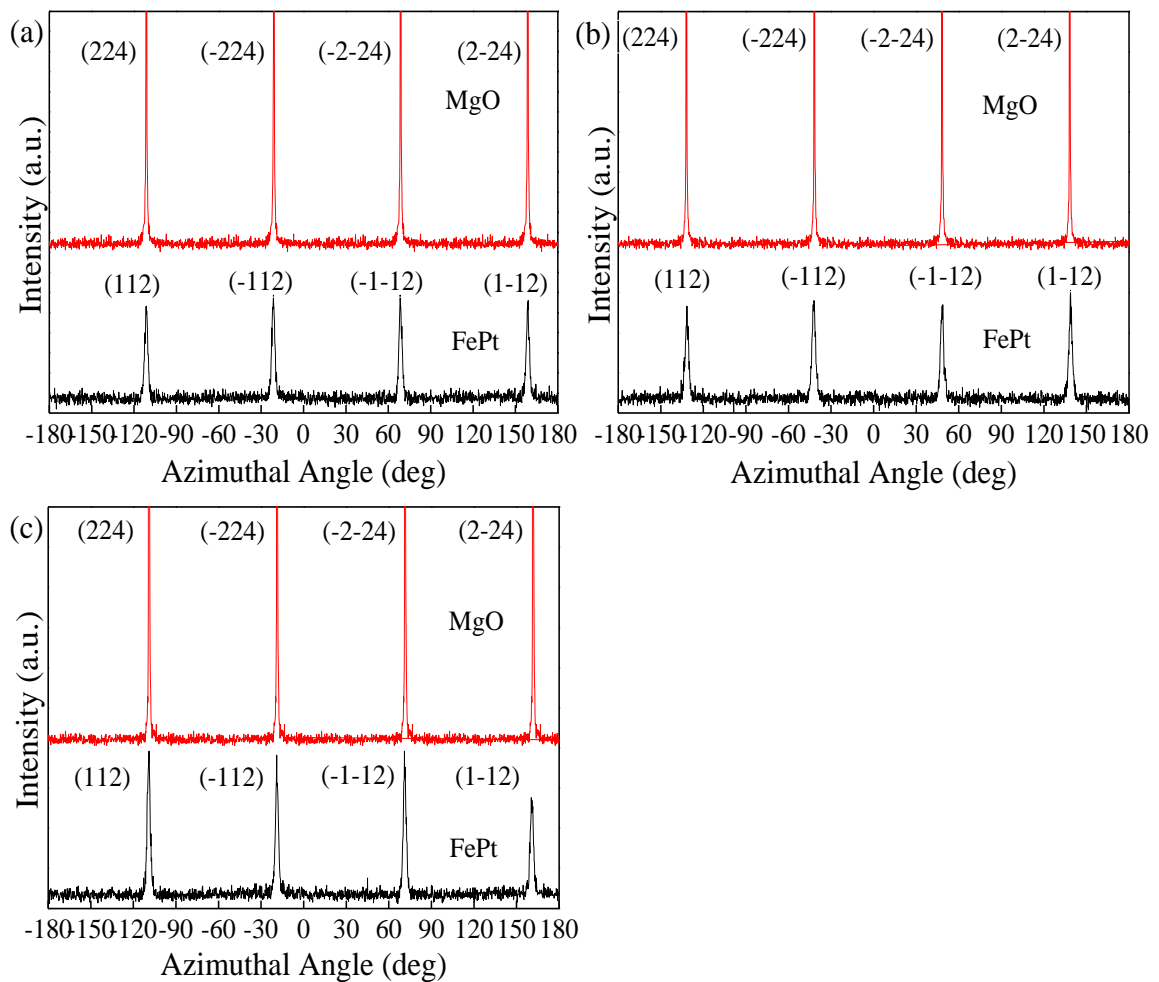
Figure 4.6   Azimuthal scans of the PSVs when the Ag spacer was post-annealed at (a) 300, (b) 400 and (c) 500 °C.

Figure 4.7 shows the RSMs of the PSVs in which the MgO substrate with (002) orientation was assigned the reference layer. The RSMs revealed intensity contour plots with a strong pronounced (002) MgO reflection and subsequently a FePt reflection halo. No Ag reflection was observed as the thin Ag film was unable to produce significant x-ray reflection relative to the background noise. The FePt and MgO reflection contour plots in the same [100] direction suggested that the FePt films were strained with the lattice misfit between MgO (001) and FePt (001) being 8.8 %. The FePt intensity contour plot was a representation of both FePt fcc (200) and FePt fct (002) as the negligible difference in their lattice parameters made them difficult to differentiate. With increasing Ag post-annealing temperature, there was no significant change to the size of the FePt reflection halo, suggesting that the formation of the *L*1$_0$-(001) texture in the FePt layers was not significantly affected by the Ag spacer post-annealing temperature.
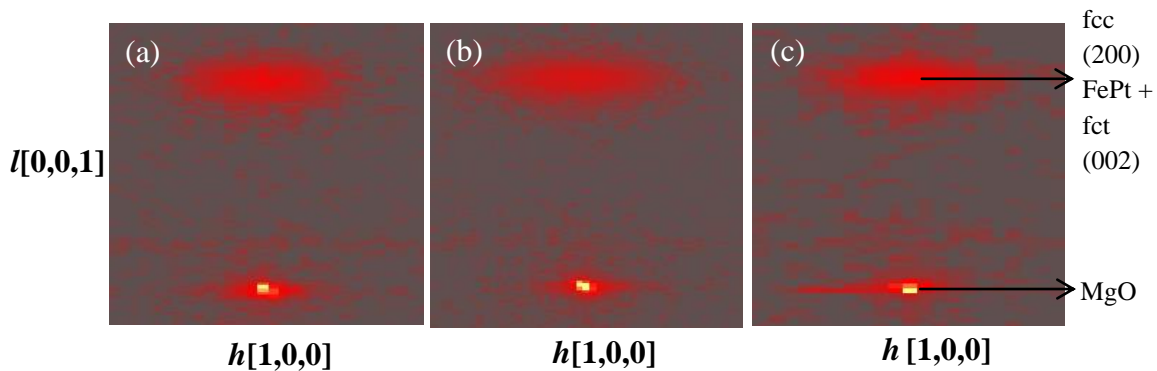
Figure 4.7   RSMs of the specular (002) reflections of MgO, Ag and FePt when the Ag spacer was post-annealed at (a) 300, (b) 400 and (c) 500 °C. MgO (002) substrate was assigned to be the reference layer.

4.1.3 Magnetic Properties

For Ag post-annealing temperatures of 300 and 400 °C, both PSVs were exchange decoupled and exhibited no significant difference in their magnetic properties (Figure 4.8). The thicker bottom *L*1$_0$-FePt possessed a higher coercivity than the

thinner top $L1_0$-FePt. Thus, the harder bottom $L1_0$-FePt behaved as the fixed layer while softer top $L1_0$-FePt the free layer. Further increase of the Ag post-annealing temperature to 500 °C resulted in the disappearance of the kink in the hysteresis loop. The extensive inter-diffusion between bottom $L1_0$-FePt and Ag resulted in a thinner Ag spacer which was insufficient to bring about exchange decoupling between the top and bottom $L1_0$-FePt.
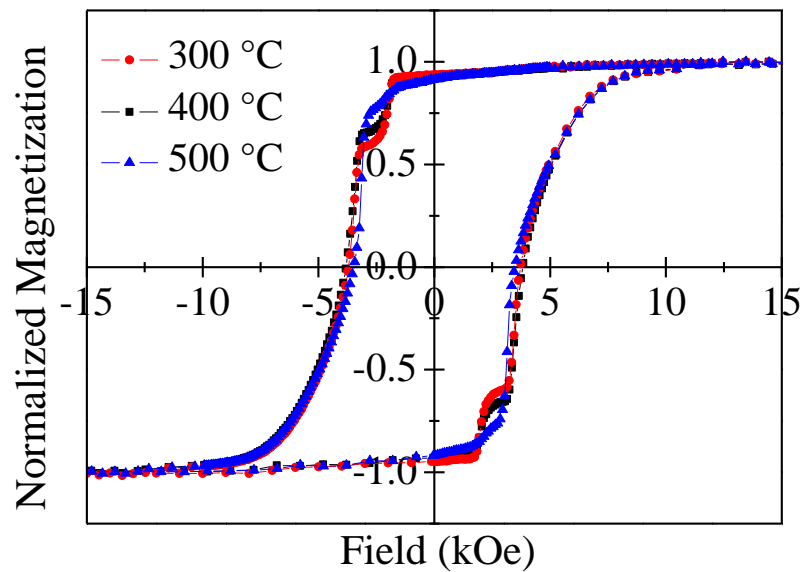
Figure 4.8 Hysteresis loops of the $L1_0$-FePt/Ag/$L1_0$-FePt PSVs with varying Ag post-annealing temperatures of 300, 400 and 500 °C.

The switching field distribution (SFD) curves [Figures 4.9(a) and 4.9(b)] of the PSVs with Ag post-annealed at 300 and 400 °C show two distinct peaks, demonstrating independent magnetization reversal of the top and bottom $L1_0$-FePt layers. The SFD of the bottom $L1_0$-FePt layer increased when Ag post-annealing temperature increased from 300 to 400 °C, indicative of reduced exchange coupling between the bottom FePt particles at higher Ag post-annealing temperatures. This was attributed to the formation of more decoupled grains within the bottom $L1_0$-FePt layer with higher Ag post-annealing temperature, a result of increased Ag diffusion to the high energy $L1_0$-FePt grain boundaries [5, 6]. When

the Ag post-annealing temperature increased to 500 °C, the formation of a more granular FePt phase was expected. However, the derivative of the hysteresis loop reflected a narrower SFD for the bottom $L1_0$-FePt layer due to exchange coupling with the top $L1_0$-FePt layer [Figure 4.9(c)] [7].
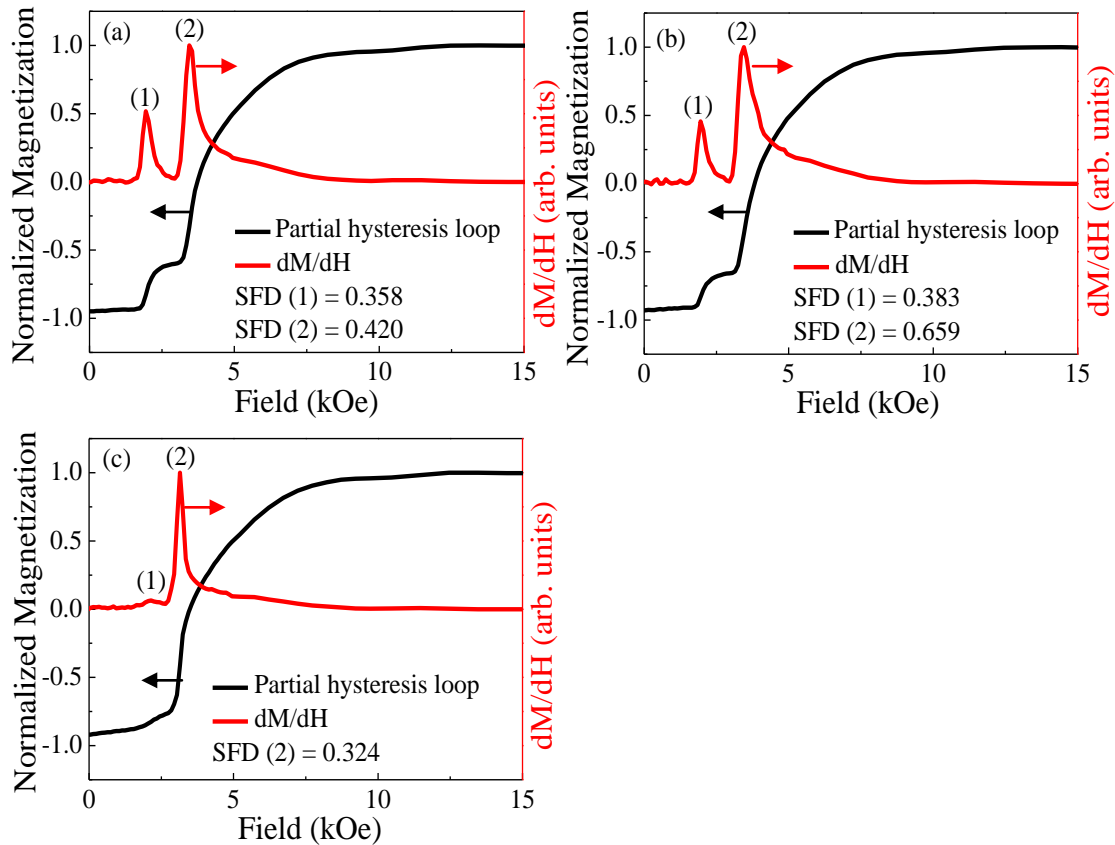
Figure 4.9   Partial hysteresis loops and the derivatives of the partial hysteresis loops, with top and bottom $L1_0$-FePt layer labelled (1) and (2), respectively, for PSVs with Ag post-annealed at (a) 300, (b) 400 and (c) 500 °C.

4.1.4 Current-in-Plane GMR

Figures 4.10(a) to 4.10(d) show the MR loops of the PSVs with Ag post annealed at the various temperatures. GMR ratios of 1.1 and 2.2 % at room temperature and 77 K, respectively, were obtained for the sample with Ag post-annealed at 300 °C. This was higher than that reported previously for room temperature CIP measurement of $L1_0$-FePt based spin valves with Pt and Pd spacers [2]. These

values were also two orders of magnitude higher than those reported using Au spacer and obtained from CPP measurements at 77 K [1], which tended to give a stronger magneto-resistance phenomenon. This could be attributed to Ag being a material that does not depolarize the spins at the $L1_0$-FePt/Ag interface as much as other materials such as Au, Pt and Pd. This was consistent with previous reports of the long spin diffusion length of Ag which enabled large spin accumulation with reduced spin flip scattering [8].
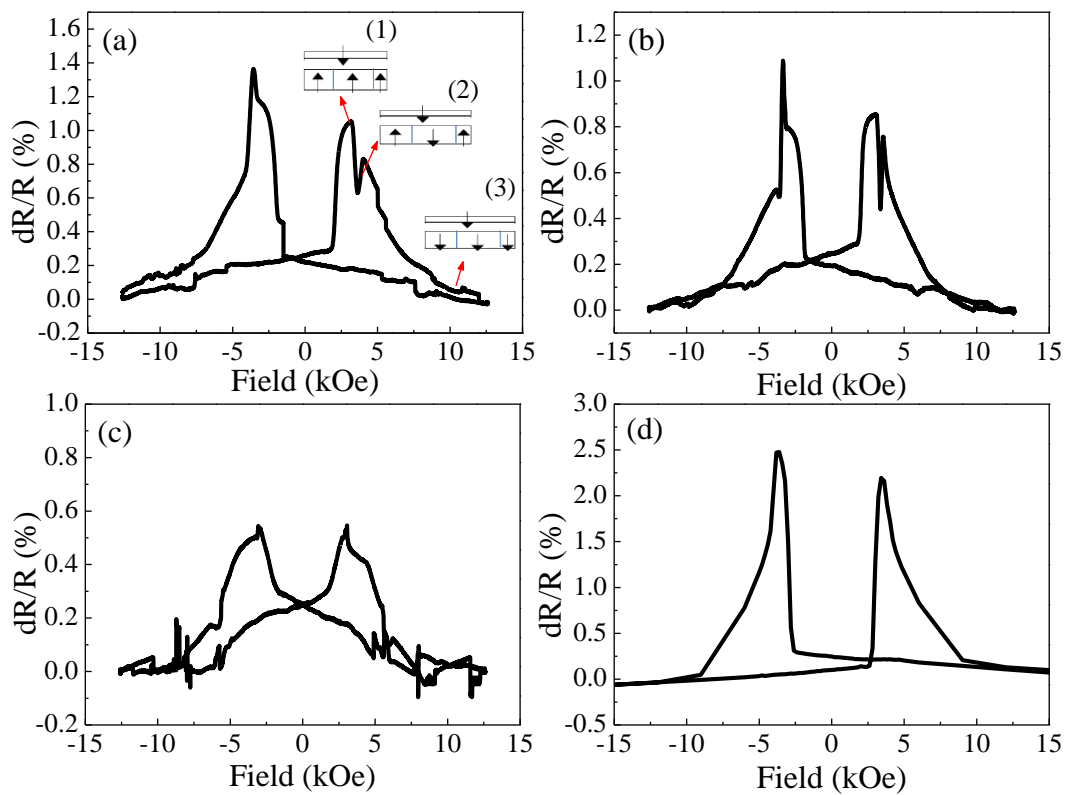
Figure 4.10 MR loops of $L1_0$-FePt/Ag/$L1_0$-FePt PSVs for Ag post-annealed at (a) 300, (b) 400 and (c) 500 °C measured at room temperature and (d) Ag post-annealed at 300 °C measured at 77 K. The inset to (a) illustrates the schematic reversal behaviour as described in the text.

The GMR observed was attributed to the spin dependent scattering of conduction electrons from the $L1_0$-FePt/Ag/$L1_0$-FePt trilayer interfaces as well as the domain walls and granular system within the $L1_0$-FePt layers. When current passed through the trilayer, GMR arose from the asymmetry in the scattering probability of the

spin up and spin down electrons, where an anti-parallel/parallel configuration of the PSV gave a high/low resistance. With high magnetocrystalline anisotropy, a narrow domain wall width δ in the range of 8.25 to 8.40 nm was expected of the bottom $L1_0$-FePt layer (Table 4.1). This allowed domain wall scattering by the randomly aligned domains to contribute to GMR during magnetization reversal of the bottom $L1_0$-FePt layer, which occurred via domain nucleation and propagation [9-12]. A MR ratio of 0.2 % due to domain wall scattering was previously reported in sputtered deposited $L1_0$-FePt films [10]. In addition, as discussed in Section 4.1.3, high temperature post-annealing conditions resulted in the formation of grains within the bottom $L1_0$-FePt layer. Hence, scattering of conduction electrons at the interface of the FePt grains and non-magnetic Ag grain boundaries was also likely to have brought about an enhancement in the GMR effect [13, 14].

Table 4.1   Summary of the magnetic properties of the PSVs with Ag post-annealed at (a) 300, (b) 400 and (c) 500 °C. δ is the estimated domain wall width where $\delta = \pi\sqrt{A/K_u}$, with $A = 10^{-6}$ erg/cm.

Ag Post-annealing Temperature (°C)	Hard Layer K_u (10^7 erg/cm^3)	M_s (emu/cm^3)	Hard Layer Coercivity (kOe)	Soft Layer Coercivity (kOe)	δ (nm)
300	1.44	794	3.86	1.94	8.28
400	1.40	747	3.74	1.99	8.40
500	1.45	799	3.50	/	8.25

With increasing Ag post-annealing temperature, the GMR ratio of the PSV decreased. The reduction of the Ag spacer roughness as a result of the increasing Ag post-annealing temperature had no effect in improving the GMR ratio. The decrease in GMR ratio at the Ag post-annealing temperature of 400 °C was the result of a larger defect density in the bottom $L1_0$-FePt film with a higher degree of

grain formation, as observed from the SFD in Section 4.1.3. The increased presence of grain boundaries reduced the electron mean free path and brought about an increased spin independent scattering [15]. Further increase of the Ag post-annealing temperature to 500 °C resulted in a thinner spacer which could not decouple the bottom and top $L1_0$-FePt layer. Scattering of the conduction electrons at the interfaces of the $L1_0$-FePt trilayer ceased to contribute to the overall GMR with the $L1_0$-FePt layers perpetually assuming a low resistance parallel configuration. Instead, GMR was likely due to the combination of domain wall and granular scattering within the $L1_0$-FePt layers.

There was also a sharp observable discontinuity on both sides of the MR loops (positive and negative applied field) for Ag post-annealed at 300 and 400 °C. When the applied field was in the range between the soft and hard $L1_0$-FePt coercivity, anti-parallel magnetic configuration assumed by the $L1_0$-FePt layers resulted in the initial peak in the GMR ratio [Inset 1 of Figure 4.10(a)]. When the applied field was increased beyond the hard layer coercivity, reversal of the hard $L1_0$-FePt layer magnetization began. Increasing formation of reversed domains within the hard layer with magnetization parallel to that of the soft layer led to a subsequent decline in the GMR ratio. However, the concurrent onset of the combined effects from domain wall and granular scatterings ultimately dominated and brought about the spike in GMR ratio [Inset 2 of Figure 4.10(a)] [16]. At large applied fields, complete reversal of the bottom $L1_0$-FePt layer gave rise to a low resistance parallel magnetic configuration [Inset 3 of Figure 4.10(a)]. It was further observed that the spike at each side of the MR loop was more distinct for Ag post-annealed at 400 °C. This was due to the greater extent of grain formation in the bottom $L1_0$-FePt, as concluded from the SFD, which increased the interfacial area

present for granular scattering. In addition, the asymmetrical MR loops arose possibly due to the asymmetrical skew scattering of spin up and spin down electrons from spin orbit interaction [17-19].

4.1.5 Reversal Mechanism

The reversal behaviour of the PSV with Ag post annealed at 300 °C was investigated by studying the magnetic configurations of both $L1_0$-FePt layers at the intermediate stages of their reversal process. A positive 20 kOe field was first applied to fully saturate the sample. Subsequently, a field in the negative direction between -2 to -8 kOe was applied. AFM and MFM images were then taken at zero field to gain an insight on the magnetic configurations of the layers frozen at its given stage along the first half of the hysteresis loop. Figure 4.11(a) shows the AFM and MFM images of the PSV after saturation in the positive 20 kOe field. A poorly contrasted MFM image mapped closely with its corresponding AFM image. It was more of a reflection of the topography of the sample surface, suggesting complete magnetization saturation with spin down configuration in both $L1_0$-FePt layers.
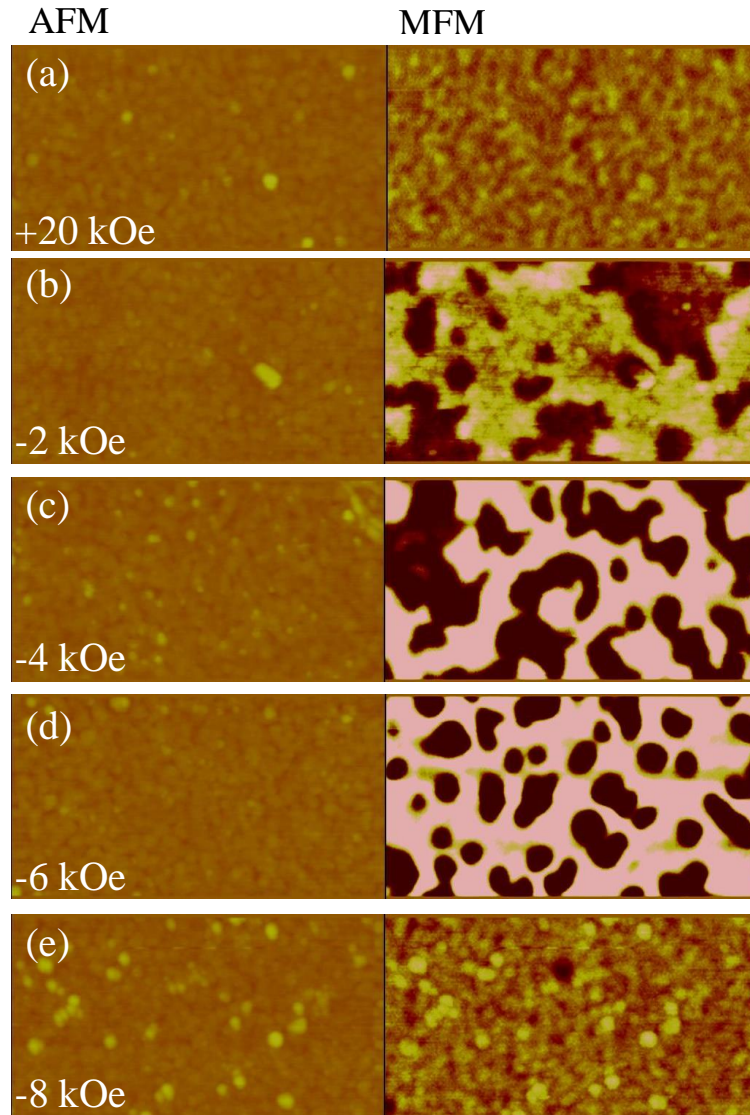
Figure 4.11 2×1 μm^2 AFM and MFM images recorded for (a) completely saturated hard and soft $L1_0$-FePt layers under an applied field of +20 kOe, (b) partial reversal in soft $L1_0$-FePt layer under an applied field of -2 kOe, (c) partial reversal in hard $L1_0$-FePt layer under an applied field of -4 kOe, (d) partial reversal in hard $L1_0$-FePt layer under an applied field of -6 kOe, and (e) close to complete saturation of hard $L1_0$-FePt layer under an applied field of -8 kOe.

When a negative field of -2 kOe was applied [Figure 4.11(b)], reversal of the soft $L1_0$-FePt began with the formation of reversed domains (spin up) followed by domain wall propagation (in yellow). The shape of the domain walls is determined by two factors. The first being domain wall elasticity, which tends to straighten the walls; the second being the presence of pinning sites from defects which adds irregularity to the shape of the domains. The dendritic shape of the reversed

domains observed in the top $L1_0$-FePt was an indication of pinning defects which blocked the propagation path of the reversed domains. This was likely created by the structural disorder due to grain boundaries within the top $L1_0$-FePt layer. High temperature deposition of the top $L1_0$-FePt promoted grain formation with diffused Ag preferentially occupying sites along the high energy grain boundaries. Bright white magnetic regions were also detected near or along the reversed domain walls of the top $L1_0$-FePt layer. These bright regions could be attributed to the decoration of reversed domains in the hard layer by the domain walls in the soft layer. The Bloch walls in the soft layer radiated strong fields to lower the nucleation field in the adjacent hard layer. Combined with the external field applied to reverse the soft $L1_0$-FePt layer, the total field generated could be high enough to reach the coercive field of the hard $L1_0$-FePt, bringing about local reversal in the bottom $L1_0$-FePt layer [20-22].

At a negative field of -4 kOe, complete reversal to a spin up configuration would have taken place in the top $L1_0$-FePt layer and the MFM would only probe the magnetic configurations of the bottom $L1_0$-FePt layer. The bright white regions in Figure 4.11(c) indicates similar switching behaviour of reversed (spin up) domain formation and wall propagation in the bottom $L1_0$-FePt. A more highly contrasted image was obtained compared to Figure 4.11(b) as a stronger perpendicular magnetic stray field was detected from the thicker bottom $L1_0$-FePt layer. With an increase in negative applied field to -6 kOe [Figure 4.11(d)], the proportion of bright regions increased with the propagation of spin up domains through the structural disorder. Domain wall shape became spherical instead of dendritic as the energy from the pinning sites was overcome with greater applied field. Beyond a negative field of -8 kOe [Figure 4.11(e)], close to complete saturation of the

bottom $L1_0$-FePt layer occurred, as reflected from the poorly contrasted MFM image.

4.1.6 Interlayer Coupling within PSV

The influence of the magnetic domain state of the hard $L1_0$-FePt layer on the magnetization reversal of the soft $L1_0$-FePt layer was demonstrated through the exchange bias effect and magnetic properties of the minor hysteresis loops (Figure 4.12).
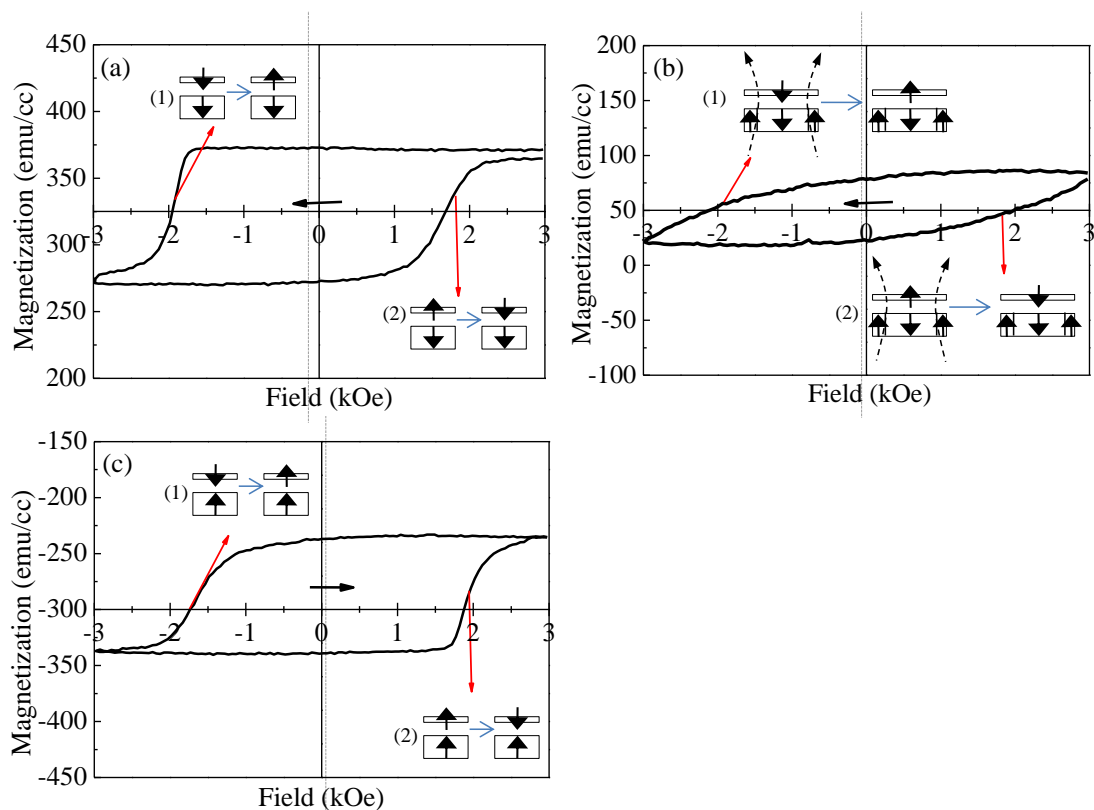
Figure 4.12 Minor hysteresis loops of the $L1_0$-FePt (bottom)/Ag/$L1_0$-FePt (top) PSV recorded under the influence of the different magnetization states of the hard bottom $L1_0$-FePt layer, created through the application of negative fields of (a) 0, (b) -4 and (c) -20 kOe. The dotted line indicates the centre of the minor hysteresis loop; the arrow indicates the direction of the shift of the minor hysteresis loop. Insets illustrate schematically the influence of the bottom $L1_0$-FePt layer on the reversal of the top $L1_0$-FePt layer as described in the text.

A positive field of 20 kOe was first applied to fully saturate both $L1_0$-FePt layers of the PSV in the same spin down direction. A field in the range of 0 to -20 kOe was

applied such that different magnetization states (partial or full saturation) of the bottom $L1_0$-FePt were attained. A minor loop below the switching field of the hard magnetic layer, between +3 to -3 kOe, was then cycled. This allowed the study of the reversal behaviour of the soft layer under the influence of a fully or partially switched hard layer. As shown in Figure 4.12, the system behaved as exchange spring magnets, whereby the minor loops exhibited the exchange bias phenomenon with a shift in the hysteresis loop producing enhanced coercive field in either the positive or negative direction. The difference between the coercivities in the first and second quadrants was termed the interlayer coupling field H_{int}. A summary of the H_{int} and coercive field $H_{coercivity}$ of the soft layer with respect to the applied field is shown in Figure 4.13
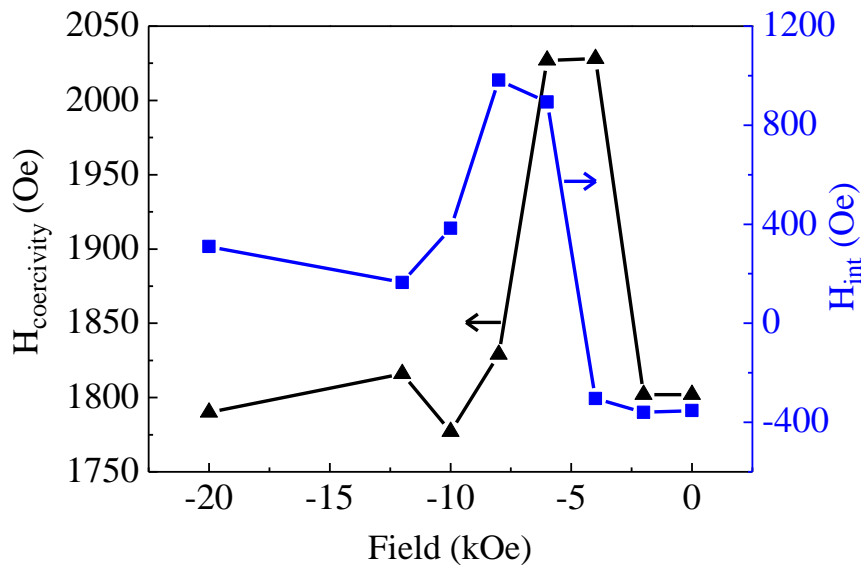
Figure 4.13 Interlayer coupling field H_{int} (■) and coercive field $H_{coercivity}$ (▲) of the soft layer versus applied field.

With zero applied field, H_{int} possessed a negative value (Figure 4.13). The small Ag spacer thickness of 2.5 nm and the relatively large interfacial roughness of 1.1 nm made contributions from direct coupling through pinholes, Ruderman-Kittel-Kasuya-Yosida (RKKY) or Néel coupling considerable [22-26]. At zero applied

field, the magnetic moments in both $L1_0$-FePt layers were close to full saturation and aligned in the positive spin down field direction. When the minor hysteresis loop was cycled, the soft layer (spin down) had to overcome the interlayer magnetostatic coupling with the hard layer (spin down) in order to switch to an anti-parallel spin up configuration [Inset 1 of Figure 4.12(a)] in the second quadrant. In contrast, reversal of the soft $L1_0$-FePt layer (from spin up to spin down) in the fourth quadrant was assisted by the interlayer magnetostatic interactions with the hard layer (spin down) [Inset 2 of Figure 4.12(a)]. This resulted in a negative H_{int}.

With increasing negative field applied, H_{int} increased and attained a positive value. Beyond -4 kOe, the hard layer coercivity was reached and significant reversal of the bottom $L1_0$-FePt began. Taking the extreme case of -20 kOe with uniform magnetization of the bottom $L1_0$-FePt in the spin up configuration, the soft layer magnetization experienced greater resistance to switching when the field for the minor loop was applied from -3 to +3 kOe direction [Inset 2 of Figure 4.12(c)] compared to +3 to -3 kOe [Inset 1 of Figure 4.12(c)]. Thus, a positive H_{int} was achieved with increasing alignment of magnetic moments beyond an applied field of -4 kOe.

As seen from Figure 4.13, H_{int} peaked in the region of -6 to -8 kOe. A larger shift in the centre of the minor loop towards the positive or negative fields (greater H_{int}) reflects a greater extent of the interlayer coupling strength [27]. As such, stronger interlayer coupling existed between the $L1_0$-FePt layers with partial reversal of the bottom $L1_0$-FePt layer. This was due to the influence of stray field dipolar coupling on the top $L1_0$-FePt, induced by the non-uniform magnetization in the bottom $L1_0$-FePt, in addition to the interlayer magnetostatic coupling effect observed in the

scenario of complete saturation of the bottom $L1_0$-FePt layer. Partial reversal of the hard $L1_0$-FePt layer resulted in numerous spin up nucleation domains [Figure 4.11(c)]. Stray field created at the vicinity of these domain walls promoted dipolar coupling between the hard and soft layers. The spin up field created at the internal border of the spin up domains assisted the formation and propagation of spin up domains in the soft $L1_0$-FePt layer when the minor loop was swept from +3 to -3 kOe [Inset 1 of Figure 4.12(b)]. On the other hand, when the minor loop was swept from -3 to +3 kOe, the magnetic reversal of the soft $L1_0$-FePt layer was met with greater resistance as stray field from the bottom $L1_0$-FePt impeded the propagation of reversed spin down domains in the top $L1_0$-FePt [Inset 2 of Figure 4.12(b)]. Dipolar coupling strength would be the strongest when the density of the domain walls within the hard layer reached a maximum with the highest domain density. This occurred around a negative applied field of -4 kOe [Figure 4.11(c)]. The magnetostatic coupling strength would be the strongest upon complete saturation of the hard layer at -10 kOe and beyond (Figure 4.8). The overall coupling strength, being an interplay of both stray field dipolar coupling and interlayer magnetostatic interactions, resulted in H_{int} peaking in the intermediate negative applied field region of -6 to -8 kOe.

It was also observed from Figure 4.13 that a peak in $H_{coercivity}$ occurred with applied negative field in the region of -4 to -6 kOe. The stray field emanating from the partially switched hard $L1_0$-FePt layer created a replication of domains from the hard to the soft $L1_0$-FePt layer. Thus, this magnetic disorder would also impede domain wall propagation within the soft layer. A larger applied field was then needed for the domain walls in the soft $L1_0$-FePt layer to overcome the domain wall pinning and propagate across the stray field pattern. Hence, an increase in

$H_{coercivity}$ of the minor loop occurred with increasing magnetic disorder in the soft layer due to the large stray field from the hard layer.

With complete saturation of the bottom $L1_0$-FePt [Figures 4.12(a) and (c)], the minor loops exhibited high remanence and rapid magnetic reversal near the coercive field. For an ideal infinite thin film with complete saturation, single domain existed and no stray field was contributed by the bottom $L1_0$-FePt layer. Hence, dipolar interaction between the two $L1_0$-FePt layers was minimized and relatively stronger decoupling was achieved. On the other hand, the minor loop exhibited sheared behaviour and low remanence [Figure 4.12(b)] with partial reversal of the bottom $L1_0$-FePt. The switching mechanism of the soft $L1_0$-FePt layer became more complex as the fringing field from the hard $L1_0$-FePt domain walls caused the domain nucleation field to be locally reduced in the adjacent soft $L1_0$-FePt layer [22]. As such, domain formation occurred non-uniformly within the softer $L1_0$-FePt layer and over a larger range of applied field.

4.2 Atomistic Modelling and Analysis

In this section, an atomistic spin model was utilized to simulate and gain further understanding of the magnetic, interfacial and reversal properties of these fabricated PSVs.

4.2.1 Description of Atomistic Model

In this atomistic spin model, the energies of the system of interacting spins are described by a classical spin Hamiltonian of the form:

$$\mathcal{H} = -\sum_{ij} J_{ij} \boldsymbol{S}_i \boldsymbol{S}_j - \sum_i K_i \boldsymbol{S}_z^2 - \sum_i \mu_i \boldsymbol{H} \boldsymbol{S}_i \tag{4.1}$$

The first term describes the exchange coupling between two neighbouring spins i and j, where J_{ij} is the exchange constant between the two spins and S_i and S_j are the spin moments of i and j, respectively. The second term describes the magneto-crystalline anisotropy of the spin, where K_i is the anisotropy energy per atom. The last term is a Zeeman constant which represents the interaction of an externally applied field H with the spin system, where μ_i is the magnetization of atom. The magnitude of the exchange coupling energy is the strongest, followed by the magneto-crystalline anisotropy and the Zeeman term.

The dynamics of the spin system are described by the Landau-Liftshitz-Gilbert (LLG) equation with Langevin Dynamics. In its standard form, the LLG equation is strictly applicable to simulations at zero temperature; Langevin Dynamics takes into account the effects of thermal fluctuation with a Gaussian white noise term ζ_i:

$$\frac{\partial S}{\partial t} = -\frac{\gamma}{(1+\lambda^2)}[S \times H + \lambda S \times (S \times H)] \tag{4.2}$$

where γ is the gyromagnetic constant, λ is the damping constant and H is the effective magnetic field obtained from the derivative of spin Hamiltonian and the additional white noise term, $H = -\frac{1}{\mu_i}\frac{\partial \mathcal{H}}{\partial S} + \zeta_i$. An increase in the temperature is represented by an increase in the width of the Gaussian distribution. The first term describes the precession of the spin about H. The second term describes the damping torque which brings the spin back to its lowest energy state along the effective field H direction. The larger is the damping constant, the faster will the spin moment be aligned along the effective field direction. The damping constant for magnetic materials typically lies between 0.01 and 0.1. The maximum damping constant attainable is 1.

The FePt layers were simulated as a generic ferromagnet with a Curie temperature (T_c) of 800 K, and uniaxial K_u of 1.1×10^6 J/m^3 and 2.2×10^6 J/m^3 for the top and bottom layers, respectively, representing different degrees of $L1_0$ ordering. The Ag spacer layer was simulated as a paramagnet with a T_c of 8 K. The paramagnetic behaviour of the spacer at temperatures greater than 8 K replicated the physical behaviour of induced order near the FePt surface, while having no intrinsic order. Experimentally, the PSVs were made up of layers of continuous thin films. In this model, a vertical slice with dimensions of $5 \times 5 \times 27.5$ nm was simulated, having the same layer thicknesses as the experimental PSVs but a much smaller lateral dimension.

Due to the high temperature fabrication conditions, diffusion between the different layers was expected to take place. In this atomistic model, the interlayer diffusion is controlled by the introduction of the following function for each material

$$\tanh\left(\frac{x}{aL}\right) \tag{4.3}$$

where x is a position within the PSV, a is the intermixing factor and L is the total length of the PSV system (27.5 ± 1.5 nm). The larger the intermixing factor a, the greater would be the degree of intermixing at the FePt and Ag interface (Figure 4.14). In this model, Ag and FePt were assumed to have the same diffusion rates. The intermixing factor of the top FePt/Ag interface (a_t), bottom FePt/Ag interface (a_b) and thickness of the Ag layer (t) were varied to model the conditions within the PSVs, where the Ag spacer was subjected to post-annealing treatment at the different temperatures. The simulated PSVs with Ag post-annealed at 300, 400 and 500 °C are henceforth referred as PSV-300, PSV-400 and PSV-500, respectively.

Figure 4.14 Schematic illustration of the dependence of Ag/FePt intermixing on intermixing factor a. Absence of intermixing when $a = 0$ (solid line). The extent of intermixing increases with increasing value of a, when $a > 0$ (dashed line to dotted line).

4.2.2 Atomistic Simulation Results and Discussion

The values of a_t, t and a_b for the simulated PSVs with the Ag spacer post-annealed at the various temperatures are summarized in Table 4.2. The a_t was assigned a value of 0.02 across the simulated samples as the top FePt layer in all the PSVs were deposited at a high temperature of 300 °C to attain $L1_0$ ordering. Ag is immiscible in FePt and the diffused Ag atoms would tend to reside along the high energy grain boundaries [5, 6]. As such, an increase in the post-annealing temperature of Ag led to a greater degree of diffusion of the Ag atoms into the bottom FePt layer as well as the grain boundaries. This was represented by an increasing a_b and a diminishing t respectively.

Table 4.2   Intermixing factor of the top FePt/Ag interface (a_t), thickness of the Ag layer (t), intermixing factor of the bottom FePt/Ag interface (a_b) as well as the corresponding magnetic ordering generated in Ag for PSV-300, PSV-400 and PSV-500.

Simulated PSV	a_t	t (nm)	a_b	Degree of induced magnetic ordering in Ag
PSV-300	0.02	2.5	0.02	0.258
PSV-400	0.02	2.0	0.025	0.357
PSV-500	0.02	1.5	0.03	0.527

Figure 4.15 shows the simulated hysteresis loops of the PSV-300, PSV-400 and PSV-500, whereby decoupling between the top and bottom FePt layers was no longer present at a Ag post-annealing temperature of 500 °C. Increasingly extensive bottom FePt/Ag interlayer diffusion with higher post-annealing temperature resulted in a larger number of Ag atoms in contact with the FePt atoms. The magnetic moments of the surrounding FePt atoms would polarize the Ag atoms. The polarizing effect on Ag became greater with a larger degree of intermixing, which in turn exerted a greater influence on the independent switching of the FePt layers. An increase in the induced magnetic ordering of the Ag spacer was observed with increasing Ag post-annealing temperature (Table 4.2). This suggested that an increasingly polarized Ag spacer contributed to the increased effective exchange coupling between the FePt layers. Furthermore, diffusion of the Ag atoms to the grain boundaries at a higher Ag post-annealing temperature gave rise to a reduced spacer thickness (Figure 4.16), which could have been too thin to bring about complete decoupling between the top and bottom FePt layer.
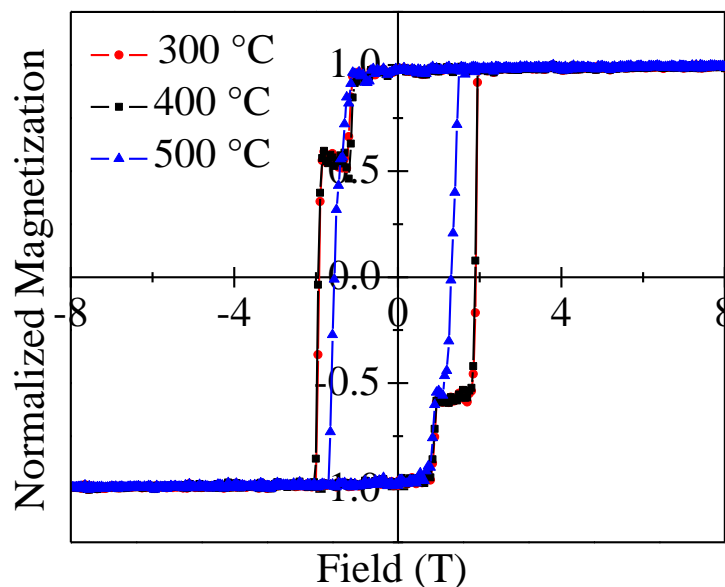
Figure 4.15 Simulated hysteresis loops of PSV-300, PSV-400 and PSV-500.
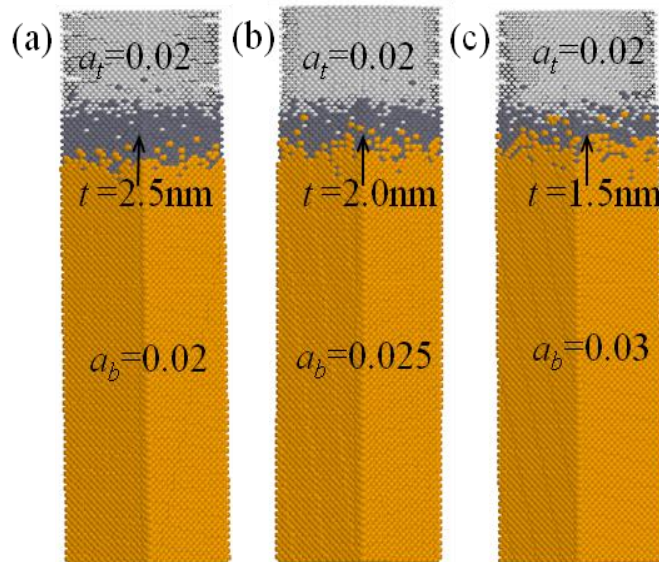
Figure 4.16 Schematic illustrations of the simulated FePt/Ag/FePt PSVs with varying Ag post-annealing temperatures of (a) 300, (b) 400 and (c) 500 °C.

Although the simulated results were in good agreement with experimental data, where a thinner Ag spacer (Figure 4.3) along with coupling behaviour between the $L1_0$-FePt layers (Figure 4.8) were observed at a Ag post-annealing temperature of 500 °C, the simulated hysteresis loop deviated slightly from experimental. Complete magnetization reversal took place instantaneously at the coercive field, unlike that observed from experimental results. This was attributed to the small simulation dimensions in atomistic modelling in which focus was placed on a single grain rather than on a multiple grain structure observed experimentally. As such, intergrain exchange interactions within the FePt layers were neglected in the model. Furthermore, a perfect lattice model was assumed in the simulation whereas fabricated samples were unlikely to be defect free. Coercivity values obtained from simulation results were also much higher than experimental ones due to the smaller simulated sample dimensions.

A rougher and more poorly defined interface was observed along with increasing intermixing factor (Figure 4.16). Interfacial scattering and spin accumulation at the

interface are of utmost importance to the MR of the PSV structure. The atomically rougher interface could have led to a greater degree of spin flipping and reduced spin accumulation, thus contributing to the decrease in GMR ratio with increasing Ag post-annealing temperature, as observed experimentally.

The switching mechanism of the FePt layers in the PSV-300 and PSV-500, in the presence and absence of interlayer decoupling, respectively, was investigated by studying the magnetic moments of the FePt and Ag atoms at different stages of the hysteresis cycle (Figure 4.17). Earlier experimental study of a 2×1 μm^2 region of the $L1_0$-FePt PSV (Section 4.1.5) concluded a reversal mechanism made up of domain nucleation and wall propagation. In this 5×5 nm^2 atomistic model, the effects of interlayer coupling on the reversal of the FePt layers within a single grain are examined.
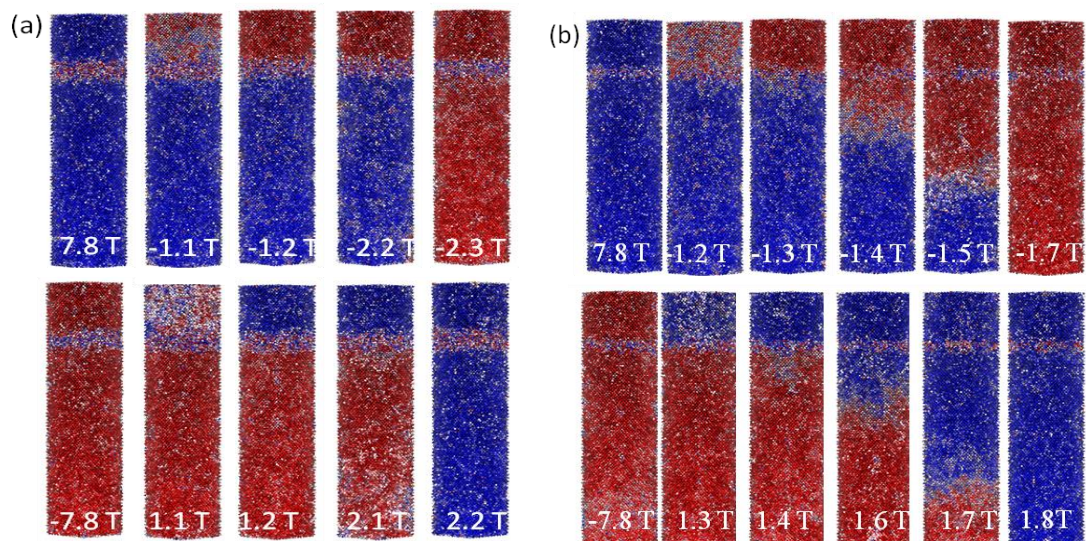
Figure 4.17 Schematic representations of the magnetization states of the Ag and FePt atoms at various applied fields along the hysteresis loops for the (a) PSV-300 and (b) PSV-500. Spin up, spin down and in-plane magnetizations are represented in blue, red and white, respectively.

In both PSV-300 and PSV-500, all the FePt atoms possessed spin up magnetization (blue) under a positive saturation field of 7.8 T [Figures 4.17(a) and (b)]. The Ag

atoms possessed a randomized combination of spin up (blue), spin down (red) and in plane (white) magnetization due to its paramagnetic nature at 300 °C. Upon reaching the coercive field of the top FePt layer, in the range of 1.1 to 1.3 T, reversal occurred simultaneously and coherently and spin down magnetization (red) of the top FePt layer was attained. On the other hand, reversal of the bottom FePt layer differed for the PSV-300 and PSV-500. For the PSV-300, coherent rotation of the bottom FePt was observed. When the post-annealing temperature of the Ag spacer was 500 °C in PSV-500, reversal of the bottom FePt became incoherent. Magnetization reversal began at the region where the bottom FePt layer was closest to the Ag spacer, followed by the subsequent propagation of reversed domains through the remaining portion. Based on the reversal schematic diagram in Figure 4.17, the switching fields of the bottom and top FePt layers occurred within a closer coercivity range when the Ag spacer was post-annealed at 500 °C compared to that at 300 °C. Exchange coupling between the FePt layers became more dominant at a higher post-annealing temperature due to the thinner Ag spacer layer. As such, initial nucleation of reversed domains in the bottom FePt layer occurred under the assistance of exchange interaction with the top FePt layer. This took place at the region near the Ag spacer where exchange interaction was the strongest due to closer proximity between the FePt layers. At the same time, the increasing presence of reversed polarized Ag near the interface of the bottom FePt layer could also have contributed to the initial reversed domains formation at this region.

4.3 Micromagnetic Modelling and Analysis

In Section 4.2, an atomistic model based on a single grain structure was used to simulate the $L1_0$-FePt/Ag/$L1_0$-FePt PSV system. However, experimental results showed that the FePt layers were granular films where lateral intergrain exchange

interactions existed. Therefore, a micromagnetic model which uses a multiple grain bilayer structure with lateral intergrain exchange coupling was used to investigate the PSVs, providing a more accurate alternative representation, on top of the atomistic model.

4.3.1 Description of Micromagnetic Model

The micromagnetic model simulates a granular bilayer structure (Figure 4.18), which is representative of the bottom fixed and top free $L1_0$-FePt layers.
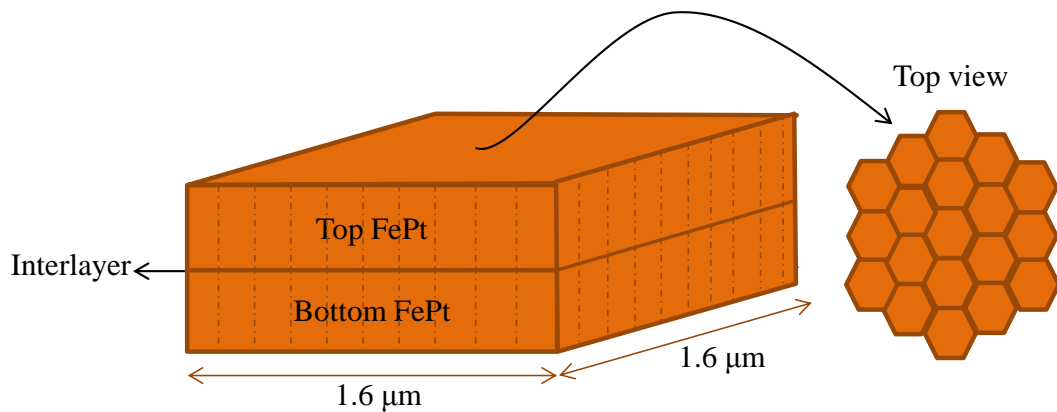
Figure 4.18 Schematic illustration of the simulated bilayer structure.

Each granular FePt layer possesses a mean grain size of 20 nm. The grain structure in the plane is modelled using a two-dimensional voronoi construction, which naturally leads to a grain size distribution as well as a distribution in the exchange coupling between neighbouring grains. Each grain is small enough to be considered a single domain, and is modelled using the micromagnetic Landau-Lifshitz-Bloch (LLB) equation of motion [28]. Conventional LLG micromagnetic calculations for spin systems lack the correct description of the temperature effects because of the assumption of a constant magnetization length. The primary advantage of the LLB approach over the more commonly used micromagnetic LLG calculations is the natural treatment of thermal effects, including the distinct

transverse and longitudinal magnetization fluctuations as well as the ability to simulate heating through the Curie point [28-30]. Although high temperatures are not relevant for this work (all simulations are performed at room temperature), the LLB generally provides a more rigorous micromagnetic formalism valid at all temperatures. The LLB equation, which takes into account the longitudinal relaxation processes, is also important for the studies of the magnetization dynamics of high anisotropy materials and as such is a better approach.

The parameters used for the $L1_0$-FePt magnetic layers are derived from the density functional theory and atomistic spin simulations using a multi-scale approach described in detail in [30]. The only alteration made to the parameters is the scaling of the anisotropy (given by the transverse susceptibility) to denote different degrees of chemical $L1_0$ ordering in the two layers. In order to represent the thermodynamic thermal fluctuations, the stochastic form of the LLB is utilized and the equation of motion for each spin is given by [31]:

$$\dot{m} = \gamma[m \times H_{eff}] + \frac{|\gamma|\alpha_{\parallel}}{m^2}(m \cdot H_{eff})m - \frac{|\gamma|\alpha_{\perp}}{m^2}\Big[m \times \big[m \times (H_{eff} + \eta_{\perp})\big]\Big] + \eta_{\parallel} \quad (4.4)$$

where $m = M_s/M_0$ is the magnetization normalized to its zero-temperature value, γ is the gyromagnetic ratio, $\alpha_{\perp}$ and $\alpha_{\parallel}$ are the dimensionless temperature dependent longitudinal and transverse damping parameters, and $\eta_{\perp}$ and $\eta_{\parallel}$ are the transverse and longitudinal noise terms given by

$$\langle \eta_i^{\mu} \rangle = 0,$$

$$\langle \eta_i^{\perp}(0)\eta_j^{\perp}(t) \rangle = \frac{2k_B T(\alpha_{\perp} - \alpha_{\parallel})}{|\gamma|M_s^0 V \alpha_{\perp}^2} \delta_{ij}\delta(t),$$

$$\langle \eta_i^{\parallel}(0)\eta_j^{\parallel}(t) \rangle = \frac{2|\gamma|k_B T\alpha_{\parallel}}{M_s^0 V} \delta_{ij}\delta(t),$$

$$\langle \eta_i^{\parallel} \eta_j^{\perp} \rangle = 0. \tag{4.5}$$

The effective field H_{eff} below T_c is given by

$$H_{\text{eff}} = H + H_{\text{A}} + \frac{1}{2\tilde{\chi}_{\parallel}} \left(1 - \frac{m^2}{m_e^2}\right) m \tag{4.6}$$

where $\tilde{\chi}_{\perp}$ and $\tilde{\chi}_{\parallel}$ are the transverse and longitudinal susceptibilities, respectively and m_e is the equilibrium magnetization [30].

The high PMA of $L1_0$-FePt dictates the preferable formation of domains which are perpendicular to plane (Figure 4.18) [32]. Magnetization parallel to the out-of plane direction is favoured to reduce the magnetocrystalline energy in $L1_0$-FePt with quality factor, $Q = K_u/2\pi M_s^2$, greater than 1. Each grain is also hexagonally shaped and surrounded by 6 neighbouring grains. Each simulated FePt layer consists of a total of 6400 grains. With 80 grains on each edge of the simulated sample, a sample dimension of 1.6×1.6 μm^2 is simulated. Epitaxial behavior across the FePt layers is modelled with an array of perpendicularly magnetized top FePt grains grown grain-on-grain on the bottom FePt grains. There is no physical representation of the Ag spacer in this model but its effects are modelled by the interlayer coupling strength between the grains of the FePt layers.

The interlayer coupling contributions are viewed collectively as the interlayer coupling field (H_{inter}) in this model. The interlayer interaction field H_{pq}^{inter} acting between two adjacent epitaxial grains across the FePt layers is described by Equation (4.7)

$$H_{pq}^{inter} = \bar{H}_{inter} \sum f_{pq} \frac{A_{pq}}{A_a} \cdot \frac{L_a}{L_{pq}} \tag{4.7}$$

where $\bar{H}_{inter}$ is the mean interlayer field, A_{pq} is the contact area, L_{pq} is the contact length, A_a is the mean contact area and L_a is the mean contact length between each pair of columnar FePt grains. The interlayer coupling field dispersion (d_{inter}), which expresses a distribution of the interlayer coupling field, is introduced through the Gaussian term f_{pq}. The interlayer fraction of decoupled grains (f_{inter}) expresses the extent to which the two FM layers are decoupled. A value of 0 for the f_{inter} indicates that all 6400 pairs of epitaxial grains are coupled, while a value of 0.5 indicates that 3200 pairs of randomly selected grains are coupled.

Within the top and bottom FePt layers, the inter-grain interaction is controlled by the strength of the intralayer exchange interaction field (H_{intra}), exchange field dispersion (d_{intra}) and fraction of exchange decoupled grains (f_{intra}). The exchange interaction field H_{ij}^e acting between two neighbouring grains within the FePt layer is approximated using Equation (4.8)

$$H_{ij}^e = \bar{H}_{exchange} \sum f_{ij} \frac{A_{ij}}{A_m} \cdot \frac{L_m}{L_{ij}} \tag{4.8}$$

where $\bar{H}_{exchange}$ is the mean exchange interaction field, A_{ij} is the contact area, L_{ij} is the contact length, A_m is the mean contact area and L_m is the mean contact length between the two neighbouring FePt grains. Disorder in the exchange interaction between the grains is introduced through the Gaussian term f_{ij}. f_{intra} and takes into account the number of grains which would be mutually affected by one another. A value of zero indicates that a grain is exchanged coupled to all 6 neighbouring grains, while a value of 0.5 corresponds to the exchange coupling of a grain to 3 random neighbouring grains.

The perpendicular MR of the PSVs is determined based on the difference in the magnetization angle between all the epitaxial grains, using the simple model [33]

$$\sum_1^{6400} \frac{[1 - \cos\varphi]}{2}$$ (4.9)

where $\varphi = \theta_{bottom} - \theta_{top}$ is the difference in the average spin moment angle between each epitaxial grain on the adjacent FePt layers. θ is the angle which the average magnetic spin moment makes with the z-axis. It is derived from $\cos^{-1}(m_z)$, where m_z is the unit vector of the resultant magnetization in the z direction. The resultant MR loop generated would not reflect an actual GMR ratio as the calculation here is a very much simplified one that assumes excellent spin accumulation at the FePt/Ag interface, perfect matching of the FePt and Ag band structures, as well as a defect free crystal with a long spin diffusion length which does not contribute to spin independent flipping. However, the fractional MR values obtained would provide an adequate qualitative comparison of the variation in MR of the PSVs with different Ag post-annealing temperatures. A value of 1 for the fractional MR signifies that all the grains in the bottom FePt are oppositely magnetized with respect to the epitaxial grains in the top FePt.

Experimentally, it was observed that the increase in the post-annealing temperature of Ag led to a more extensive FePt/Ag interlayer diffusion (Figure 4.3). The consequent thinning of the Ag spacer from 2.2 to 1.4 nm when the Ag spacer was post-annealed at 300 and 500 °C, respectively, resulted in the loss of decoupling within the PSV. The interlayer coupling field (H_{inter}) and fraction of exchange decoupled grains within the fixed FePt (f_{bottom}) were varied to simulate the scenario of increased FePt(bottom)/Ag interdiffusion with increasing Ag post-annealing

temperature (Table 4.3). The H_{inter} was increased with increasing Ag post-annealing temperature to model the effects of an increasingly thinner Ag spacer. In addition, more extensive Ag diffusion to the high energy grain boundaries was also expected. Hence, higher f_{bottom} values were used to indicate greater grain formation at higher post-annealing temperatures. The fraction of exchanged decoupled grains within the top FePt layer (f_{top}) was maintained at the same value across the PSVs as the experimental deposition temperature of the top FePt layer was unchanged. The bottom fixed and top free $L1_0$-FePt layers possessed intralayer exchange fields of 35 kOe and magnetic anisotropies of 1.39×10^7 and 1.69×10^6 erg/cm^3, respectively. The simulated PSVs with Ag post-annealed at 300, 400 and 500 °C are henceforth referred as PSV-300 °C, PSV-400 °C and PSV-500 °C, respectively.

Table 4.3 Interlayer coupling field (H_{inter}), fraction of exchange decoupled grains within the fixed FePt (f_{bottom}) and fraction of exchange decoupled grains within the free FePt layer (f_{top}) for PSV-300 °C, PSV-400 °C and PSV-500 °C.

Simulated PSV	H_{inter} (Oe)	f_{bottom}	f_{top}
PSV-300 °C	50	0.25	0.05
PSV-400 °C	400	0.30	0.05
PSV-500 °C	4500	0.32	0.05

4.3.2 Micromagnetic Simulation Results and Discussion

Simulated hysteresis loops (Figure 4.19) based on the micromagnetic model show better agreement with experimental results (Figure 4.8) compared to the atomistic model (Figure 4.15). The hysteresis loops indicated a gradual change to magnetization saturation in accordance with the experimental results, instead of an instantaneous reversal at the coercive field in the atomistic model. However, the

coercivities obtained for the simulated PSVs (Figure 4.19) were larger compared to the experimental values (Figure 4.8) due to the assumption of a single domain in every grain. Grains in the fabricated samples may be large enough to contain several domains, which would result in a reduction in coercivities. Figure 4.19 shows that the simulated PSV-300 °C and PSV-400 °C were well decoupled but the decoupling between the FePt layers ceased to exist in the simulated PSV-500 °C.
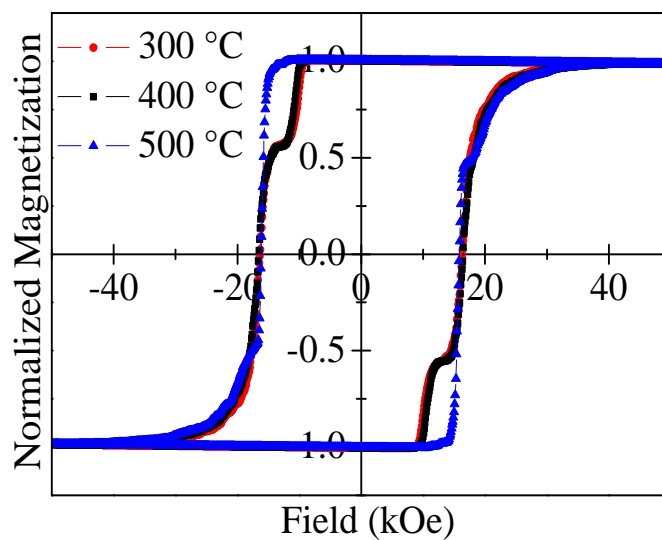
Figure 4.19 Simulated hysteresis loops of the PSV-300 °C, PSV-400 °C and PSV-500 °C.

Figures 4.20(a)-(d) and 4.21(a)-(h) show the magnetic configuration snapshots during the reversal process of both FePt layers for the simulated PSV-300 °C. The reversal mechanism occurred via reversed domain formation (in red) and subsequently domain wall propagation. The reversal mechanism and domain size of the simulated PSV were consistent with those observed experimentally [Figures 4.20(e), 4.21(i) and 4.21(j)].
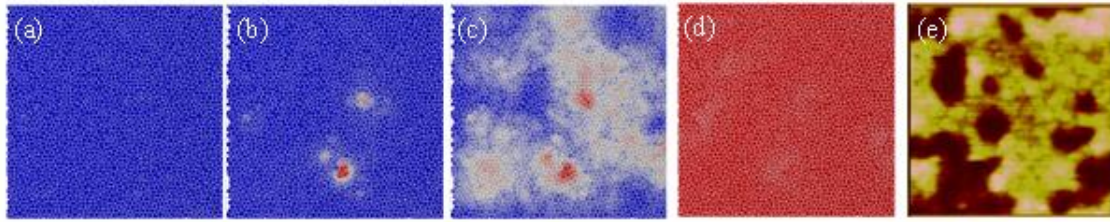
Figure 4.20 Magnetization configurations of the top FePt layer, with a cross section of $1 \times 1 \ \mu m^2$, at an applied field of (a) -10, (b) -11, (c) -12 and (d) -14 kOe for the PSV-300 °C. Spin up, spin down and in-plane magnetizations are represented in red, blue and white, respectively. (e) $1 \times 1 \ \mu m^2$ AFM image illustrating the magnetization configurations of the top FePt layer at an applied field of -2 kOe for the experimentally fabricated PSV with Ag post-annealed at 300 °C. Bright regions represent the reversed domains.
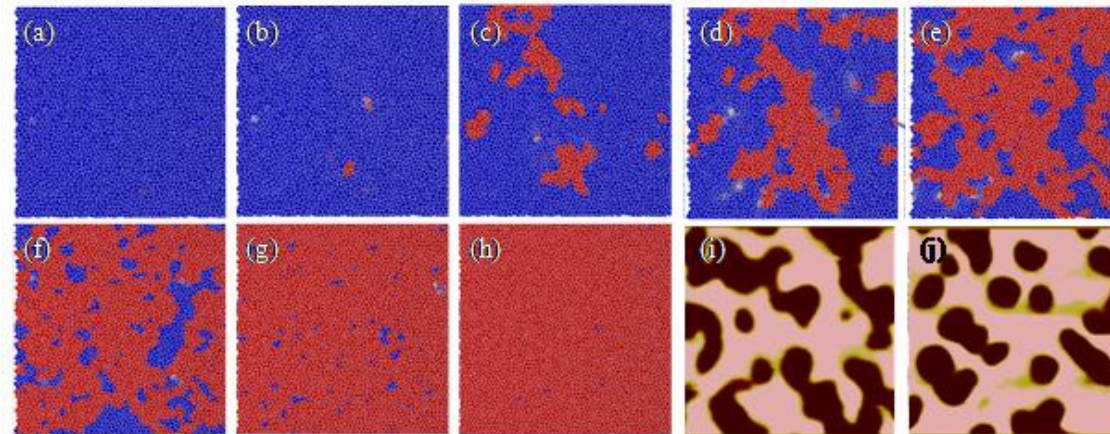
Figure 4.21 Magnetization configurations of the bottom fixed FePt layer, with a cross section of $1 \times 1 \ \mu m^2$, at an applied field of (a) -10, (b) -12, (c) -17, (d) -18, (e) -19, (f) -20, (g) -30 and (h) -50 kOe for the PSV-300 °C. Spin up, spin down and in-plane magnetizations are represented in red, blue and white, respectively. $1 \times 1 \ \mu m^2$ AFM image illustrating the magnetization configurations of the top FePt layer at an applied field of (i) -4 and (j) -6 kOe for the experimentally fabricated PSV with Ag post-annealed at 300 °C. Bright regions represent the reversed domains.

The top FePt reversed more rapidly and over a narrower SFD. This was attributed to the smaller extent of decoupled grain formation within the top FePt which was not influenced by the bottom FePt/Ag interdiffusion. As such, the reversal of the top FePt occurred more coherently instead of independently as in the case of the more decoupled bottom FePt. In addition, stray fields emanating from the top FePt

[Figure 4.20(b)] reduced the nucleation field of the bottom FePt locally [Figure 4.21(b)], resulting in the preferential formation of reversed domains at the adjacent site on the bottom FePt. These nucleation sites subsequently became the centre for further reversed domain propagation with increasing negative applied field. Similar reversal mechanism and stray field effects were observed for the simulated PSV-500 °C. Reversal of the top soft FePt layer also proceeded more rapidly than the bottom hard FePt layer. This was an indication that even though the FePt layers appeared to be coupled on the hysteresis loop for the simulated PSV-500 °C, the increased coupling strength due to the thinner Ag spacer was not sufficiently strong enough to result in the concurrent reversal of both FePt layers.

Figure 4.22 shows the calculated MR loops of the simulated PSV-300 °C and PSV-500 °C. The fractional MR of the PSVs decreased from 0.964 to 0.309 with an increase in Ag post-annealing temperature from 300 to 500 °C. On the other hand, the simulated MR loop for the PSV-400 °C (not shown here) was similar to that of PSV-300 °C, only with a slightly smaller fractional MR of 0.952. These trends were in line with observations made of the CIP MR in the fabricated PSVs (Figure 4.10). For the simulated PSV-500 °C, the considerable decrease in fractional MR was attributed to the larger number of epitaxial grains in both FePt layers possessing magnetization of identical configurations, due to the significant increase in interlayer coupling between the FePt layers. However, a small MR was still present despite the absence of interlayer decoupling as the reversal of both FePt layers did not occur concurrently. In addition, the increase in MR set in at a much larger applied field as the coercive field of the softer top FePt layer increased due to the exchange interaction with the harder bottom FePt layer. The decline in the MR with increasing applied field also occurred more gradually as the increase in

the fraction of decoupled grains in the bottom FePt layer reduced the intergrain exchange coupling and promoted more independent reversal amongst grains. As such, reversal of the bottom FePt layer and the consequent reduction in MR occurred more gradually over a broader range of applied field.
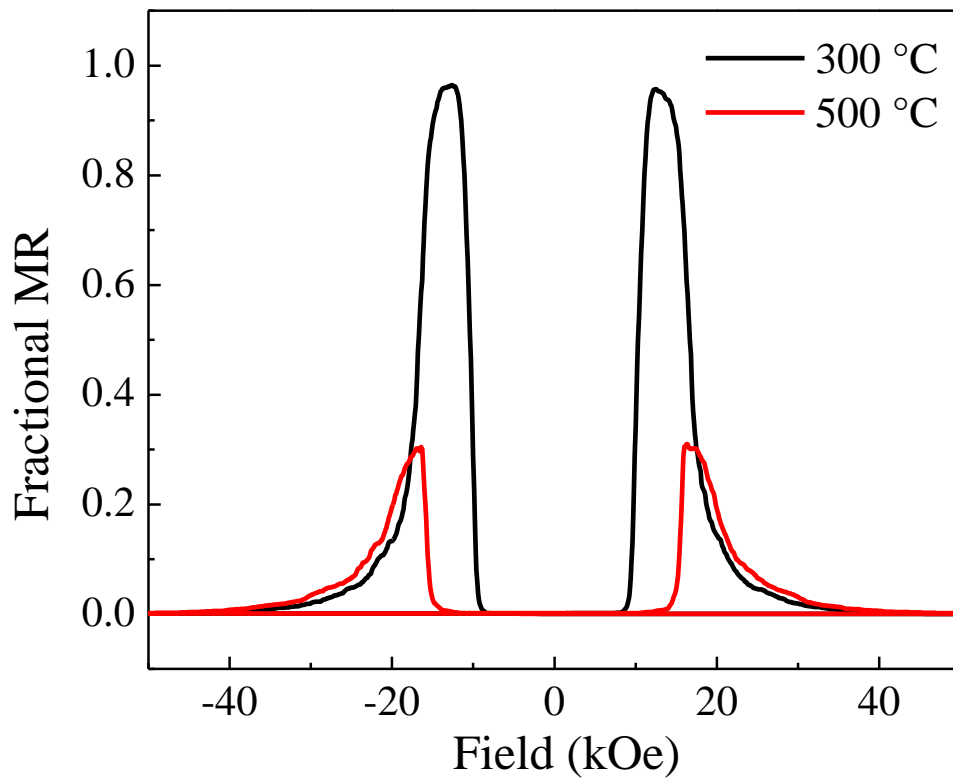
Figure 4.22 MR loops of the simulated PSVs with Ag post-annealed at 300 and 500 °C.

References

1.   T. Seki, S. Mitani, K. Yakushiji, and K. Takanashi, Appl. Phys. Lett. **89**, 172504 (2006).

2.   A. P. Mihai, J. P. Attané, L. Vila, C. Beigné, J. C. Pillet and A. Marty, Appl. Phys. Lett. **94**, 122509 (2009).

3.   Y. Hsu, S. Jeong, D. E. Laughlin, and D. N. Lambeth, J. Magn. Magn. Mater. **260**, 282 (2003).

4.   Z. L. Zhao, J. S. Chen, J. Ding, J. B. Yi, B. H. Liu, and J. P. Wang, Appl. Phys. Lett. **88**, 052503 (2006).

5.   S. Thongmee, B. H. Liu, J. Ding, and J. B. Yi, Thin Solid Films **518**, 7053 (2010).

6.   S. C. Chen, P. C. Kuo, A. C. Sun, C. Y. Chou, Y. H. Fang, and S. Y. Kuo, IEEE Trans. Magn. **41**, 3340 (2005).

7.   T. Hauet, S. Florez, D. Margulies, Y. Ikeda, B. Lengsfield, N. Supper, K. Takano, O. Hellwig, and B. D. Terris, Appl. Phys. Lett. **95**, 222507 (2009).

8.   T. Kimura and Y. Otani, Phys. Rev. Lett. **99**, 196604 (2007).

9.   S. Ishio, T. Yoshino, H. Saito, T. Suzuki, and K. Ohuchi, J. Magn. Magn. Mater. **239**, 217 (2002).

10. K. M. Seemann, V. Baltz, M. Mackenzie, J. N. Chapman, B. J. Hickey, and C. H. Marrows, Phys. Rev. B **76**, 174435 (2007).

11. D. Ravelosona, A. Cebollada, F. Briones, C. Diaz-Paniagua, M. A. Hidalgo, and F. Batallan, Phys. Rev. B **59**, 4322 (1999).

12. A. D. Kent, J. Yu, U. Rüdiger, and S. S. P. Parkin, J. Phys.: Condens. Matt. **13**, R461 (2001).

13. A. Granovsky, F. Brouers, A. Kalitsov, and M. Chshiev, J. Magn. Magn. Mater. **166**, 193 (1997).

14. S. J. Guilfoyle, R. J. Pollard, and P. J. Grundy, J. Phys. D: Appl. Phys. **29**, 29 (1996).

15. E. M. Ho, A. K. Petford-Long, and A. Cerezo, J. Magn. Magn. Mater. **192**, 431 (1999).

16. A. P. Mihai, J. P. Attané, A. Marty, P. Warin, and Y. Samson, Phys. Rev. B **77**, 060401 (2008).

17. A. Gerber, A. Milner, M. Karpovsky, B. Lemke, H. -U. Habermeier, J. Tuaillon-Combes, M. Négrier, O. Boisron, P. Mélinon, and A. Perez, J. Magn. Magn. Mater. **242-245**, 90 (2002).

18. O. Shaya, M. Karpovski, and A. Gerber, J. Appl. Phys. **102**, 043910 (2007).

19. K. M. Seemann, Y. Mokrousov, A. Aziz, J. Miguel, F. Kronast, W. Kuch, M. G. Blamire, and AT. Hindmarch, Phys. Rev. Lett. **104**, 076402 (2010).

20. A. P. Mihai, J. P. Attané, L. Vila, C. Beigné, J. C. Pillet, and A. Marty, Appl. Phys. Lett. **94**, 122509 (2009).

21. P. de Person, P. Warin, M. Jamet, C. Beigne, and Y. Samson, Phys. Rev. B **76**, 184402 (2007).

22. H. W. Fuller and D. L. Sullivan, J. Appl. Phys. **33**, 1063 (1962).

23. V. Baltz, A. Marty, B. Rodmacq, and B. Dieny, Phys. Rev. B **75**, 014406 (2007).

24. W. S. Lew, S. P. Li, L. Lopez-Diaz, D. C. Hatton, and J. A. C. Bland, Phys. Rev. Lett. **90**, 2172011 (2003).

25. L. Thomas, J. Lüning, A. Scholl, F. Nolting, S. Anders, J. Stöhr, and S. S. P. Parkin, Phys. Rev. Lett. **84**, 3462 (2000).

26. C. L. Zha, J. Nogues, and J. Akerman, J. IEEE. Trans. Magn. **45**, 3881 (2009).

27.   A. Berger, D. T. Margulies, and H. Do, Appl. Phys. Lett. **85**, 1571 (2004).

28.   D. A. Garanin, Phys. Rev. B 55, 3050–3057 (1997).

29.   M. Hartl-Malang, J. Kotzler, and D. A. Garanin, Phys. Rev. B **51,** 8974 (1995).

30.   N. Kazantseva, D. Hinzke, U. Nowak, R. W. Chantrell, U. Atxitia, and O. Chubykalo-Fesenko, Phys. Rev. B **77**, 184428 (2008).

31.   R. F. L. Evans, D. Hinzke, U. Atxitia, U. Nowak, R. W. Chantrell, and O. Chubykalo-Fesenko, Phys. Rev. B **85**, 014433 (2012).

32.   A. D. Kent, U. Rudiger, J. Yu, L. Thomas, and S. S. P. Parkin, J. Appl. Phys. **85**, 5243 (1999).

33.   B. A. Gurney, M. Carey, C. Tsang, M. Williams, S. S. P. Parkin, R. E. Fontana, Jr., E. Grochowski, M. Pinarbasi, T. Lin, and D. Mauri, *Ultrathin Magnetic Structures IV*, edited by B. Heinrich and J. A. C. Bland (Springer, Berlin, 2005), Chapter 6 pg. 2.

CHAPTER 5

5 PERPENDICULAR MAGNETIC ANISOTROPY *L*1$_0$-FePt/TiN/*L*1$_0$-FePt PSVs

The growth of ordered *L*1$_0$-FePt involves a high temperature deposition process which will result in interlayer diffusion within the SV. Diffusion within the SV affects the magnetic, interfacial and spin transport properties which in turn adversely impacts the MR of the system [1]. A spacer with good diffusion barrier properties and/or the ability to lower the deposition temperature of the adjacent *L*1$_0$-FePt, while being able to sustain the differential scattering within the SV, is very much sought after. Spacer materials such as Ag, Au and Cu have been used in *L*1$_0$-FePt based SVs but these have been found to diffuse into the FM layer easily due to the high temperature deposition of *L*1$_0$-FePt [2, 3]. Recently, epitaxial growth of (001) textured *L*1$_0$-FePt layer on TiN underlayer has been reported [4, 5]. The lattice mismatch of 9.5 % between FePt and TiN imposes strain ordering on FePt, thereby promoting the ordered (001) epitaxial relationship. At the same time, the metallic TiN, with low resistivity of 15 μΩ cm, displays desirable qualities of being chemically stable towards FePt and is also a good diffusion barrier. In Chapter 5, the use of TiN as a spacer material in the *L*1$_0$-FePt based PSVs is investigated thorough experimental work and micromagnetic simulation.

5.1 Effects of TiN Spacer Thickness

The thickness of the spacer layer affects the interlayer interactions, such as the direct coupling through pinholes, indirect oscillatory RKKY coupling, Néel orange peel coupling and dipolar stray field coupling [6-11]. It also influences the extent of current shunting within the PSV. These factors are detrimental to the GMR. A detailed study of the influence of spacer layer thickness on the magnetization reversal and GMR behaviour is crucial for a deeper understanding of the $L1_0$-FePt/TiN/$L1_0$-FePt PSV. Section 5.1 focuses on the effects of varying TiN spacer thickness on the crystallographic, magnetic, reversal, interlayer coupling and magneto-transport properties of the $L1_0$-FePt PSV structures.

Samples with the structure $L1_0$-$Fe_{50}Pt_{50}$ (20 nm)/TiN (x nm)/$L1_0$-$Fe_{50}Pt_{50}$ (20 nm) were fabricated on single crystal (001)-textured MgO substrates, with x varied between 3 to 7 nm (Figure 5.1). These samples were prepared using the magnetron sputtering system with a base pressure better than 8×10^{-7} Torr. The bottom and top $L1_0$-FePt layers were deposited at 400 and 500 °C, respectively. The TiN spacer layer was deposited at 350 °C.

FePt	20 nm, 500 °C
TiN	x nm, 350 °C
FePt	20 nm, 400 °C
MgO substrate	
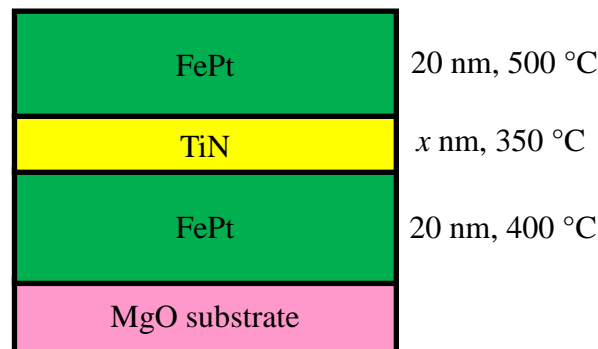
Figure 5.1   Schematic diagram of MgO/$L1_0$-FePt/TiN/$L1_0$-FePt PSV with varying spacer thickness.

5.1.1 Crystallographic and Microstructural Properties

The XRD spectrums of all the PSVs with different TiN spacer thickness show similar FePt (002) fundamental and FePt (001) superlattice peaks (Figure 5.2). Their integrated intensity ratios $I_{(001)}/I_{(002)}$ lie in the range of 0.68 to 0.79 [12]. The absence of the TiN (002) reflection in the XRD was attributed to the thin TiN spacer that was unable to produce a significant XRD signal beyond the noise level. In addition, TiN possessed a (002) Bragg angle that was close to that of MgO, resulting in its negligible signal being overshadowed by the strong MgO reflection.
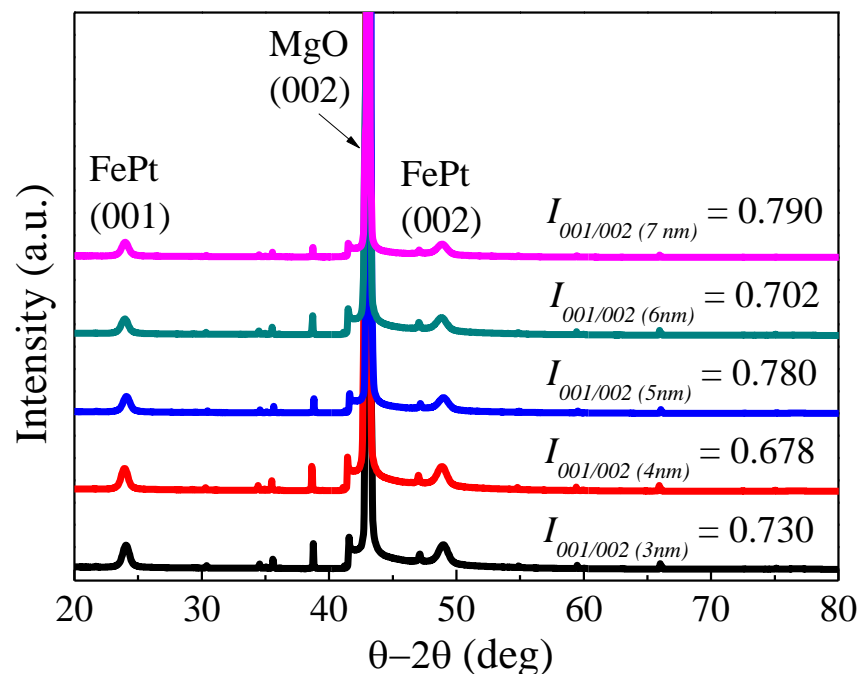
Figure 5.2   XRD spectrums of MgO/$L1_0$-FePt/TiN/$L1_0$-FePt PSVs with TiN spacer thickness of 3, 4, 5, 6 and 7 nm. The remaining unlabelled sharp peaks are inherent of the MgO substrate.

Figure 5.3(a) shows the cross-sectional SAED pattern along a <001> zone axis for the PSV with TiN spacer thickness of 5 nm. The (001) and (002) FePt spots were aligned with the strong (002) MgO spots. The cross-sectional HRTEM image in Figure 5.3(b) shows a highly contrasted TiN spacer and FePt layers due to the large difference in their atomic numbers. The observation of lattice fringes in the FePt

and TiN layers ascertained the growth of (001) textured FePt and (002) TiN crystalline films. A relatively clear and distinct FePt/TiN interface also suggested the presence of an effective TiN physical barrier which had minimal reaction with the adjacent FePt layers.
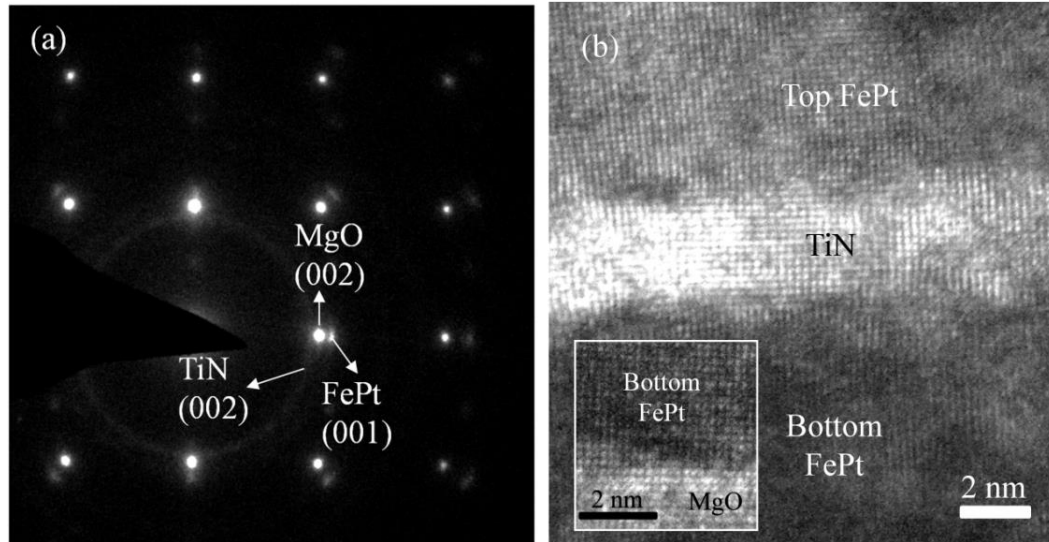
Figure 5.3   (a) Cross sectional SAED in the <001> zone axis. The faint ring pattern is the Pt (111) protective layer deposited on the PSV during FIB preparation. (b) Cross sectional HRTEM image for the MgO/$L1_0$-FePt/TiN/$L1_0$-FePt PSV with 5 nm TiN spacer. Inset shows the HRTEM image of bottom $L1_0$-FePt on MgO substrate.

5.1.2 Magnetic Properties

The magnetization hysteresis loop of a single layer of bottom $L1_0$-FePt deposited at 400 °C exhibits a coercivity of 1.8 kOe [Figure 5.4(a)]. In all of the PSVs, the top $L1_0$-FePt displayed a larger coercivity (H_c) due to a higher K_u which arose from the higher deposition temperature [Figures 5.4(b)-(f)]. The bottom $L1_0$-FePt behaved as the softer free layer while the top $L1_0$-FePt the harder fixed layer of the $L1_0$-FePt/TiN/$L1_0$-FePt PSVs. With increasing TiN spacer thickness, the PSVs became increasingly well-decoupled [Figures 5.4(b)-(f)], exhibiting a larger difference in the H_c between the top and bottom $L1_0$-FePt (Table 5.1).
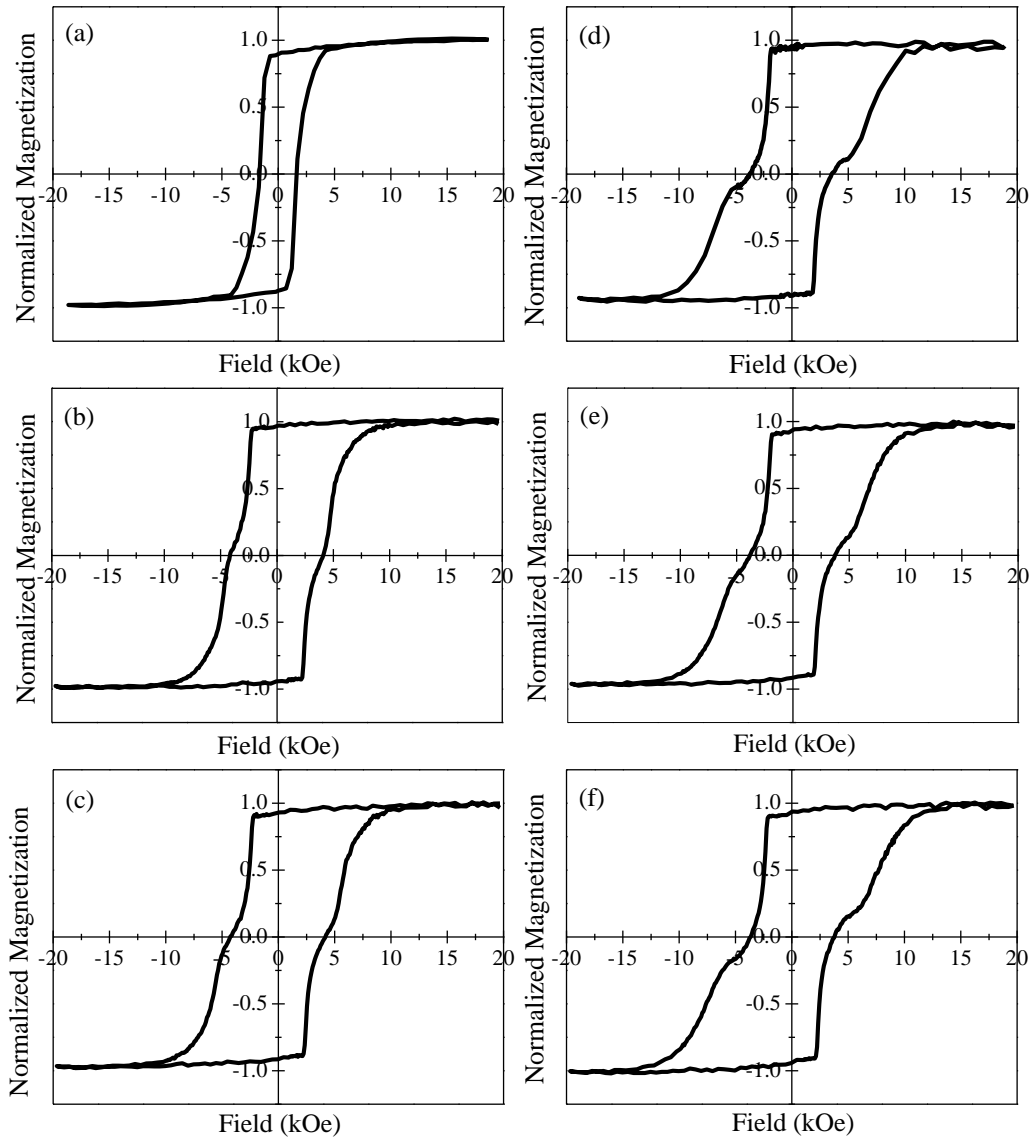
Figure 5.4   Out-of-plane hysteresis loops measured at room temperature for (a) MgO/$L1_0$-FePt and MgO/$L1_0$-FePt/TiN/$L1_0$-FePt PSVs with TiN spacer thickness of (b) 3, (c) 4, (d) 5, (e) 6 and (f) 7 nm.

Table 5.1   Summary of the properties of the MgO/$L1_0$-FePt/TiN/$L1_0$-FePt PSVs with TiN spacer thickness of 3, 4, 5, 6 and 7 nm.

TiN thickness (nm)	$H_{c(soft)}$ (kOe)	$H_{c(hard)}$ (kOe)	R_{RMS} (nm)	R_{max} (nm)	GMR (%)
3	2.60	5.14	0.27	6.44	0.53
4	2.57	5.98	0.28	5.58	0.78
5	2.30	7.55	0.30	4.46	0.61
6	2.28	7.52	0.26	3.75	0.59
7	2.44	8.23	0.29	4.82	0.52

This was attributed to a reduction in the interlayer coupling strength with a thicker spacer thickness. The interlayer coupling was largely contributed by the magnetostatic effects due to the magnetic dipoles set up within the $L1_0$-FePt layers. Lee *et al.* reported an exponential relationship between the magnetostatic coupling field (H_{stat}) and spacer thickness (t) [13]

$$H_{stat} = \frac{\pi^2 \gamma^2 M_P}{\sqrt{2}\lambda t_F} \exp\left(\frac{-2\pi\sqrt{2}t}{\lambda}\right) \tag{5.1}$$

where γ is the peak-to-peak waviness amplitude of the film, λ is the in-plane wavelength of the surface variations, M_p is the magnetization of the fixed layer and t_F is the thickness of the free layer. M_p did not vary significantly while t_F was kept constant across the PSVs with varying thickness. In addition, as seen in Table 5.1, the root mean square roughness (R_{RMS}) of the spacer did not vary significantly with thickness. With the same degree of roughness, a smaller TiN thickness resulted in a more significant contribution from the magnetostatic coupling, thus preventing the independent switching of the $L1_0$-FePt layers. Another minor contribution could presumably arise from the direct coupling due to pinholes. Pinhole defects can be thought of as localized regions where the roughness was greater than the thickness of the spacer, hence resulting in physical gaps which promoted direct interactions between the FMs. Pinhole defects were likely to be more prevalent in a thinner TiN spacer, thereby creating a stronger direct interlayer coupling. This is substantiated with the maximum roughness (R_{max}) values in Table 5.1, in which these values generally increased with decreasing spacer thickness. In particular, for TiN spacer thickness of 3 and 4 nm, the maximum roughness was larger than the spacer thickness, thus suggesting the possible presence of pinhole defects. The oscillatory RKKY coupling favours ferromagnetic or anti-ferromagnetic coupling depending

on the thickness of the spacer [14, 15]. The presence of this oscillatory coupling could not be determined in this range of TiN spacer thickness studied. The RKKY coupling is understood to have originated from the quantum interference of electrons confined within the non-magnetic spacer. Thus, its strength is typically dominant at spacer thickness of several monolayers. With increasing spacer thickness to a length scale of several nanometers (> 3 nm), the RKKY coupling strength diminishes drastically. As such, contribution to the interlayer coupling by RKKY was assumed to be negligible in the PSVs in this work.

5.1.3 Reversal Mechanism

The reversal mechanism of both top and bottom $L1_0$-FePt layers in the PSV with TiN spacer thickness of 5 nm is shown in Figure 5.5. The remanent magnetic configurations of both $L1_0$-FePt layers were studied at the intermediate stages of their reversal process. A +20 kOe field was first applied to fully saturate the sample. Subsequently, a field between 0 to -12 kOe was applied. MFM images were then taken at zero field to study the remanent magnetic configurations of the layers at different magnetization stages along the first half of the hysteresis loop. Figures 5.5(b)-(d) capture the remanent magnetic configurations of the soft bottom $L1_0$-FePt during its various reversal stages. At a field of -6 kOe, complete reversal of the soft bottom $L1_0$-FePt was expected. Figures 5.5(e)-(h) depict the remanent magnetic configurations of the hard top $L1_0$-FePt at its various reversal stages. The reversal in both $L1_0$-FePt layers proceeded by reversed domain nucleation and propagation. Their initial reversals were marked by bright white regions, where distinct regions of spin up and spin down configurations were present. As the reversal proceeded to complete saturation in either $L1_0$-FePt layer, the intensity of the reversed domains changed from bright white to a darker yellow as the

difference in magnetization between the neighbouring domains became less distinct.
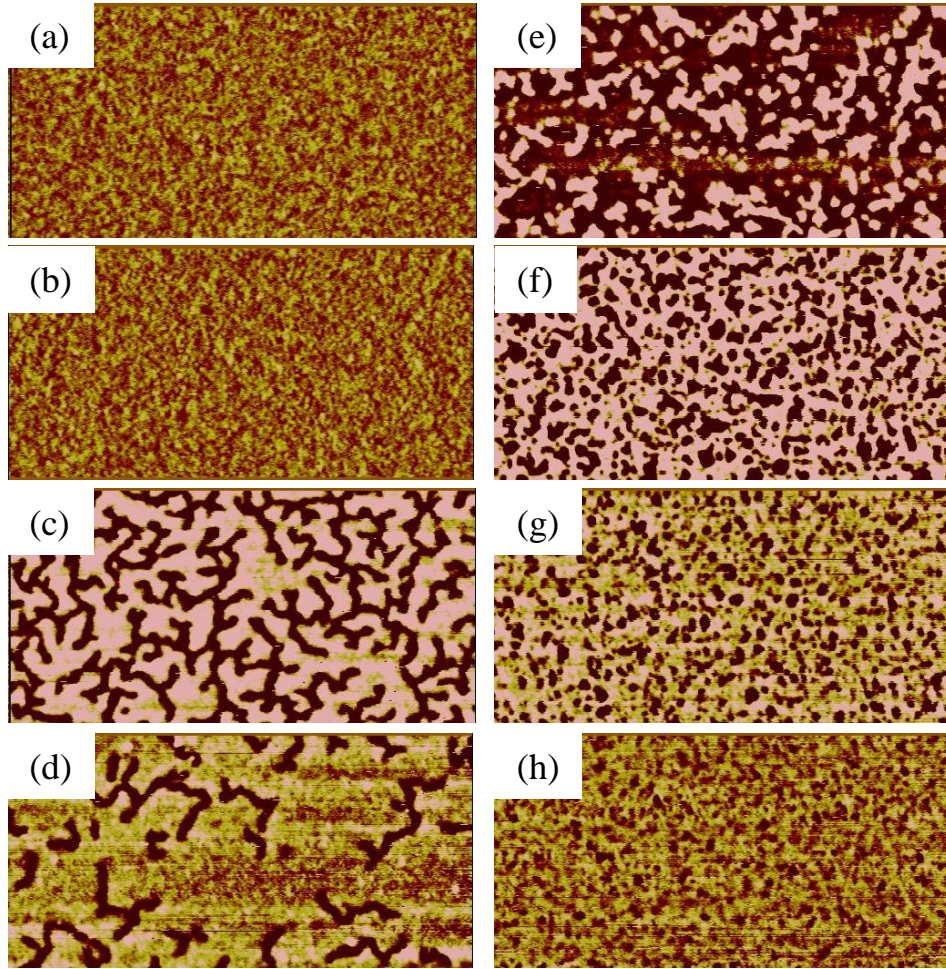
Figure 5.5 10×5 μm^2 MFM images showing the magnetization states of the $L1_0$-FePt layers in the PSVs with applied field of (a) 0, (b) -2, (c) -3, (d) -4, (e) -6, (f) -8, (g) -10 and (h) -12 kOe. Brighter regions are reversed domains with spin up configuration.

The reversed domains in the hard top $L1_0$-FePt appeared to be smaller than the soft bottom $L1_0$-FePt. The domain wall width (δ) is related to the K_u by Equation (5.2)

$$\delta = \pi\sqrt{A/K_u} \tag{5.2}$$

where exchange constant $A = 10^{-6}$ erg/cm [16]. The higher K_u of the top $L1_0$-FePt gave rise to a smaller domain wall width. For a domain wall with smaller wall width, a larger volume fraction of the domain wall would be pinned by defects. As

such, it was likely that the magnetic domains of the hard top $L1_0$-FePt experienced more efficient pinning by defects compared to the soft bottom $L1_0$-FePt, thus leading to smaller domain sizes.

5.1.4 Interlayer Coupling within PSV

The influence of the interlayer coupling on the reversal of the $L1_0$-FePt layers was demonstrated through the shift in the center of the minor hysteresis loops for the PSVs with TiN thickness of 5 and 7 nm. A +20 kOe field was applied to fully saturate both $L1_0$-FePt layers in the same spin down direction. A field in the range of 0 to -20 kOe was then applied to attain different magnetization states of the hard top $L1_0$-FePt. A minor loop below the switching field of the hard magnetic layer, between +5 to -5 kOe, was then cycled. The difference between the H_c in the first and second quadrants of the minor loop was termed the interlayer coupling field H_{int}.

At an applied field of 0 [Figure 5.6(a)] and -20 kOe [Figure 5.6(d)] where the hard top $L1_0$-FePt was fully saturated, the shift observed in the minor loop suggested the presence of magnetostatic coupling between the hard and soft $L1_0$-FePt layers. At an applied field of 0 kOe, the hard top $L1_0$-FePt was fully saturated in the spin down configuration. When the minor loop was cycled from +5 to -5 kOe, the soft bottom $L1_0$-FePt had to overcome the interlayer interactions from the hard top $L1_0$-FePt to attain an anti-parallel configuration [inset of Figure 5.6(a)]. This resulted in the shift in H_{int} in the negative direction. Conversely, a positive H_{int} was observed at an applied field of -20 kOe, where the soft bottom $L1_0$-FePt reversed more easily to the same parallel configuration as the hard top $L1_0$-FePt with the assistance of the interlayer interactions [inset of Figure 5.6(d)].
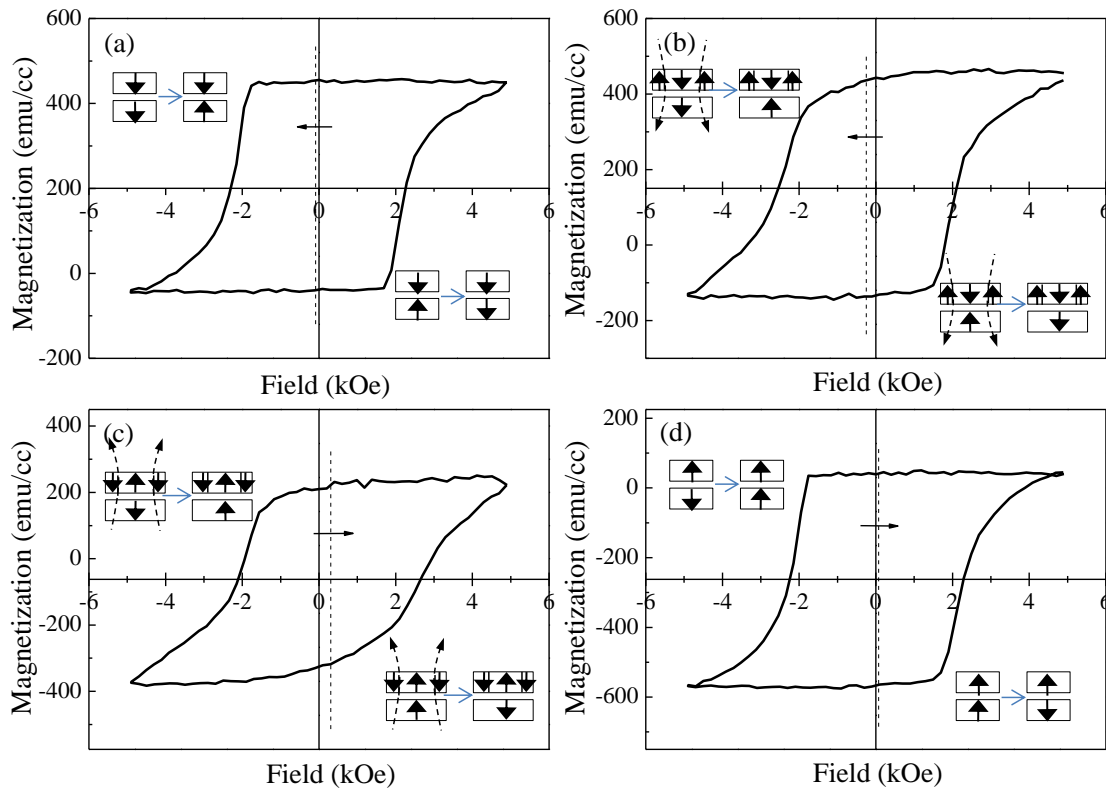
Figure 5.6   Minor hysteresis loops of the PSV with TiN thickness of 5 nm measured under the influence of the different magnetization states of the top $L1_0$-FePt, created through applied fields of (a) 0, (b) -6, (c) -8 and (d) -20 kOe. The dotted line indicates the centre of the minor hysteresis loop; the arrow indicates the direction of the shift of the minor hysteresis loop. Insets indicate schematically the influence of bottom $L1_0$-FePt on the reversal of top $L1_0$-FePt.

There was a decrease followed by a positive peak in H_{int} in the range of applied field between -6 to -10 kOe [Figure 5.6(b) and (c)]. Figures 5.5(e)-(g) discussed earlier in Section 5.1.3 show that partially reversed states of the hard top $L1_0$-FePt were present in this applied field range. As such, apart from the magnetostatic effect, dipolar stray field due to the non-uniformly magnetized hard top $L1_0$-FePt film also played a major role in influencing the H_{int} [17, 18]. The direction and strength of the stray field depended on the density of reversed domains present in the hard top $L1_0$-FePt. At an applied field of -6 kOe, reversed domains with spin up configuration began to nucleate but the density of unreversed domains with spin down configuration remained larger in the hard top $L1_0$-FePt [Figure 5.5(e)]. This

116

resulted in a larger extent of dipolar coupling stray field emanating from the walls of the unreversed domains, which impeded the propagation of the reversed domains in the soft bottom $L1_0$-FePt when the minor loop was swept from +5 to -5 kOe [inset of Figure 5.6(b)]. Thus, a decrease in H_{int} was observed at an applied field of -6 kOe. However, with an increased applied field of -8 kOe, the proportion of reversed domains with spin up configuration surpassed that of the unreversed domains in the hard top $L1_0$-FePt [Figure 5.5(f)]. A positive peak in H_{int} occurred as a result of the fringing fields from the walls of the high density reversed domains, which reduced the local nucleation field and promoted propagation of reversed domains in the adjacent soft bottom $L1_0$-FePt, when the minor loop was swept from +5 to -5 kOe [inset of Figure 5.6(c)]. With increasing negative applied field, the increasingly saturated hard top $L1_0$-FePt generated fewer stray fields and the effects of dipolar coupling gradually diminished.

The H_{int} values obtained from the minor loops of the PSV with TiN thickness of 5 and 7 nm are shown in Figure 5.7. The minor loops of the PSV with TiN thickness smaller than 5 nm were not compared here as fully saturated minor loops were unobtainable. A sufficiently large field range to saturate the minor loop could not be achieved in these poorly decoupled PSVs without capturing the magnetization loop of the hard top $L1_0$-FePt. With a thicker TiN spacer, the reduced interlayer coupling strength between the $L1_0$-FePt layers was reflected with H_{int} values which were closer to zero, indicating a greater extent of independent reversal of the soft bottom $L1_0$-FePt.
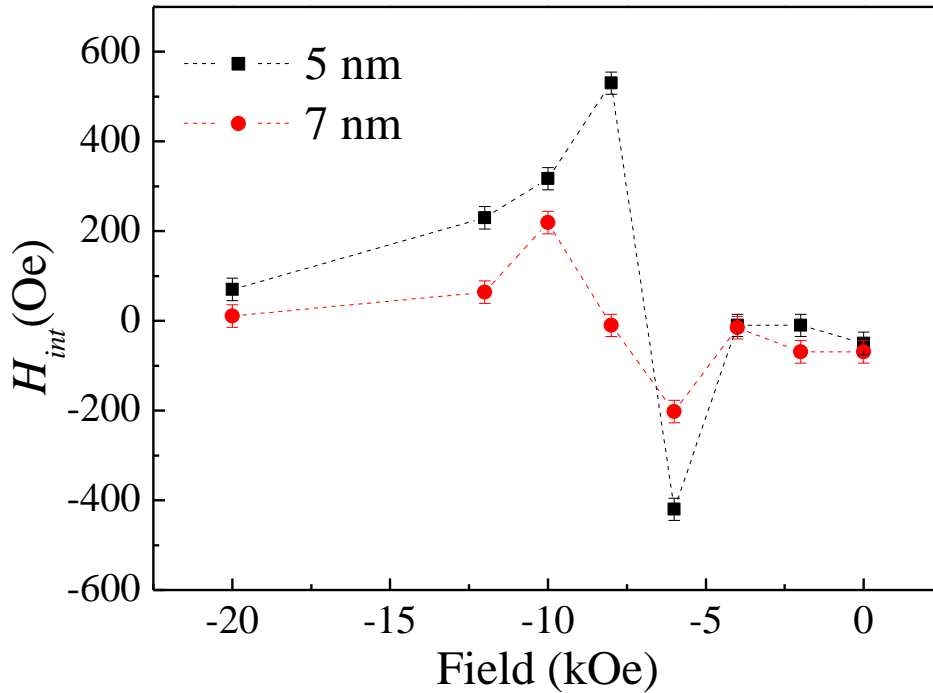
Figure 5.7   Interlayer coupling field H_{int} of the minor hysteresis loop versus applied field for the PSVs with TiN spacer thickness of 5 and 7 nm. Dashed lines serve as a guide for the eye. The vertical error bar represents the systematic instrumental error due to the finite step size of the minor loop.

5.1.5 Current-in-Plane GMR

A single layer of bottom $L1_0$-FePt shows a linear behaviour of resistivity with magnetic field, displaying a MR of 0.41 % [Figure 5.8(a)]. At finite temperatures, the directions of the localized d electrons spins fluctuated and the s electrons coupled to them scattered from their inhomogeneous exchange potential [19, 20]. This spin flip scattering contributed to the resistivity of the $L1_0$-FePt film. The linear decrease in resistivity occurred with increasing applied field which acted to suppress the spin disorder scattering. In addition, the spike followed by sharp drop in resistivity at the coercive field of the $L1_0$-FePt film was contributed by magnon magnetoresistance (MMR) [21]. At an applied field slightly smaller than the coercive field, the applied field acted in an opposite direction from the magnetization direction. The destabilization of the magnetization direction led to a

118

surge in magnon population, thus bringing about an upsurge in MMR. The magnon population decreased sharply when the applied field and magnetization direction acted in the same direction at the coercive field. Consequently, a reduction in MMR was observed.
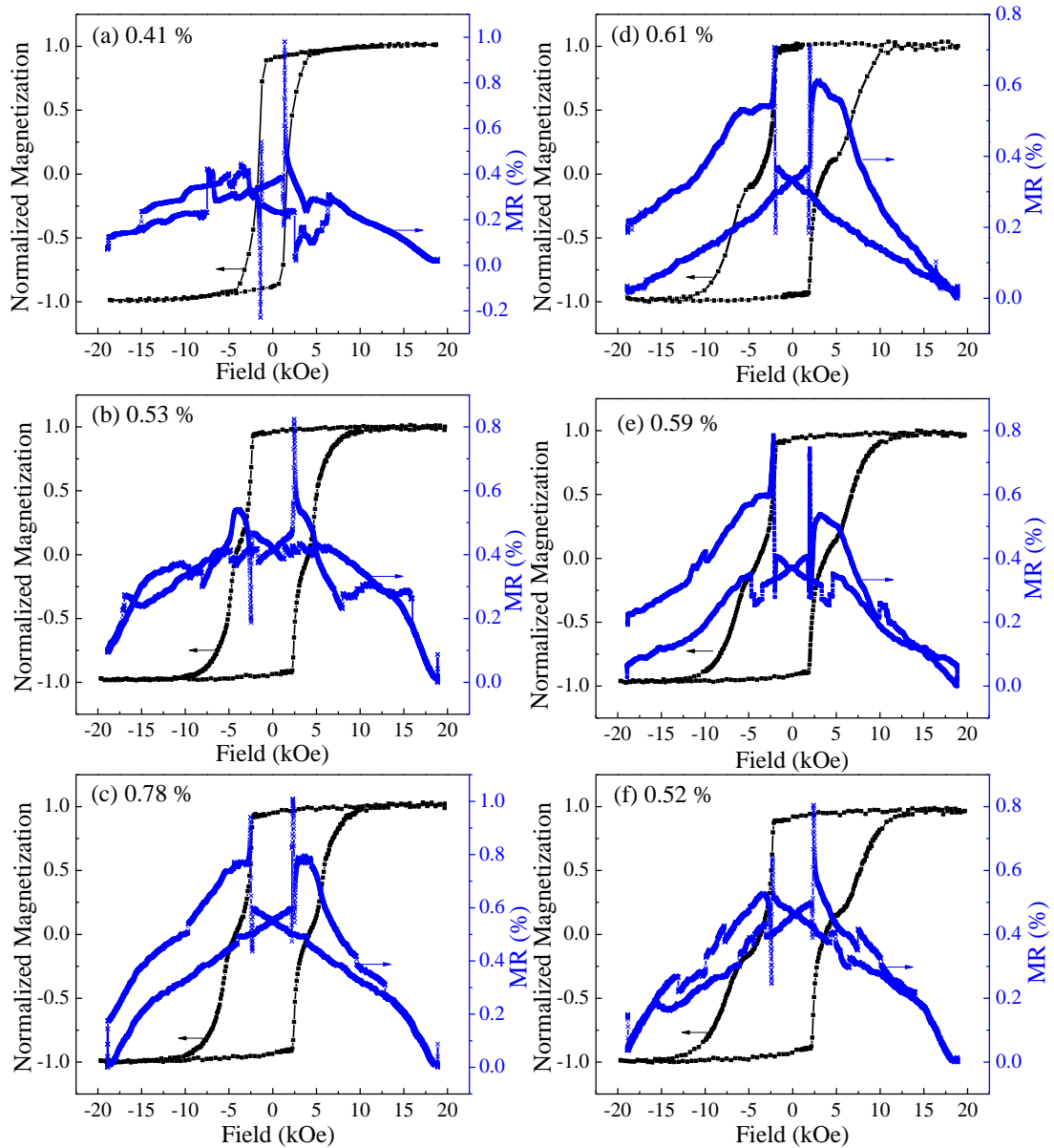
Figure 5.8   Out-of-plane magnetization (■) and MR (x) curves measured at room temperature for (a) MgO/*L*1₀-FePt, MgO/*L*1₀-FePt/TiN/*L*1₀-FePt PSVs with TiN spacer thickness of (b) 3, (c) 4, (d) 5, (e) 6 and (f) 7 nm.

Similar contributions by spin disorder and MMR were observed in the MR loops of the PSVs with different TiN thickness [Figures 5.8(b)-(f)]. However, the effects of MMR were not prominent at the coercivity of the hard top *L*1₀-FePt, compared to

the soft bottom $L1_0$-FePt, due to its larger SFD. At an applied field slightly smaller than the coercive field of the hard top $L1_0$-FePt, a considerable number of spins had already reversed and the remaining spins which could contribute to the MMR effect was significantly reduced. The electron mean free path for TiN is in the range of 39 to 41 nm, which is large enough for the electrons to pass through all the layers successfully when the current flows in the plane of the layers [22]. As such, in addition to the spin disorder and MMR contributions, resistivity due to the spin dependent scattering of the conduction electrons at the trilayer interfaces was also present.

With increasing TiN spacer thickness, the GMR increased to a maximum and then decreased with further increase in TiN thickness (Figure 5.9). The initial increase in GMR with an increase in TiN thickness was the result of a reduction in the short-range interlayer magnetostatic interactions. This permitted a difference in the coercivity between the top and bottom $L1_0$-FePt as well as an increase in the effectively decoupled regions, increasing the sample area over which a high resistance anti-parallel configuration of the PSV may be realized. However, with a further increase in TiN thickness, the GMR gradually declined despite a more effectively decoupled PSV and a further reduction of the interlayer coupling strength. Further increasing the spacer thickness increased the probability of conduction electrons being channelled away from the $L1_0$-FePt/TiN interface and confined within the TiN spacer. Due to this current shunting effect, the GMR eventually diminished at larger TiN spacer thickness.
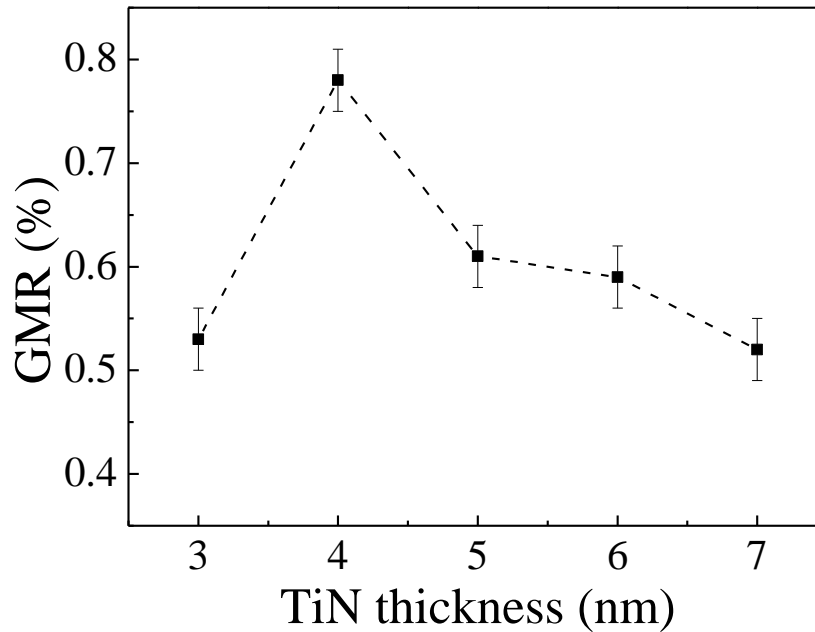
Figure 5.9   GMR ratio of MgO/*L*1₀-FePt/TiN/*L*1₀-FePt PSVs with respect to the different TiN spacer thickness. Dashed line serves as a guide for the eye. The error bar indicates the standard deviation of 3 independent measurements.

5.2 Effects of Top *L*1₀-FePt Thickness

The morphology of $L1_0$-FePt on TiN is known to be affected by its thickness and this poses significant changes to the resistance, magnetic and spin-transport properties of the PSVs [5]. In this section, the magnetic and spin transport properties of $L1_0$-FePt/TiN/$L1_0$-FePt PSV with varying top $L1_0$-FePt thickness are investigated. Samples with the structure MgO (001) substrate/$L1_0$-$Fe_{50}Pt_{50}$ (20 nm)/TiN (5 nm)/$L1_0$-$Fe_{50}Pt_{50}$ (y nm) were prepared, with y varied between 5 to 20 nm (Figure 5.10). Deposition conditions of these PSVs were the same as those fabricated in Section 5.1. These samples were prepared using the magnetron sputtering system with a base pressure better than 8×10^{-7} Torr. The bottom and top $L1_0$-FePt layers were deposited at 400 and 500 °C, respectively. The TiN spacer layer was deposited at 350 °C.
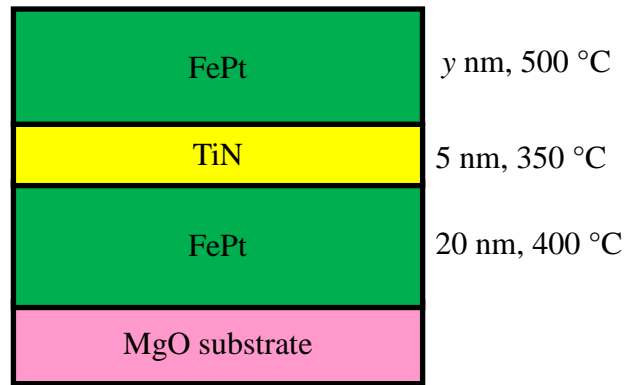
Figure 5.10 Schematic diagram of MgO/$L1_0$-FePt/TiN/$L1_0$-FePt PSV with varying top $L1_0$-FePt thickness.

The XRD spectrums in Figure 5.11 show the presence of the FePt (002) fundamental peak and the FePt (001) superlattice peak in all the PSVs. The chemical ordering parameter (S) resided in a high range of 0.7 to 0.8, indicating the strong presence of (001) $L1_0$ texture in these PSVs [23]. No TiN (002) peak was detected as the thin TiN spacer gave rise to a low signal to noise ratio.
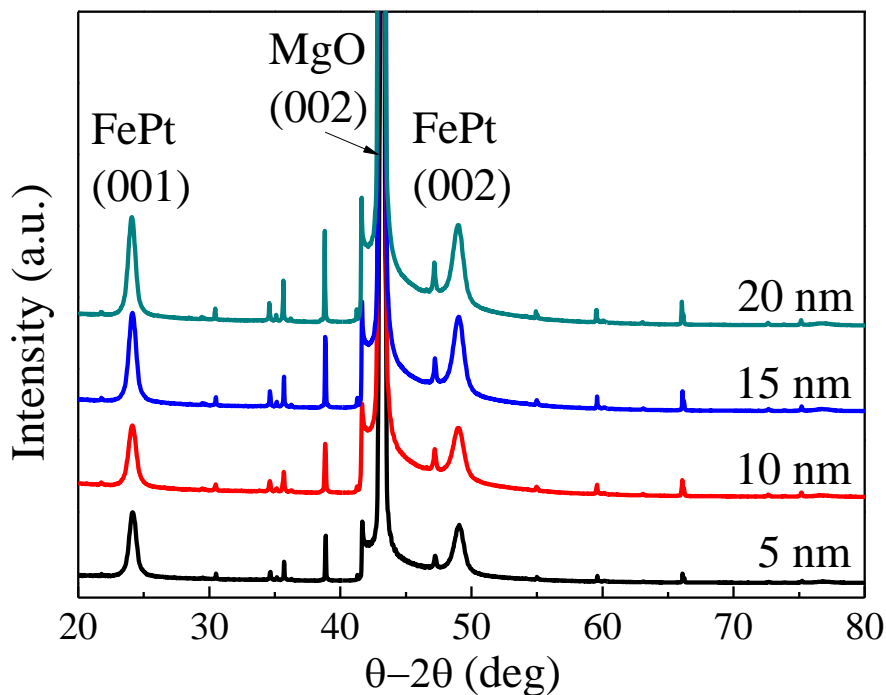
Figure 5.11 XRD spectrums of MgO/$L1_0$-FePt/TiN/$L1_0$-FePt PSVs with different top $L1_0$-FePt thickness of 5, 10, 15, and 20 nm. The remaining unlabelled sharp peaks are inherent of the MgO substrate.

Figures 5.12 and 5.13 show the hysteresis loops and SFD curves of the PSVs, respectively. The difference in coercivity between the top and bottom *L1*$_0$-FePt as well as the SFD of the top *L1*$_0$-FePt diminished with increasing thickness of top *L1*$_0$-FePt are summarized in Table 5.2.
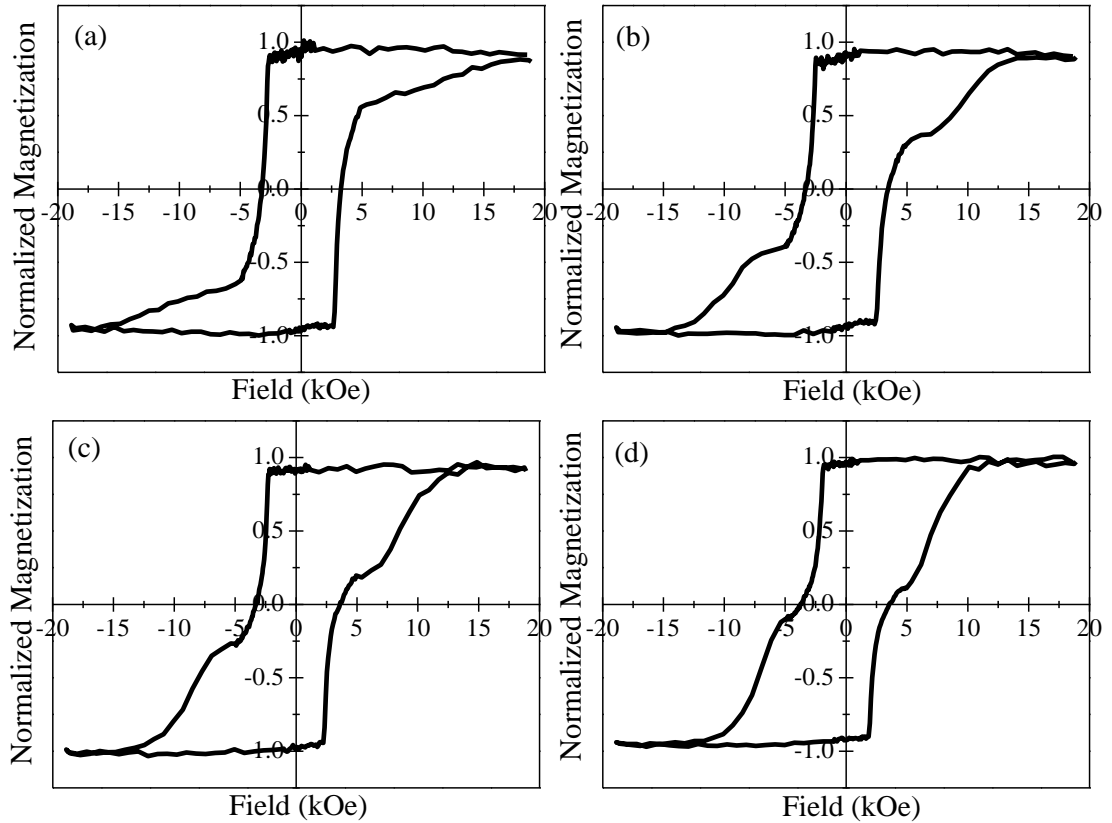
Figure 5.12 Out-of-plane hysteresis loops measured at room temperature for MgO/*L1*$_0$-FePt/TiN/*L1*$_0$-FePt PSVs with top *L1*$_0$-FePt thickness of (a) 5, (b) 10, (c) 15 and (d) 20 nm.
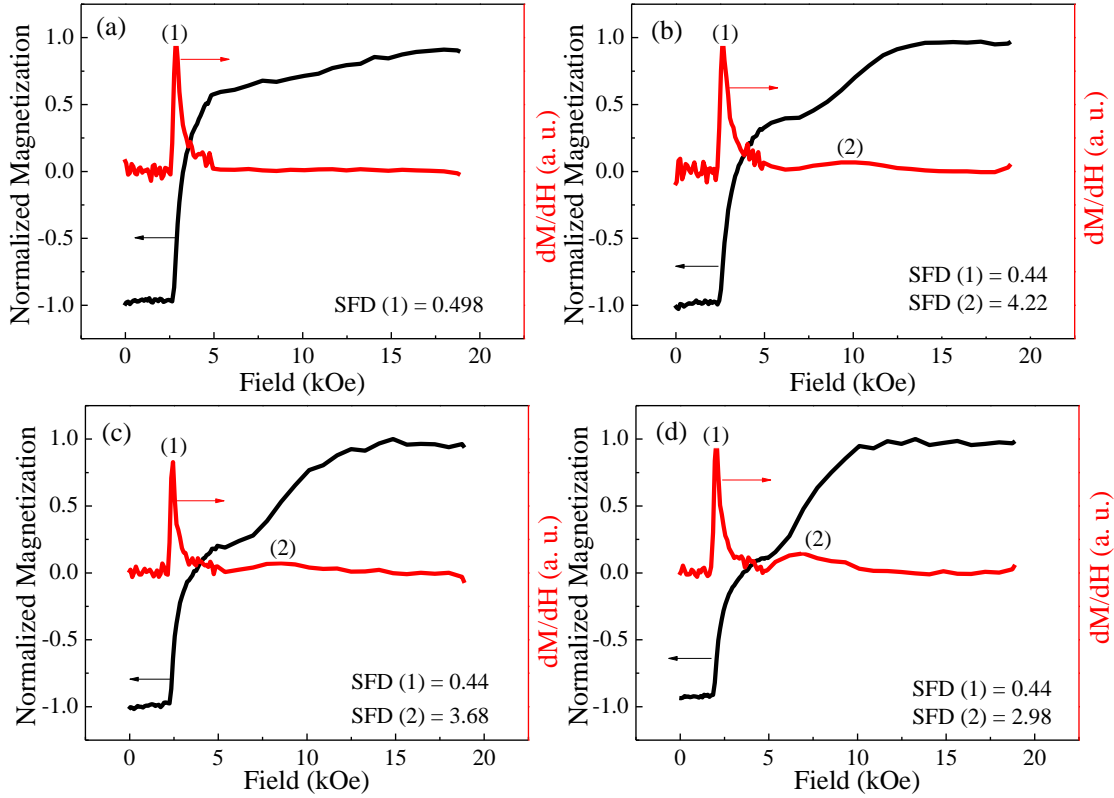
Figure 5.13 Partial hysteresis loops and the derivatives of the partial hysteresis loops, with bottom and top $L1_0$-FePt layer labelled (1) and (2), respectively, for PSVs with top $L1_0$-FePt thickness of (a) 5, (b) 10, (c) 15 and (d) 20 nm.

Table 5.2   Summary of the properties of the MgO/$L1_0$-FePt/TiN/$L1_0$-FePt PSVs with top $L1_0$-FePt thickness of 5, 10, 15 and 20 nm.

Top $L1_0$-FePt Thickness (nm)	$H_{c(hard)}$ (kOe)	$H_{c(soft)}$ (kOe)	$SFD_{(hard)}$ (kOe)	$SFD_{(soft)}$ (kOe)	Resistance (Ω)	GMR (%)
5	/	3.3	/	0.49	9.22	/
10	10.1	2.9	4.22	0.44	8.18	0.35
15	8.5	2.6	3.68	0.44	6.62	0.51
20	7.6	2.3	2.98	0.44	5.44	0.61

With increasing top $L1_0$-FePt thickness, the $L1_0$-FePt film morphology changed from a particulate island growth to a more complete continuous 3D growth (Figures 5.14 and 5.15), resulting in a decrease in its coercivity. Consequently, the difference in coercivity between the top and bottom $L1_0$-FePt reduced. In addition,

the increased exchange coupling within the more continuous thicker $L1_0$-FePt film also gave rise to a narrower SFD for the top $L1_0$-FePt. Conversely, for the top $L1_0$-FePt with a thickness of 5 nm, the magnetic moments of the $L1_0$-FePt island-growth grains did not reverse concurrently, contributing to a large SFD [Figure 5.12(a)]. Furthermore, a reduction in the resistance of the PSV with increasing thickness of the top $L1_0$-FePt (Table 5.2) was the consequence of a thicker and more continuous percolation path of the top $L1_0$-FePt layer for the conduction electrons, which had to pass through the plane of the film during the CIP measurement.
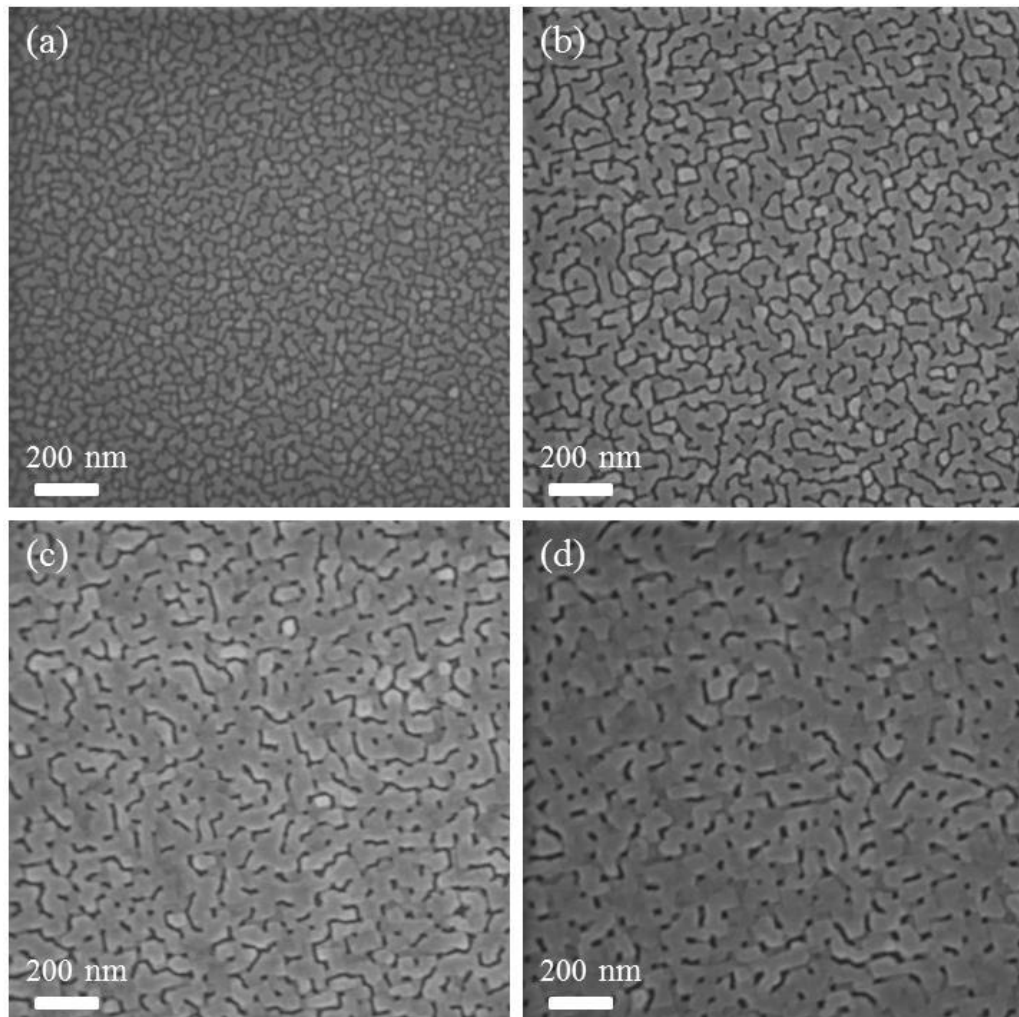
Figure 5.14 Plan-view SEM images of the top $L1_0$-FePt with thickness of (a) 5, (b) 10, (c) 15 and (d) 20 nm for the MgO/$L1_0$-FePt/TiN/$L1_0$-FePt PSVs.
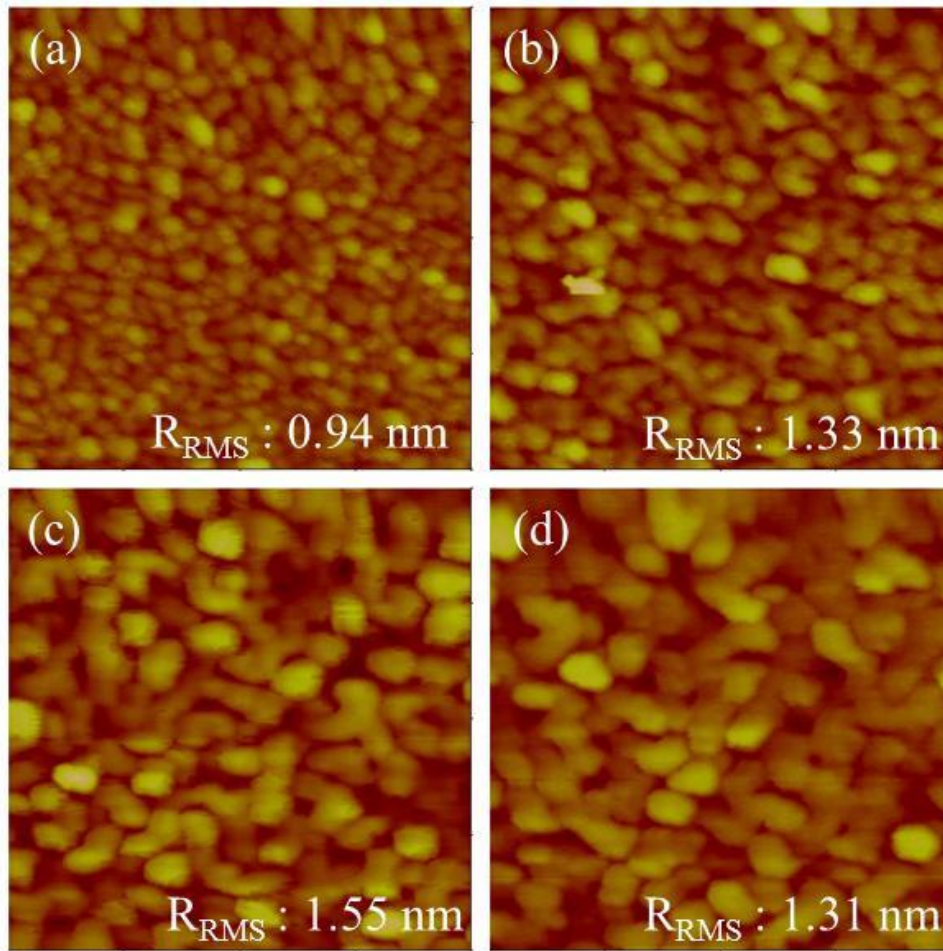
Figure 5.15 1×1 μm^2 AFM images of the top $L1_0$-FePt with thickness of (a) 5, (b) 10, (c) 15 and (d) 20 nm for the MgO/$L1_0$-FePt/TiN/$L1_0$-FePt PSVs.

The GMR of the PSVs decreased with a thinner top $L1_0$-FePt, and eventually disappeared with a top $L1_0$-FePt thickness of 5 nm (Figure 5.16). The island growth of the top $L1_0$-FePt prevented a continuous pathway for the spin dependent scattered electrons to be detected via the CIP measurement.
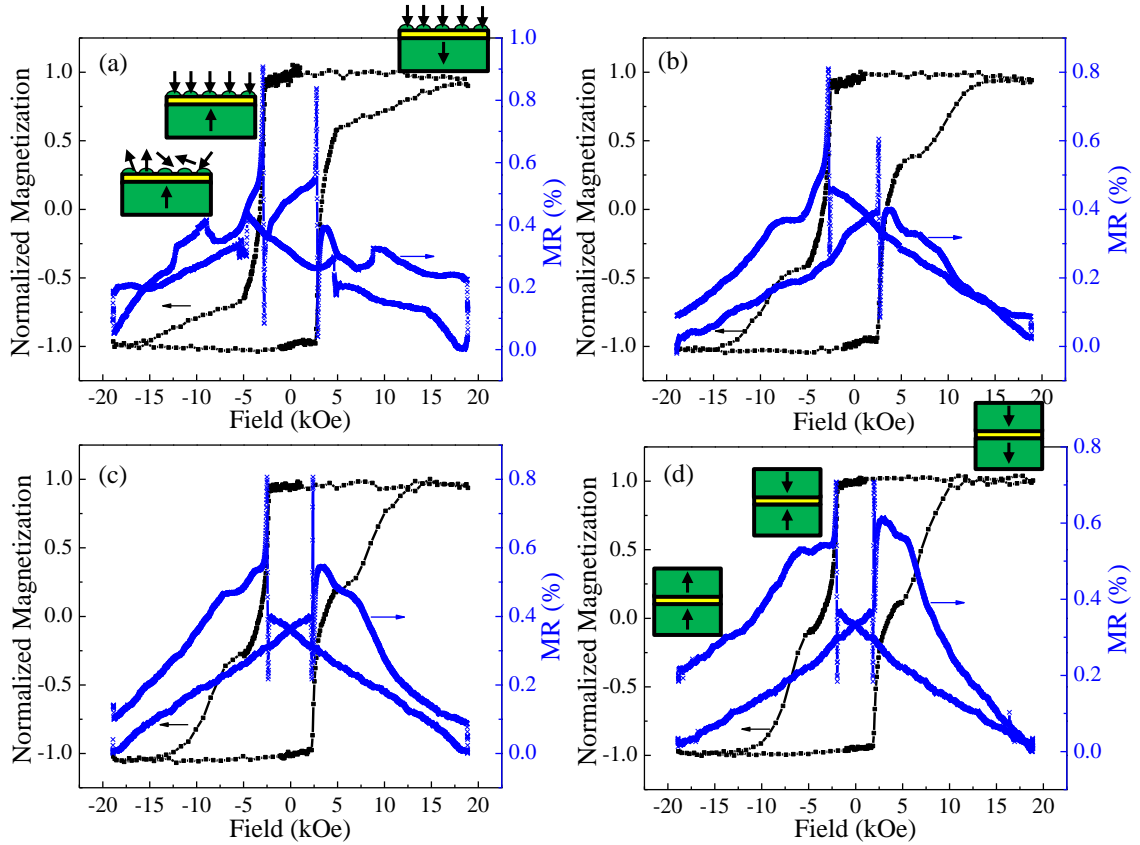
Figure 5.16 Out-of-plane magnetization (■) and MR (x) curves measured at room temperature for MgO/*L*1$_0$-FePt/TiN/*L*1$_0$-FePt PSVs with top *L*1$_0$-FePt thickness of (a) 5, (b) 10, (c) 15 and (d) 20 nm.

5.3 Evaluation and Comparison of GMR of *L*1$_0$-FePt PSVs with Different Spacers

The GMR observed with the TiN spacer was smaller than with the use of the Ag spacer (1.1 %) in similar (001) textured *L*1$_0$-FePt based PSVs shown in the Chapter 4. Based on the resistor model for CIP GMR illustrated in Equation (5.3), the MR ratio of a multilayer with spacer layer of finite resistance is given by: [24]

$$\frac{\Delta R}{R} = \frac{(\alpha - 1)^2}{4\left(\alpha + \frac{\rho d_{NM}}{d_{FM}}\right)\left(1 + \frac{\rho d_{NM}}{d_{FM}}\right)}$$

(5.3)

127

where α is the scattering spin asymmetry, d_{NM} is the thickness of the non-magnetic spacer and d_{FM} is the thickness of the ferromagnet. ρ is the resistivity defined by $\rho_{NM}/\rho_\uparrow$, where ρ_{NM} is the resistivity of the non-magnetic spacer and $\rho_\uparrow$ is the majority spin resistivity. It should be noted that this is a largely simplified resistor model that is only applicable for spacer thickness d_{NM} smaller than its electron mean free path. Assuming that the PSVs with various spacer materials possessed the same structure with the same d_{NM} and d_{FM}, the CIP GMR of the PSV would then be largely dependent on the scattering spin asymmetry and resistivity of the spacer. Thus, the smaller GMR in the $L1_0$-FePt/TiN/$L1_0$-FePt PSV was possibly due to the larger resistivity of TiN (15 $\mu\Omega$ cm) compared to Ag (1.6 $\mu\Omega$ cm) [25], which led to a greater extent of spin independent scattering.

Another possible reason is the smaller scattering spin asymmetry of TiN with FePt compared to Ag with FePt. First principles calculations of the band structures of FePt, TiN and Ag were performed with CASTEP, using the density functional theory and plane-wave pseudopotential method. The lattice constant of Ag and TiN were assigned to be the same as that of FePt in the calculations, based on the assumption that there existed epitaxial growth of Ag and TiN on FePt layer. Near the Fermi energy level of 0 eV, the energy band structures of TiN and Ag displayed better band structure matching with the FePt spin up electrons [Figures 5.17(a) and 5.17(c)] compared to the FePt spin down electrons [Figures 5.17(b) and 5.17(d)] [26]. This indicates a higher transmission of the majority spin up electrons and a poorer transmission of minority spin down electrons at both the FePt/TiN and FePt/Ag interfaces. The scattering spin asymmetry is the difference in the conductivities (σ) of these two spin channels, where $\alpha = \sigma_\uparrow/\sigma_\downarrow$. When the $L1_0$-FePt layers were aligned, the majority spin up electrons passed through relatively easily,

giving a low resistance state. A higher resistance state was produced when the $L1_0$-FePt layers were anti-aligned and electrons in both channels were reflected at either one of the interfaces. As such, to attain a larger GMR, a larger spin scattering asymmetry is desirable. The band structures of Ag with FePt spin up electrons [Figure 5.17(c)] displayed better band compatibility, with larger regions of similar energy and slope, compared to that of TiN with FePt spin up electrons [Figure 5.17(a)]. This suggests the presence of a larger density of states available for the majority spin up electrons at the FePt/Ag interface compared to that of FePt/TiN. The lower GMR observed in the $L1_0$-FePt PSV with TiN spacer could thus be a result of its smaller interfacial scattering spin asymmetry.
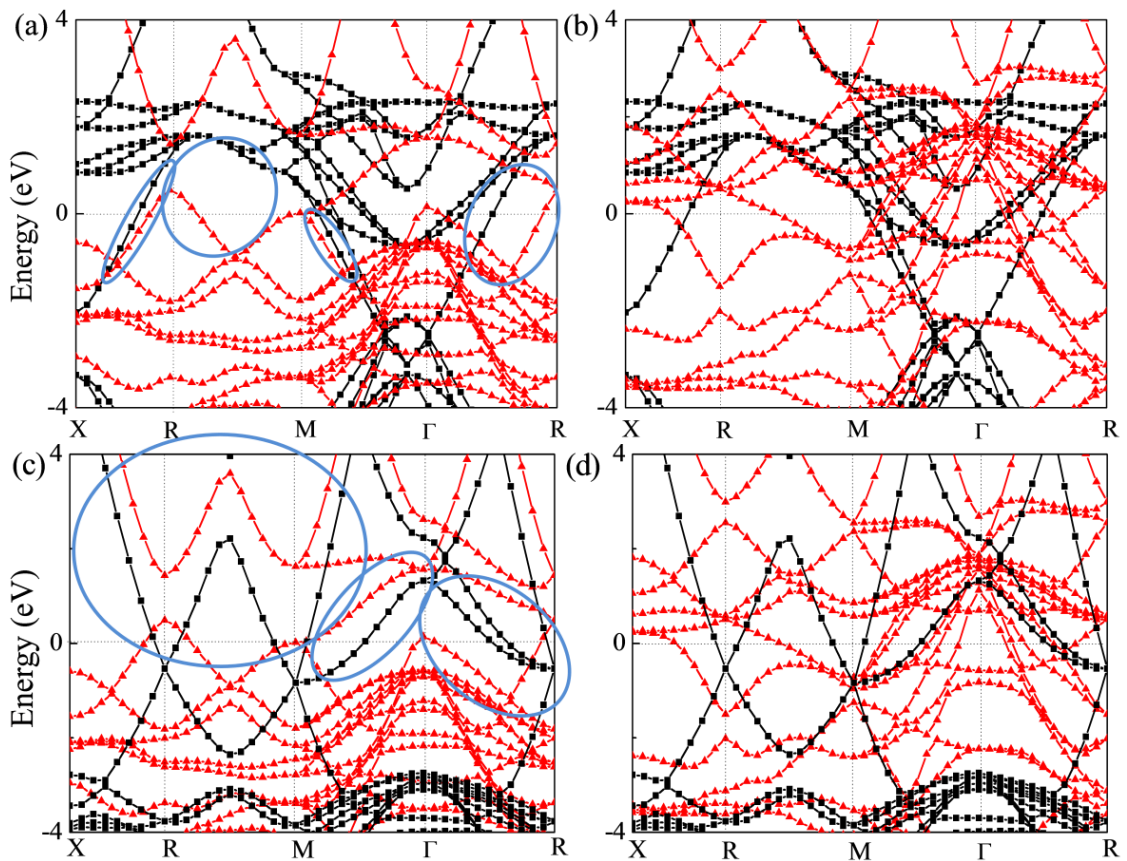
Figure 5.17 Energy bands for (a) TiN (■) with spin up FePt (▲), (b) TiN (■) with spin down FePt (▲), (c) Ag (■) with spin up FePt (▲) and (d) Ag (■) with spin down FePt (▲).

129

5.4 Micromagnetic Simulation with Trilayer Model

In Sections 4.2 and 4.3, the atomistic modelling and bilayer micromagnetic modelling were introduced to study the $L1_0$-FePt based PSVs. The atomistic study involved a single grain model which did not take into consideration the inter-grain exchange coupling and magnetostatic coupling present in the granular $L1_0$-FePt films. While a more complete description of the spin valve was made with the bilayer micromagnetic multiple granular approach, this model was a dual layer ferromagnetic system which did not explicitly include the presence of a spacer. In this section, the magnetic and magnetoresistive properties of a trilayer $L1_0$-FePt/TiN/$L1_0$-FePt PSV is modelled theoretically using a trilayer micromagnetic model (Figure 5.18). The trilayer micromagnetic model is an extension of the bilayer micromagnetic model described in Section 4.3, in which an additional spacer layer is introduced with the insertion of a physical space between the two FePt layers. The spacer thickness is represented by the magnitude of the gap between the two FePt layers.
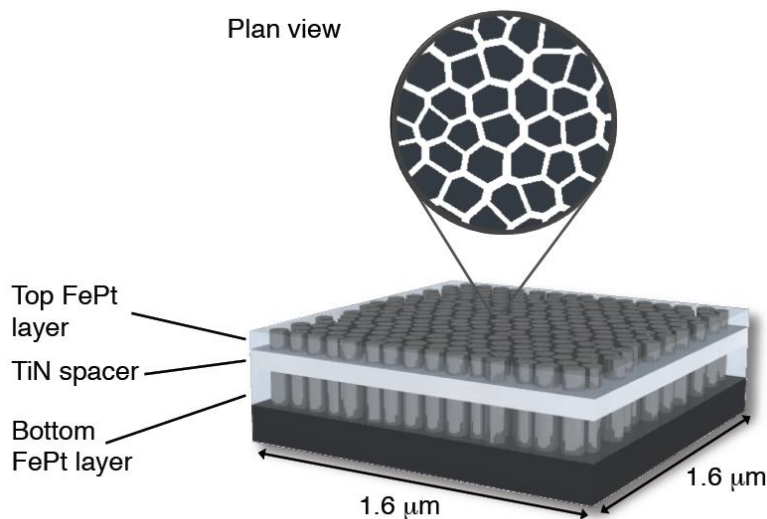
Figure 5.18 Schematic illustration of the trilayer model adopted in the micromagnetic simulation.

The effects of the hard top $L1_0$-FePt layer thickness on the magnetic properties of the PSVs were investigated. Changing the FePt layer thickness principally affected two key phenomena: the change in morphology which led to highly exchange coupled magnetic grains and an increased influence of the demagnetizing field.

The changes in morphology of the top $L1_0$-FePt layer for different layer thickness are shown in the SEM images in Figure 5.14. Increasing the top $L1_0$-FePt layer thickness changed the granular nature of the film to a more complete continuous 3D growth, due to the agglomeration of the grains. This suggested that a greater proportion of the grains in the top layer were exchange coupled with increased film thickness. Thus, the fraction of intralayer decoupled grains f_{intra} for the top $L1_0$-FePt is expected to diminish with increasing top $L1_0$-FePt thickness.

In addition, each isolated grain, which contained a single domain, is expected to emit magnetic stray fields at its walls. In the trilayer with a thinner top $L1_0$-FePt marked by particulate grain growth, there existed a greater extent of magnetic stray fields emanating from the higher density individual domain walls. On the other hand, these magnetic stray fields diminished for a thicker and more continuous top $L1_0$-FePt layer with a reduction in the density of individual domains. Hence, it is expected that the H_{inter} also diminished with increasing top $L1_0$-FePt thickness.

In the simulated trilayers with varying top $L1_0$-FePt thickness, the anisotropy of the top and bottom $L1_0$-FePt were kept constant at 1.31×10^7 erg/cm^3 and 8.48×10^6 erg/cm^3, respectively due to the different deposition temperatures of the layers and commensurate degree of $L1_0$ ordering. Both the $L1_0$-FePt layers were assumed to have an intralayer exchange field $H_{intra} = 35$ kOe. A small dispersion in the exchange field of 0.1 within (d_{intra}) and between (d_{inter}) both $L1_0$-FePt layers was

introduced The fraction of decoupled grains f_{intra} for the bottom $L1_0$-FePt and the fraction of decoupled grains between the $L1_0$-FePt layers f_{inter} were fixed at 0.01 and 0.8, respectively, representing the semi-continuous nature of the film in the bottom layer, and also the much weaker degree of coupling between the layers due to the addition of the spacer layer. The changes in the values of the f_{intra} for the top $L1_0$-FePt and the H_{inter} are summarized in Table 5.3. The values used in the model were determined after the optimization of the simulation system to achieve magnetic properties similar to the experimental hysteresis loops. The simulated PSVs with top $L1_0$-FePt thickness of 5, 10, 15 and 20 nm are henceforth referred as PSV-5, PSV-10, PSV-15 and PSV-20, respectively.

Table 5.3   Summary of the properties of the simulated trilayers with varying top $L1_0$-FePt thickness of 5, 10, 15 and 20 nm.

Simulated PSV	Top f_{intra}	H_{inter} (kOe)
PSV-5	0.4	5.00
PSV-10	0.3	2.25
PSV-15	0.2	1.50
PSV-20	0.1	1.20

Having considered the effects of film morphology on the magnetic parameters, the hysteresis behaviour of the various experimental PSVs in comparison to the modelling results are generated for the different hard layer thickness. Qualitatively the agreement between the simulation and experimental magnetization behaviour of the trilayers with varying top $L1_0$-FePt thickness was very good. The coercivities of the top hard ($\sim$ 10kOe) and bottom soft layers ($\sim$ 5 kOe) did not change

appreciably with varying top layer thickness, but the shape of the loop changed consistently for both simulation and experiment as the contribution of the top FePt layer to the total magnetization changed (Figure 5.19). However, it was observed that the coercivity of the simulated trilayers was twice that of the actual experimental measurement. The deviation was likely contributed by the disparity in the time dependent measurement of the simulated hysteresis loop, which was computed over a few nanoseconds, compared to the experiments where a longer measurement time allowed sufficient time for spin relaxation [27]. The most significant change in the hysteresis properties with increasing hard layer thickness was the reduction of the magnetic tail. For the PSV-5, the weak exchange coupling between the grains in the top FePt layer led to the formation of stable domains which required a large external field to flush out completely. For increasing top FePt layer thickness, the larger inter-grain exchange coupling helped to flush out these domains leading to a squarer loop.
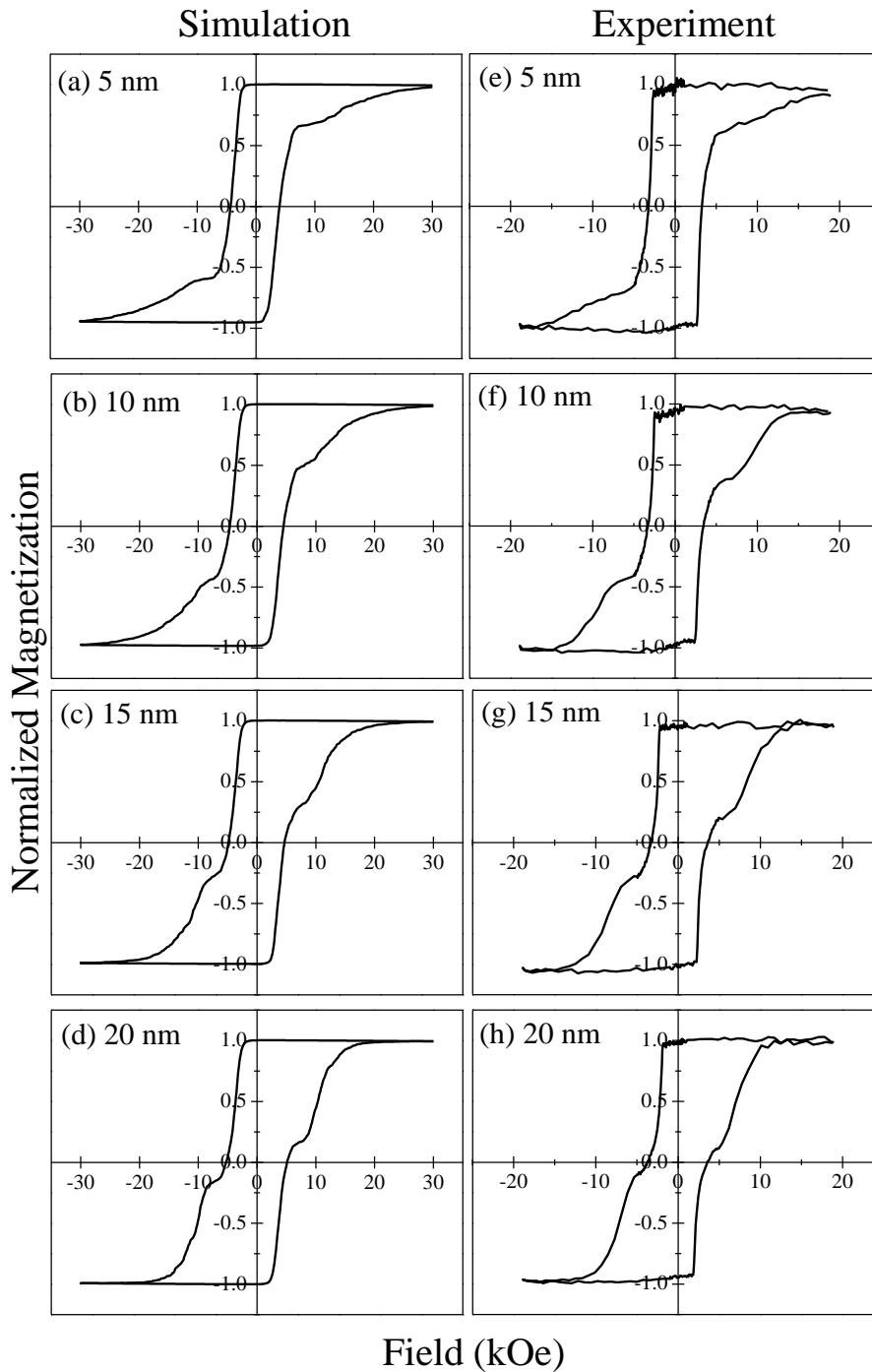
Figure 5.19 Out-of-plane simulated hysteresis loops for (a) PSV-5, (b) PSV-10, (c) PSV-15 and (d) PSV-20 and out-of-plane experimental hysteresis loops measured at room temperature with top $L1_0$-FePt thickness of (e) 5, (f) 10, (g) 15 and (h) 20 nm for the fabricated MgO/$L1_0$-FePt /TiN/$L1_0$-FePt PSVs.

In order to compare the magnetic states of the hard and soft layers during switching, the simulated magnetic configurations and experimental MFM images of the reversal behaviour of the individual layers with a top FePt layer thickness of 20 nm are presented in Figures 5.20 and 5.21. Reversal proceeded via the formation and

propagation of the reversed domains in both the simulated layers. Both the simulated and experimental results show good agreement in terms of the reversal mechanism, domain size and shape. Larger domain sizes were observed for the soft bottom layer in both the simulation and experiment [Figures 5.20(d) and (g)]. The larger domains formed for the bottom soft FePt were the result of more instantaneous reversal, reflected in its smaller SFD (Figure 5.19).
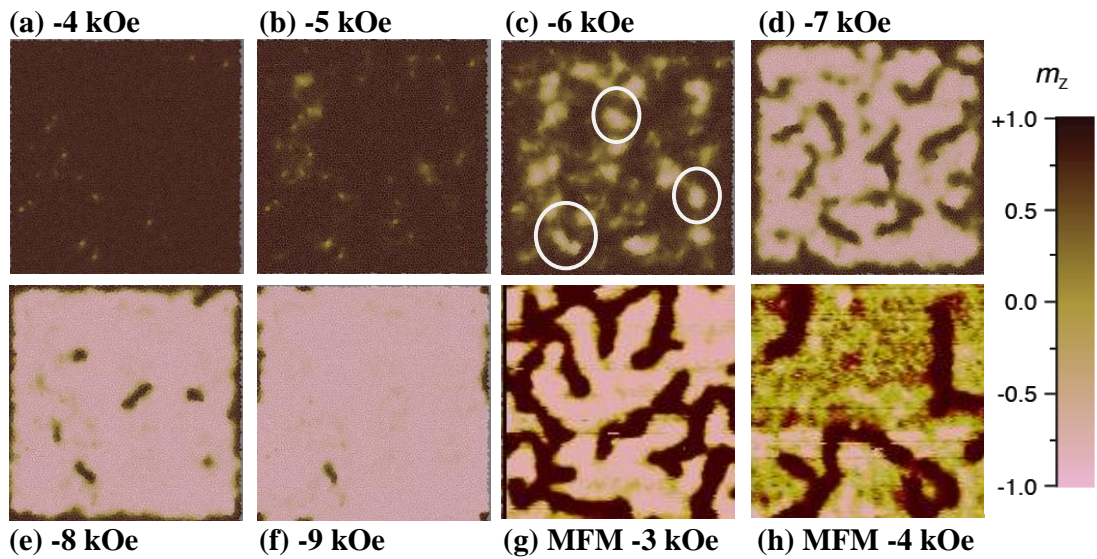
Figure 5.20 1.6 × 1.6 μm^2 simulated [(a)-(f)] and MFM [(g)-(h)] magnetization configurations of the soft bottom FePt layer at different points of the hysteresis curve, in the trilayer structure with top FePt thickness of 20 nm.

Figure 5.21 1.6 × 1.6 μm^2 simulated [(a)-(f)] and MFM [(g)-(h)] magnetization configurations of the hard top FePt layer at different points of the hysteresis curve, in the trilayer structure with top FePt thickness of 20 nm.

Smaller domain sizes were observed for the hard top FePt layer in both the simulation and experimental results [Figures 5.21(d) and (h)]. The smaller domain sizes for the hard top FePt was attributed, earlier in Section 5.1.3, to its higher anisotropy. This resulted in narrower domain wall widths which were more susceptible to pinning by defects formed within the top FePt layer. Thus, the impeded domain wall propagation led to smaller domain sizes in the hard top FePt layer. Despite the simulation model having assumed a defect free system, the same observation of smaller domain sizes was observed for the hard top FePt layer of PSV-20 all the same. As such, an additional contribution could be the influence of the strong demagnetization field on the larger anisotropy top FePt layer. At a field of -6 kOe, there were indications of local demagnetization within the top FePt initiated by stray fields emanating from the walls of the reversed domains within the soft bottom FePt [circled in Figures 5.20(c) and 5.21(a)], giving rise to the long magnetic tail towards negative saturation

Simulated magnetic configuration images for the FePt layers of PSV-5 are shown in Figures 5.22 and 5.23. The bottom and top FePt layers in PSV-5 followed the same reversal behaviour as that of PSV-20. However, the sizes of the reversed domains in the hard top FePt appeared smaller in PSV-5 than in PSV-20 (Figures 5.23 and 5.21). This was attributed to the greater extent of independent reversal present within the top FePt layer of PSV-5 where the grains were more decoupled due to its granular morphology. In addition, the thinner top FePt layer, made up of smaller grains, was more susceptible to the influence of dipolar stray field emitted from the reversed domain walls of the soft bottom FePt. This observation was made based on the fact that there existed more significant local reversal within the hard top FePt at the applied field of -6 kOe in PSV-5 [Figures 5.22(d) and 5.23(b)]

compared to PSV-20 [Figures 5.20(c) and 5.21(a)]. As such, the greater degree of local demagnetization within the thinner top FePt layer also contributed to the smaller reversed domain sizes compared to that in the thicker top FePt layer. At the same time, this also resulted in a far larger applied field required to bring about complete saturation of the 5 nm top FePt ($\sim$ 26 kOe) [Figure 5.23(h)] compared to that in 20 nm top FePt ($\sim$ 22 kOe) [Figure 5.21(f)].
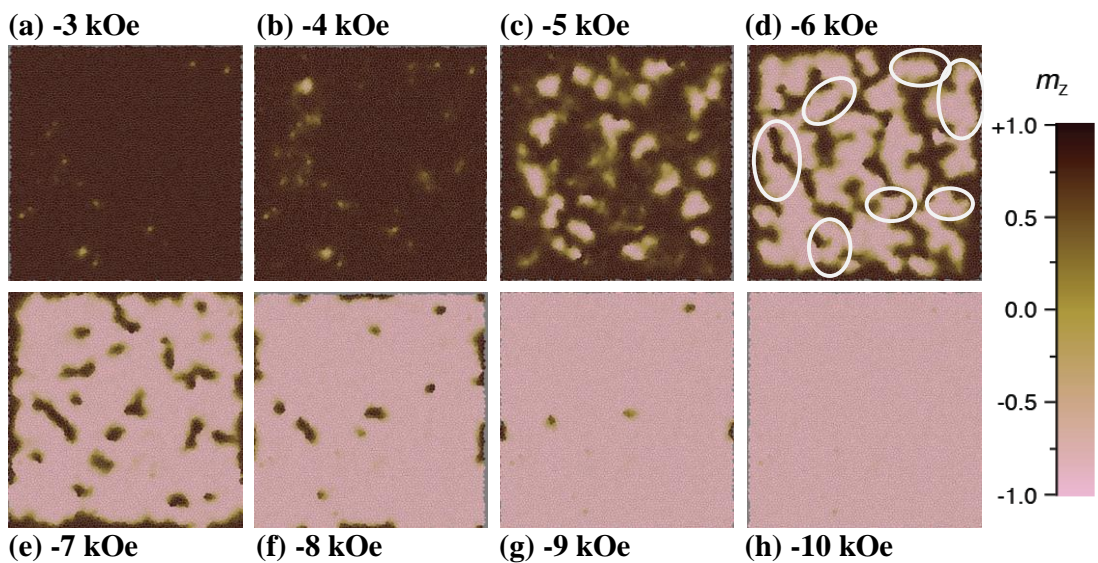
Figure 5.22 1.6×1.6 µm^2 simulated magnetization configurations of the soft bottom FePt layer at different points of the hysteresis curve, in the trilayer structure with top FePt thickness of 5 nm.
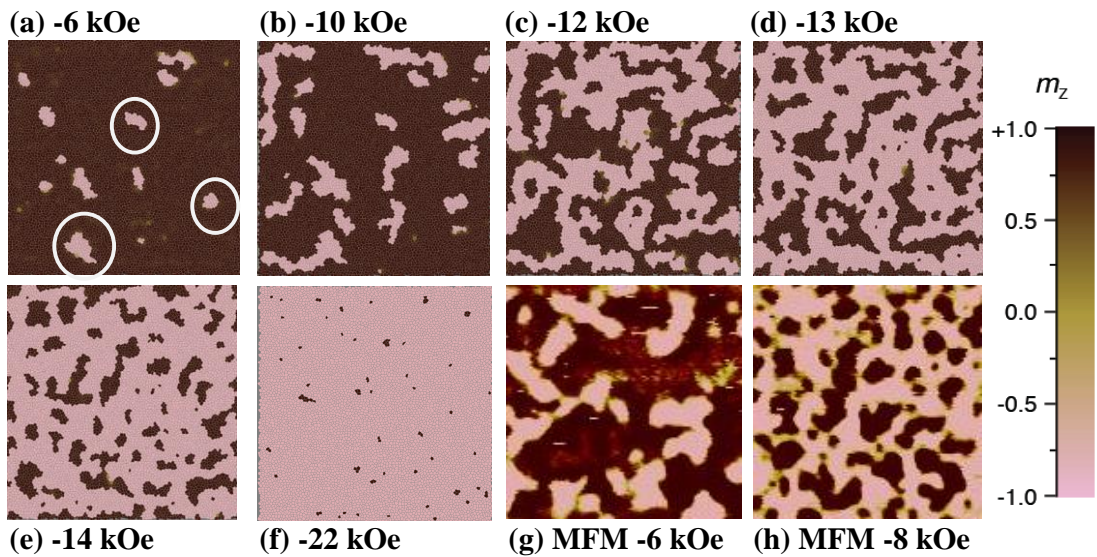

Figure 5.23 1.6×1.6 µm^2 simulated magnetization configurations of the hard top FePt layer at different points of the hysteresis curve, in the trilayer structure with top FePt thickness of 5 nm.

137
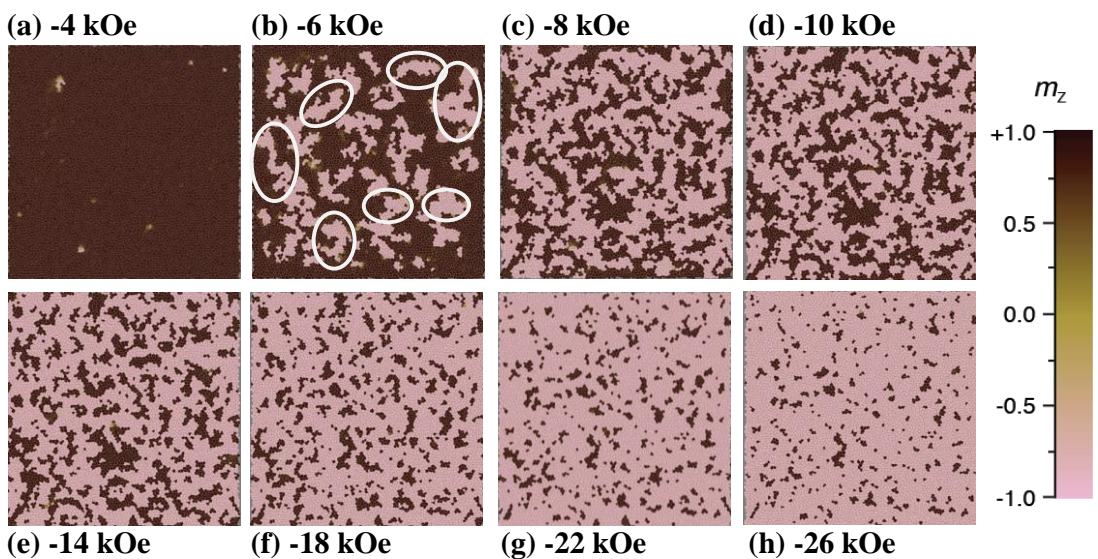
Figure 5.24 shows the simulated CPP fractional MR loops of the trilayer with varying top FePt thickness. Although CPP measurements of the MR were not carried out for the experimental PSVs, CIP measurements indicated the existence of GMR for the PSVs with thicker top FePt layer, as shown in Figure 5.16. The CPP fractional MR of the simulated trilayer was observed to decrease with a thinner top FePt thickness. This is in agreement with the measured MR trend (Figure 5.16), where the decline in GMR with the thinner top FePt layer was attributed to the lack of a continuous pathway for the spin dependent scattered electrons to be detected via the CIP measurement, as discussed in Section 5.2.
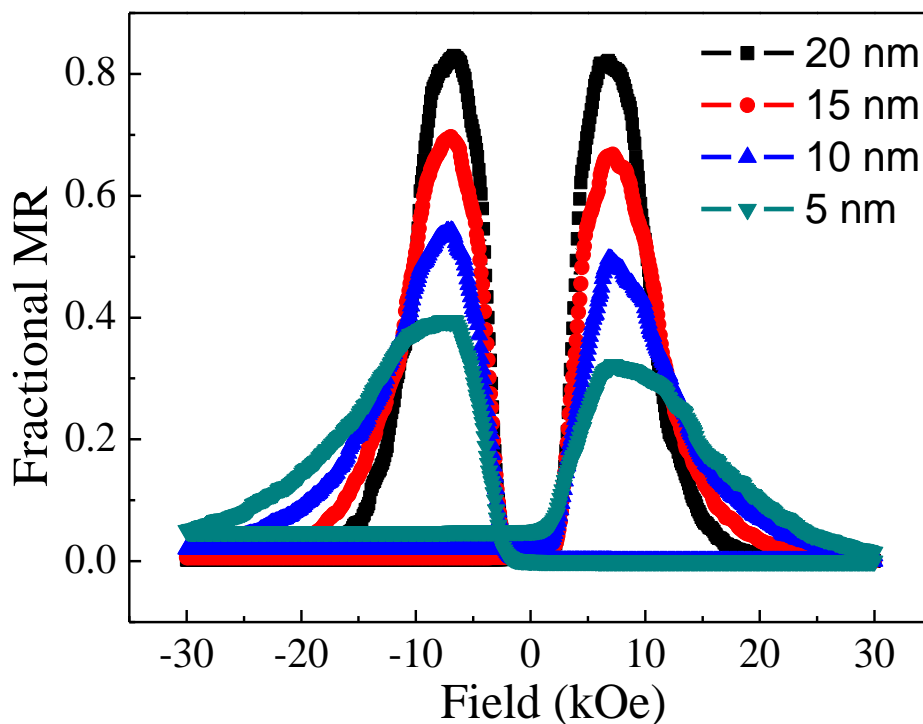
Figure 5.24 Simulated MR loops of the trilayer with varying top FePt thickness.

However, the effects of the continuity of electron percolation path were not taken into account in the CPP fractional MR calculation for the simulation, where the calculation of CPP fractional MR was carried out based on the angle made between the two adjacent top and bottom FePt grains. As such, the same MR trend observed

from the simulation results was an indication of another possible contribution. As discussed, the stray fields emitted from the soft bottom FePt layer brought about a magnetic tail and thus more significant local domain reversal in the thinner top FePt layer of PSV-5 compared to the thicker FePt layer of PSV-20. This resulted in a greater proportion of domains in both the bottom and top FePt layers of PSV-5 possessing parallel magnetization, thus bringing about a smaller fractional MR. As such, the simulation results suggest that dipolar stray field coupling presumably also contributed to the smaller GMR in the experimental PSV with a thinner top $L1_0$-FePt. Furthermore, the fact that the CPP MR calculations ignored the effects of continuity of the electron percolation pathway also led to the discrepancy with the measured CIP MR. In particular, for the PSV-5, there existed a non-evident CIP GMR (Figure 5.16) compared to the significantly larger CPP MR in the corresponding simulated trilayer

References

1. E. M. Ho, A. K. Petford-Long, and A. Cerezo, J. Magn. Magn. Mater. **192**, 431 (1999).

2. P. Ho, G. C. Han, R. F. L. Evans, R.W. Chantrell, G. M. Chow, and J. S. Chen, Appl. Phys. Lett. **98**, 132501 (2011).

3. S. K. Chen, F. T Yuan, and S. N. Shiao, IEEE Trans. Magn. **41**, 921 (2005).

4. H. H. Li, K. F. Dong, Y. G. Peng, G. Ju, G. M. Chow, and J. S. Chen, J. Appl. Phys. **110**, 043911 (2011).

5. Y. Tsuji, S. Noda, and S. Nakamura, J. Vac. Sci. Technol. B **29**, 031801 (2011).

6. S. Wiebel, J. P. Jamet, N. Vernier, A. Mougin, J. Ferre, V. Baltz, B. Rodmacq, and B. Dieny, Appl. Phys. Lett. **86**, 142502 (2005).

7. W. S. Lew, S. P. Li, L. Lopez-Diaz, D. C. Hatton, and J. A. C. Bland, Phys. Rev. Lett. **90**, 2172011 (2003).

8. L. Thomas, M. G. Samant, and S. S. P. Parkin, Phys. Rev. Lett. **84**, 1816 (2000).

9. D. Tripathy, A. O. Adeyeye, S. Shannigrahi, Phys. Rev. B **75**, 012403 (2007).

10. N. Thiyagarajah and S. Bae, J. Appl. Phys. **104**, 113906 (2008).

11. C. L Zha, Y. Y. Fang, J. Nogués, and J. Åkerman, J. Appl. Phys. **106**, 053909 (2009).

12. Y. Liu, D. J. Sellmyer, and D. Shindo, Hand Book of Advanced Magnetic Materials vol. 1, 199 (2006).

13. C. L. Lee, J. A. Bain, S. Chu, and M. E McHenry, J. Appl. Phys. **91**, 7113 (2002).

14. P. Bruno and C. Chappert, *Magnetism and Structure in Systems of Reduced Dimension*, edited by R. F. C. Farrow et al., (Plenum Press, New York, 1993), 389-399.

15. F. J. Himpsel, J. E. Ortega, G. J. Mankey, and R. F. Willis, Advances in Physics: Magnetic Nanostructures **47**, 511 (1998).

16. K. M. Seemann, V. Baltz, M. Mackenzie, J. N. Chapman, B. J. Hickey, and C. H. Marrows, Phys. Rev. B. **76**, 174435 (2007).

17. P. Ho, G. C. Han, G. M. Chow, J. S. Chen, Appl. Phys. Lett. **98**, 252503 (2011).

18. V. Baltz, A. Marty, B. Rodmacq, and B. Dieny, Phys. Rev. B **75**, 014406 (2007).

19. P. Allia, F. Celegato, M. Coisson, P. Tiberto, F. Vinai, F. Albertini, F. Casoli, and S. Fabbrici, J. Magn. Magn. Mater. **322**, 1898 (2010).

20. J. Yu, U. Rüdiger, A. D. Kent, R. F. C. Farrow, R. F. Marks, D. Weller, L. Folks, and S. S. P. Parkin, J. Appl. Phys. **87**, 6854 (2000).

21. A. P. Mihai, J. P. Attané, A. Marty, P. Warin, and Y. Samson, Phys. Rev. B **77**, 060401 (2008).

22. W. Tsai, M. Delfino, J. A. Fair, and D. Hodul, J. Appl. Phys. **73**, 4462 (1993).

23. Y. Liu, D. J. Sellmyer, and D. Shindo, Hand Book of Advanced Magnetic Materials vol. 1, 199 (2006).

24. E. Y. Tsymbal and D. G. Pettifor, " Perspective of Giant Magnetoresistance," in Solid State Physics, edited by H. Ehrenreich and F. Spaepen, Vol. 56 (Academic Press, 2001) pp. 113-237.

25. D. R. Lide, ed., CRC Handbook of Chemistry and Physics, 92th ed. (CRC Press, Boca Raton, FL, USA, 2009), Chap. 12, pp. 42.

26. T. Ambrose, and O. Mryasov, *Half-metallic Alloys Fundamentals and Applications*, edited by I. Galanakis, and P. H. Dederichs (Springer, Berlin, 2005), 206-210.

27. M. P. Sharrock, J. Appl. Phys. 76, 6413 (1994).

CHAPTER 6

6 ULTRA-THIN PMA $L1_0$-FePt BASED PSVs

Besides using PMA materials to reduce the STS critical current, a further method is to reduce the thickness of the PMA material. An ultra-thin free layer is desirable for STS as a reduction in the free layer volume brings about a decrease in the STS critical current. At the same time, the ultra-thin free layer is required to possess a sufficiently high PMA to ensure the non-volatility of the STT-MRAM. As covered in Chapter 1, materials such as $L1_0$-FePt and $[Co/Pd]_n$ multilayers are suitable candidates for the magnetic layers in the SVs and MTJs due to their high PMA. The PMA in $[Co/Pd]_n$ multilayers results from the hybridization of Co $3d$ and Pd $4d$ electrons at the Co/Pd interface [1, 2]. Thus, a large number of repeating units is required to give a high interfacial PMA in $[Co/Pd]_n$ multilayers. This deemed $[Co/Pd]_n$ multilayers to be a less suitable material, compared to $L1_0$-FePt, for fulfilling the ultra-thin free layer requirement in STT-MRAM. Earlier, K. Yakushiji demonstrated STS in ultra-thin FePt, with thickness in the range of 1.02 to 2.04 nm, for the PMA $L1_0$-FePt based SV [3]. The ultra-thin $L1_0$-FePt was fabricated using molecular beam epitaxial deposition of alternating $[Fe/Pt]_n$ multilayers. However, the use of the $[Fe/Pt]_n$ multilayer structure gives less stable magnetic properties which tend to fluctuate due to the interdiffusion of the Fe/Pt alternating layers [2]. An ultra-thin FePt alloy film will thus have an edge over the multilayer structures in this aspect but this has yet to be demonstrated. Earlier reports of $L1_0$-FePt SV structures illustrated the use of free $L1_0$-FePt alloy films with thickness in the range of 4 to 20 nm [4-8]. The fabrication and study of ultra-thin, continuous $L1_0$-FePt alloy films for the free layer is critical to reduce the J_c of

the STT-MRAM and makes it more viable for commercial applications. Chapter 6 focuses on the study of PSV structures which consist of an ultra-thin $L1_0$-FePt alloy free layer with thickness between 2 to 4 nm.

6.1 Properties of Ultra-Thin $L1_0$-FePt Film

Samples with the structure MgO (001) substrate/Fe (1 nm)/Pd (20 nm)/Pt (4 nm)/Fe (1 nm)/$L1_0$-FePt (t nm)/Ag (5 nm), with t varied between 1 to 4 nm, were fabricated to investigate the properties of a single ultra-thin $L1_0$-FePt alloy layer. Figure 6.1 shows the out-of-plane and in-plane hysteresis loops of the ultra-thin $L1_0$-FePt film with thickness varied from 1 to 4 nm. Table 6.1 summarizes the magnetic properties of these ultra-thin $L1_0$-FePt single layers with varying thickness. With increasing $L1_0$-FePt thickness, the PMA and thermal stability factor (TSF), $K_u V/k_B T$, of the ultra-thin $L1_0$-FePt layer increased. The thermal stability of the bit is critical for the maintenance of the non-volatility of the STT-MRAM, especially since the STT effect dominates only at small dimensions of less than 100 nm. A 10-year thermal stability criterion of greater than 60 is typically required. Assuming the scalability of the PSV to a diameter of 10 nm, these nanopillars with ultra-thin $L1_0$-FePt thickness of 2 to 4 nm possessed a TSF which surpassed the thermal stability criterion (Table 6.1). For the 1 nm $L1_0$-FePt, the squareness (S^*) and TSF were relatively low and hence only the properties of the PSVs with $L1_0$-FePt thickness of 2 to 4 nm would be further explored.
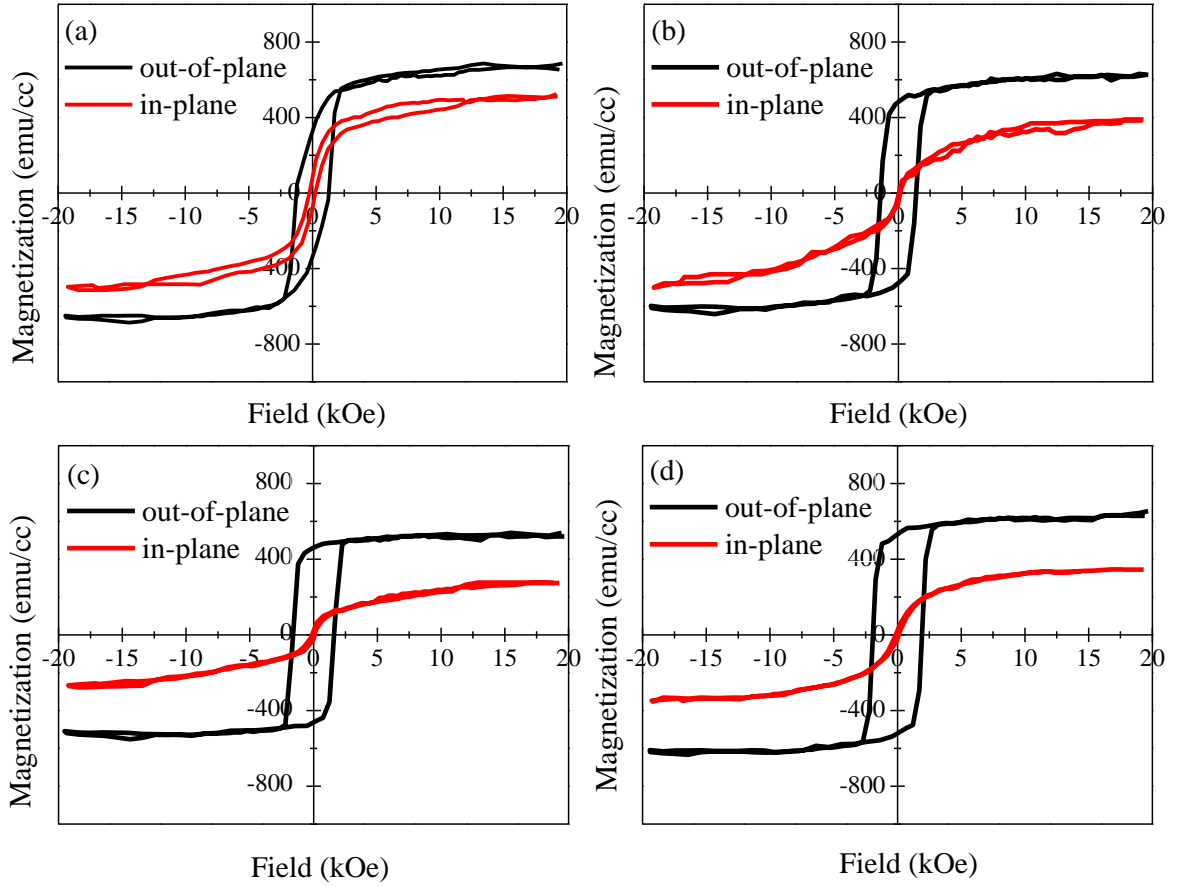
Figure 6.1   Out-of-plane and in-plane hysteresis loops of ultra-thin $L1_0$-FePt films with varying $L1_0$-FePt thickness of (a) 1, (b) 2, (c) 3 and (d) 4 nm.

Table 6.1.   Summary of the magnetic properties of the ultra-thin $L1_0$-FePt with thickness of 1, 2, 3 and 4 nm. Thermal stability factor (TSF) is defined by $K_u V/k_B T$, where K_u is the magnetic anisotropy, V is the volume of the free layer bit (assuming a device diameter of 10 nm), k_B is Boltzmann constant and T is temperature.

$L1_0$-FePt thickness (nm)	M_s (emu/cm^3)	K_u (10^7 erg/cm^3)	H_c (kOe)	S^*	TSF
1	675	2.06	1.34	0.51	39
2	614	2.21	1.43	0.81	84
3	532	2.50	1.67	0.89	142
4	611	2.89	1.92	0.87	219

6.2 PSVs with Ultra-Thin *L1*$_0$-FePt Film

PSVs with the structure Fe (1 nm)/Pd (20 nm)/Pt (4 nm)/Fe (1 nm)/*L1*$_0$-FePt (*u* nm)/Ag (5 nm)/[Co (0.3 nm)/Pd (0.8 nm)]$_{30}$/Pt (3 nm) were fabricated on single crystal (001)-textured MgO substrates, with *u* varied between 2 to 4 nm (Figure 6.2). In all of the samples, the Fe/Pd/Pt underlayers were deposited at 150 °C while the Fe/*L1*$_0$-FePt layers at 380 °C. The Ag spacer layer, [Co/Pd]$_{30}$ multilayer and the Pt capping layer were subsequently deposited at room temperature to minimize interlayer diffusion within the PSVs, in particular at the interfaces of the ferromagnets and spacer. The structural, crystallographic, magnetic, interfacial and spin transport properties of the PSVs with varying thickness of the ultra-thin *L1*$_0$-FePt alloy film will be studied in detail.

Pt	3 nm, RT
[Co/Pd]$_{30}$	33 nm, RT
Ag	5 nm, RT
FePt	*u* nm, 380 °C
Fe	1 nm, 380 °C
Pt	4 nm, 150 °C
Pd	20 nm, 150 °C
Fe	1 nm, 150 °C
MgO substrate	
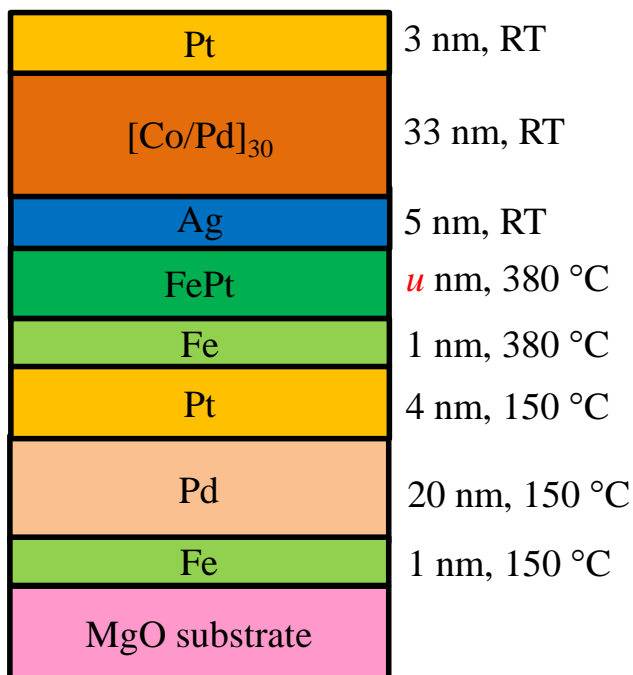
Figure 6.2 Schematic diagram of MgO/Fe/Pd/Pt/Fe/*L1*$_0$-FePt/Ag/CoPd/Pt PSV.

6.2.1 Crystallographic Properties

Figure 6.3 shows the XRD spectrums of the PSVs with varying $L1_0$-FePt thickness. In all the PSVs, a (002) texture was formed for the Pd bottom electrode. This served to promote the subsequent $L1_0$ ordering in the FePt, evident from the superlattice (001) and fundamental (002) $L1_0$-FePt peaks. The (001) and (002) FePt peaks became more prominent with increasing $L1_0$-FePt thickness due to a stronger signal from a thicker $L1_0$-FePt. (002) textured PMA [Co/Pd]$_{30}$ multilayer was also formed, induced by the growth of the (001) $L1_0$-FePt and (002) Ag spacer.
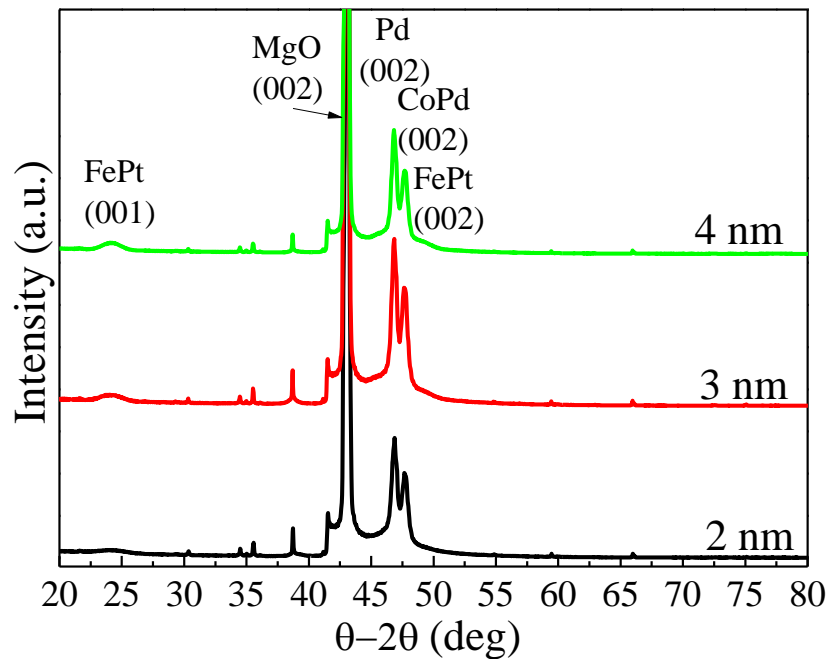
Figure 6.3 XRD spectrums of the PSVs with $L1_0$-FePt thickness of 2, 3 and 4 nm. The remaining unlabelled sharp peaks are inherent of the MgO substrate.

The cross-sectional HRTEM of the PSV with $L1_0$-FePt thickness of 4 nm (Figure 6.4 and inset) shows a crystalline growth of the (001) $L1_0$-FePt, (002) Ag spacer and (002) [Co/Pd]$_{30}$ multilayer. The white arrows (Figure 6.4 inset) highlight regions of mismatch at the $L1_0$-FePt/Ag interface which possibly arose due to the large lattice difference of 7.1 % between FePt and Ag.
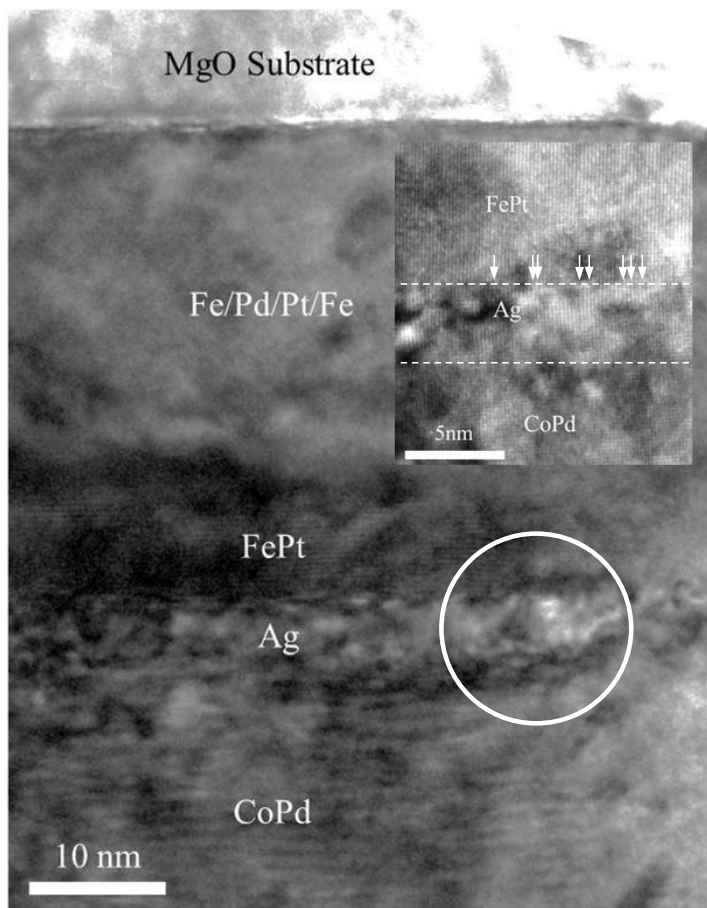
Figure 6.4 Cross-sectional HRTEM image of the MgO substrate/Fe/Pd/Pt/Fe/$L1_0$-FePt/Ag/[Co/Pd]$_{30}$ PSV with $L1_0$-FePt thickness of 4 nm. Inset indicates the magnified cross section of the circled region. Dashed lines in the inset represent the FePt/Ag and Ag/CoPd interfaces.

HRXRD was used to characterize and study the strain present in the multilayer PSV structure. The RSM combines the measurement of the interplanar spacing variations for the same orientation in the vertical l[001] direction, and a measurement of the orientation variations for the same interplanar spacing in the horizontal h[100] direction. The diffracted intensity distribution is represented by the signal in the out-of-plane k[010] direction. Figures 6.5 (a) to (c) represent the RSMs in the specular [001] direction, with the (002) MgO substrate taken as the reference.
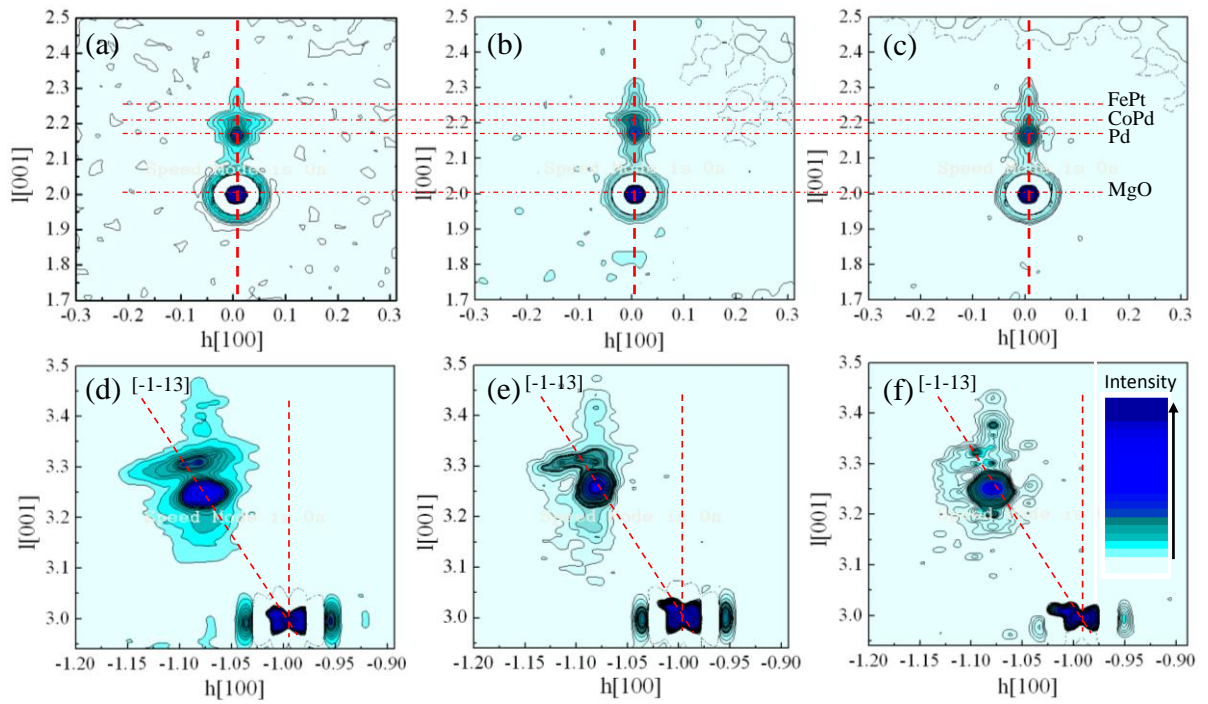
Figure 6.5   RSMs of the specular (002) reflections of MgO, Pd, CoPd and FePt in the PSVs with $L1_0$-FePt thickness of (a) 2, (b) 3 and (c) 4 nm. RSMs of the $(\bar{1}\,\bar{1}3)$ reflections of MgO, Pd and CoPd in the PSVs with $L1_0$-FePt thickness of (d) 2, (e) 3 and (f) 4 nm. The MgO (002) substrate was assigned to be the reference layer.

The strong reflection at the bottom of the RSMs was identified to be the (002) MgO substrate. In accordance with the XRD θ-2θ spectrum in Figure 6.3, the RSM intensity contour plots revealed a subsequent (002) Pd bottom electrode halo, followed by a CoPd reflection and a FePt reflection spot along the same vertical axis as the MgO substrate, where h[100] has the value of 0. Figures 6.5 (d) to (f) show the RSMs in the off-normal $(\bar{1}\,\bar{1}3)$ plane which provided a complete picture of the strain status of the multilayer PSVs. The reflections from the MgO substrate, Pd bottom electrode and [Co/Pd]₃₀ multilayer structure were similarly identified along the same $[\bar{1}\,\bar{1}3]$ direction, which had been extended from the origin of the reciprocal space. This suggested the presence of a fully relaxed Pd electrode and [Co/Pd]₃₀ multilayer [9]. The $L1_0$-FePt diffraction centre found between the $[\bar{1}\,\bar{1}3]$

and [001] directions indicated the presence of a partially strained $L1_0$-FePt layer. In addition, the diffraction of $[Co/Pd]_{30}$ was observed to become increasingly widely distributed in the direction perpendicular to the $[\bar{1}\,\bar{1}3]$ line. Such broadening suggests the increasing mosaicity in the $[Co/Pd]_{30}$ layer due to the angular variation in the $(\bar{1}\,\bar{1}3)$ plane [9]. With decreasing $L1_0$-FePt thickness, the $Ag/[Co/Pd]_{30}$ interface became rougher (Table 6.2) due to the Ag spacer being grown on a less continuous bottom $L1_0$-FePt. The increasingly rougher Ag surface could presumably have contributed to the larger variation in the orientation of the (002) CoPd diffraction.

Table 6.2.   Summary of the properties of the PSVs with ultra-thin $L1_0$-FePt thickness of 2, 3 and 4 nm.

$L1_0$-FePt thickness (nm)	R_{RMS} (nm)	H_{cfree} (kOe)	H_{chard} (kOe)	SFD_{free} (kOe)	SFD_{hard} (kOe)	Resistance (Ω)	GMR (%)
2	3.3	1.10	2.62	1.32	1.26	1.24	0.74
3	2.5	1.43	2.70	1.20	1.51	1.20	0.50
4	1.8	1.58	1.58	1.48	1.48	1.38	0.15

6.2.2 Magnetic Properties

Figure 6.6 shows the out-of-plane and in-plane hysteresis loops of the PSVs with varying $L1_0$-FePt thickness of 2 to 4 nm. Table 6.2 summarizes the magnetic properties of the $L1_0$-FePt and $[Co/Pd]_{30}$ layers in the PSVs. With increasing $L1_0$-FePt thickness, the anisotropy and coercivity of the $L1_0$-FePt increased. This was attributed to the improvement in the $L1_0$ ordering due to the increased volume fraction of the fct $L1_0$-FePt formed with a thicker $L1_0$-FePt. The absence of

independent reversal in the PSV with $L1_0$-FePt film thickness of 4 nm was attributed to the similarity in coercivities of the $L1_0$-FePt and $[Co/Pd]_{30}$ layers [Figure 6.6(c)]. With the reduction in $L1_0$-FePt film thickness, decoupling between the $L1_0$-FePt and $[Co/Pd]_{30}$ layers was observed [Figures 6.6(a) and (b)]. The softer $L1_0$-FePt and harder $[Co/Pd]_{30}$ acted as the free and fixed layer, respectively.
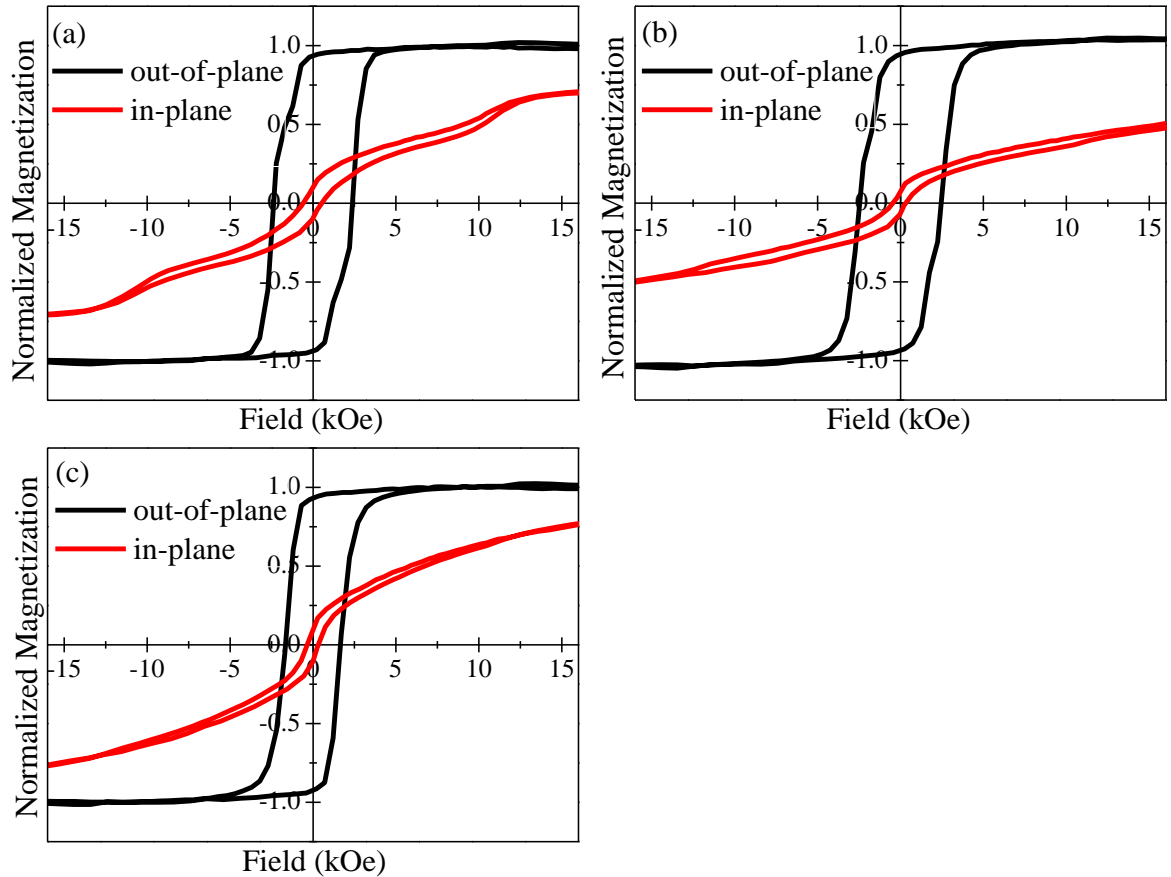
Figure 6.6   Out-of-plane and in-plane hysteresis loops of $L1_0$-FePt/Ag/$[Co/Pd]_{30}$ PSVs with $L1_0$-FePt thickness of (a) 2, (b) 3 and (c) 4 nm.

6.2.3 Current-in-Plane GMR

For the $L1_0$-FePt layer thickness of 4 nm, the absence of a distinct difference between the coercivities of the $L1_0$-FePt and $[Co/Pd]_{30}$ layers resulted in a persistently parallel configuration of the FM layers. As such, only a background MR which arose from the finite temperature effect was observed [Figure 6.7(c)]

[10]. The background MR contribution possessed a largest value of 0.15 % in the absence of an applied field. The MR gradually decreased with a larger applied field which eliminated the *s-d* electrons spin flipping disorder. With reduced *L*1$_0$-FePt thickness, a GMR was produced due to the formation of the parallel and anti-parallel configurations of the *L*1$_0$-FePt and [Co/Pd]$_{30}$ layers with applied field, which gave rise to the low and high resistance states, respectively [Figure 6.7(a) inset].
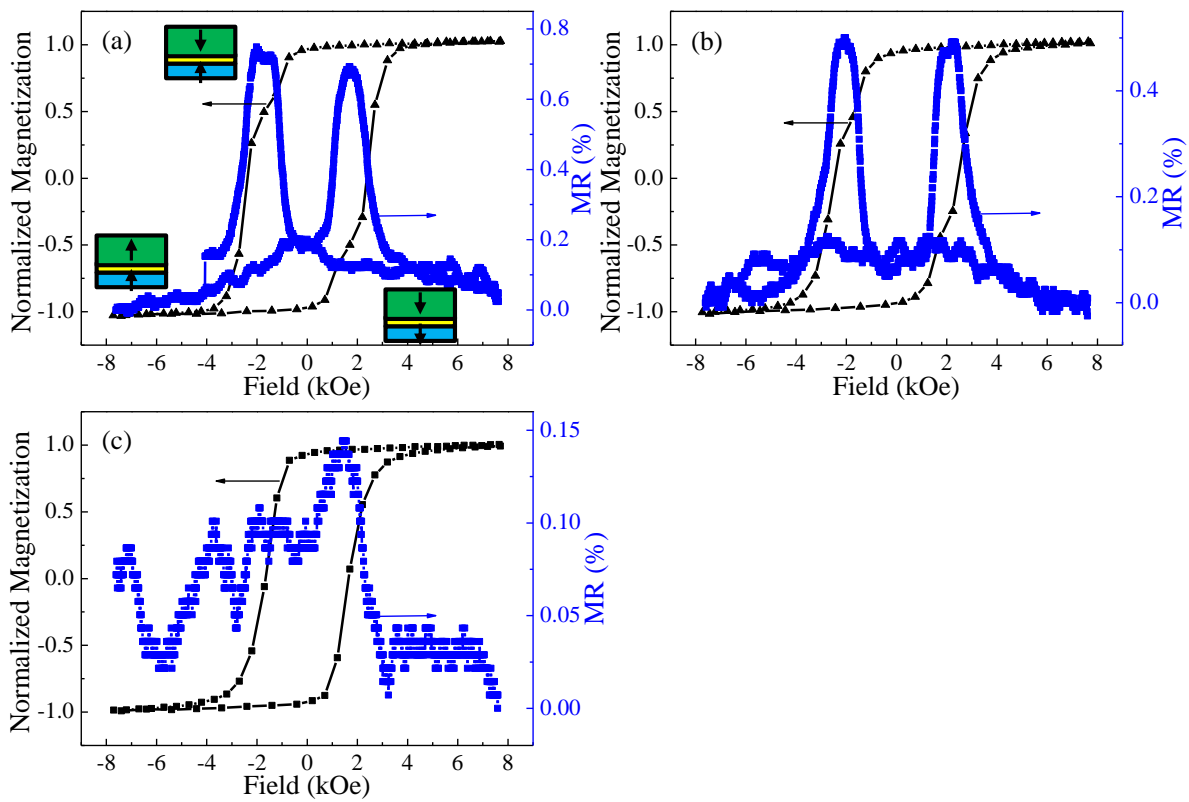
Figure 6.7 Out-of-plane magnetization and MR curves measured at room temperature for the PSVs with *L*1$_0$-FePt thickness of (a) 2, (b) 3 and (c) 4 nm.

First principles calculations of the band structures of FePt, Ag and Co were performed with CASTEP, using the density functional theory and plane-wave pseudopotential method. Figure 6.8 shows that near the Fermi energy level of 0 eV, both the band structures of FePt and Co spin up electrons displayed better band

compatibility with Ag, in terms of more similar energy and slope, compared to that of the FePt and Co spin down electrons [11]. As such, majority spin up electrons would be scattered less extensively compared to the spin down electrons at the FePt/Ag and Ag/Co interfaces, contributing to a larger transmission of majority spin up electrons across the interfaces. This reinforced that the GMR observed was attributed to the differential scattering of the spin up and spin down conduction electrons at the $L1_0$-FePt/Ag and Ag/Co interfaces of the PSVs.
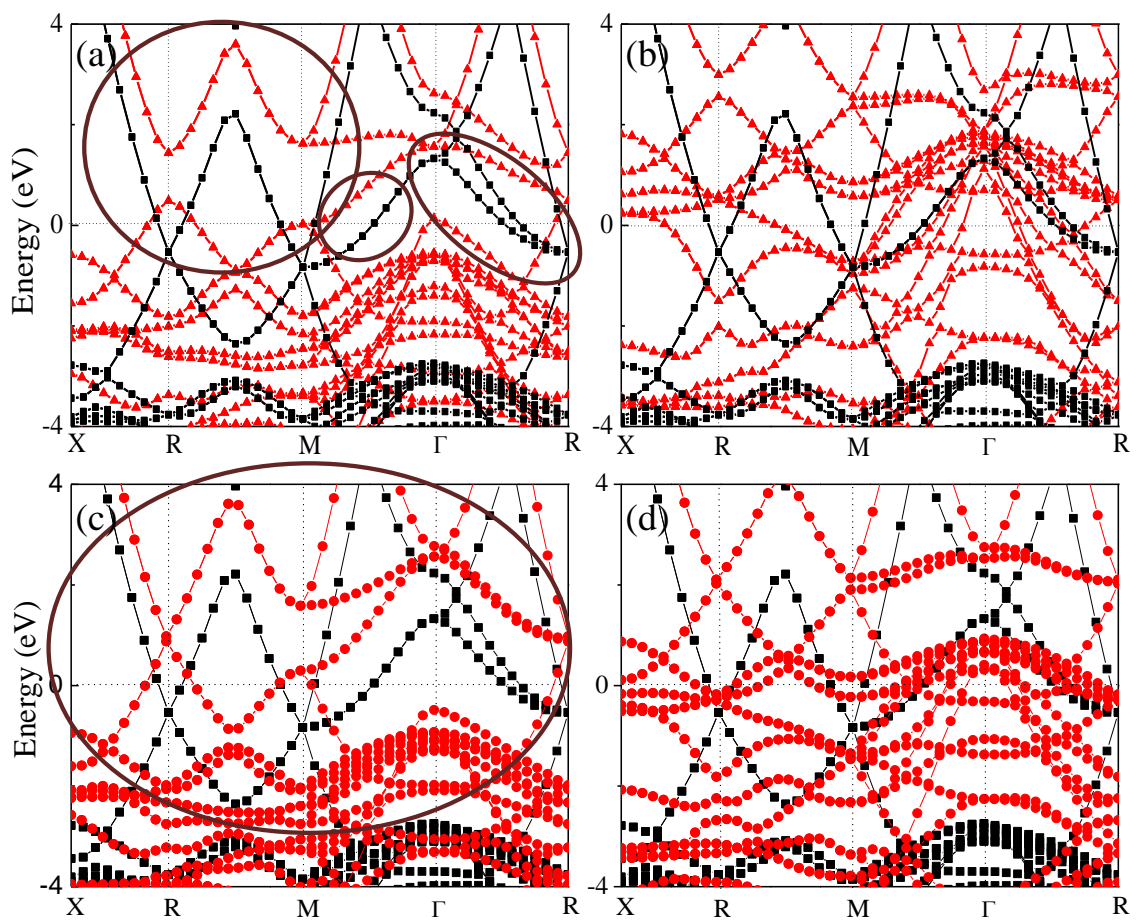
Figure 6.8   Energy bands for the Ag (■) and (a) spin up FePt (▲), (b) spin down FePt (▲), (c) spin up Co (●) and (d) spin down Co (●). Better band match is evident around the Fermi energy of Ag with spin up FePt band and Ag with spin up Co band structures.

In the parallel configuration, the majority spin up electrons passed through relatively easily, giving a low resistance state. In the anti-parallel configuration, the electrons in both channels were reflected at either one of the interfaces, producing

a higher resistance state. In addition, a positive GMR was observed since the surface and bulk spin asymmetries of the $L1_0$-FePt and $[Co/Pd]_{30}$ magnetic films possessed positive values, indicating that the majority spin electrons were less scattered within the layers and at the interfaces [12].

With a reduction in the $L1_0$-FePt layer thickness to 2 nm, the GMR increased to a highest value of 0.74 % (Table 6.2). This was attributed to a more decoupled PSV where there was a more distinct difference in the coercivities of the $L1_0$-FePt and $[Co/Pd]_{30}$ layers. A better decoupled PSV suggested a smaller extent of mutual influence between the spins of both FM layers, thereby allowing a greater proportion of spins to possess opposite magnetization. Another contribution could also be due to the smaller number of heavy Pt scattering centres present in the thinner FePt films, which reduced the extent of spin independent scattering [13].

References

1. B. N. Engel, C. D. England, R. A. Van Leeuwen, M. H. Wiedmann, and C. M. Falco, Phys. Rev. Lett. **67**, 1910 (1991).

2. C. S. E, J. Rantschler, S. S. Zhang, S. Khizroev, T. R. Lee, and D. Litvinov, J. Appl. Phys. **103**, 07B510 (2008).

3. K. Yakushiji, S. Yuasa, T. Nagahama, A. Fukushima, H. Kubota, T. Katayama, and K. Ando, Appl. Phys. Express **1,** 041302 (2008).

4. T. Seki, S. Mitani, K. Yakushiji, and K. Takanashi, Appl. Phys. Lett. **89**, 172504 (2006).

5. A. P. Mihai, J. P. Attané, L. Vila, C. Beigné, J. C. Pillet, and A. Marty, Appl. Phys. Lett. **94**, 122509 (2009).

6. C. L. Zha, J. Persson, S. Bonetti, Y. Y. Fang and J. Akerman, Appl. Phys. Lett. **94**, 163108 (2009).

7. P. Ho, G. C. Han, R. F. L. Evans, R. W. Chantrell, G. M. Chow, and J. S. Chen, Appl. Phys. Lett. **98**, 132501 (2011).

8. P. Ho, G. C. Han, K. H. He, G. M. Chow, and J. S. Chen, Appl. Phys. Lett. **99**, 252503 (2011).

9. G. V. Hansson, H. H. Radamsson, and W. X. Ni, J. Mater. Sci: Materials in Electronics **6**, 292 (1995).

10. J. Yu, U. Rüdiger, A. D. Kent, R. F. C. Farrow, R. F. Marks, D. Weller, L. Folks, and S. S. P. Parkin, J. Appl. Phys. **87**, 6854 (2000).

11. T. Ambrose, and O. Mryasov, *Half-metallic Alloys Fundamentals and Applications*, edited by I. Galanakis, and P. H. Dederichs (Springer, Berlin, 2005), 206-210.

12. J. Barnas, A. Fert, M. Gmitra, I. Weymann, and V. K. Dugaev, Phys. Rev. B. **72,** 024426 (2005).

13. A. D. Kent, Nature Materials **9**, 699 (2010).

CHAPTER 7

7   CONCLUSIONS AND RECOMMENDATIONS

In recent years, research focus has shifted towards the utilization of STT as a means to induce magnetization reversal in MRAM. High PMA materials are required for STT-MRAM as they allow the maintenance of thermal stability, with a miniaturization of the device, to fulfill the higher areal density requirement. Another advantage is its ability to reduce the critical current density required for spin transfer switching. In this thesis, work carried out on the high PMA $L1_0$-FePt as a potential candidate for STT-MRAM has been described. The major findings are summarized in Sections 7.1 to 7.3.

7.1 $L1_0$-FePt PSV with Ag spacer

Chapter 4 described the $L1_0$-FePt based PSV system with Ag spacer. A highest GMR of 1.1 and 2.2 % was achieved at room temperature and 77 K, respectively. This proved to be a significant improvement from the use of Au, Pt and Pd spacer materials reported earlier. Ag is of a smaller atomic number and thus depolarizes the spins to a smaller extent compared to the other spacer materials. The effects of diffusion within the PSV due to high temperature processes such as post-annealing were detrimental to the performance of the PSV. Increased interlayer diffusion resulted in stronger interlayer coupling between the $L1_0$-FePt layers. This prevented the independent reversal of the $L1_0$-FePt layers, a pre-requisite to produce a significant GMR. Both the atomistic model and micromagnetic bilayer model which utilized the LLG and LLB equation, respectively, also affirmed the damaging effects of interlayer diffusion on the PSV system.

7.2 $L1_0$-FePt PSV with TiN spacer

The recognition that interlayer diffusion within the PSV must be minimized for enhanced GMR performance led to the introduction of the TiN spacer for the $L1_0$-FePt based PSV system, as covered in Chapter 5. The interlayer diffusion was effectively minimized with the use of the metallic TiN spacer, which has the desirable qualities of being chemically stable towards FePt and good diffusion barrier properties. However, the highest GMR of 0.78 % obtained for the PSV with TiN spacer was slightly lower than that of the Ag spacer. This was attributed to the larger resistivity of TiN compared to Ag, which led to a greater extent of spin independent scattering. At the same time, the poorer band structure compatibility between TiN and $L1_0$-FePt in contrast to Ag and $L1_0$-FePt resulted in a smaller scattering spin asymmetry for TiN with FePt. Chapter 5 also illustrated a micromagnetic trilayer model, a build-up from the micromagnetic bilayer model to include the physical presence of the spacer. Theoretically simulated results from the micromagnetic trilayer model showed very good agreement with experimental observations made of the $L1_0$-FePt/TiN/$L1_0$-FePt PSVs.

7.3 PSV with Ultra-Thin $L1_0$-FePt

In line with the requirement for an ultra-thin free layer in STT-MRAM, where a reduction in the free layer volume brings about a reduction in the STT switching critical current, Chapter 6 demonstrated the PSVs with $L1_0$-FePt of ultra-thin (< 4 nm) thickness. PMA $L1_0$-FePt/Ag/[Co$_3$Pd$_8$]$_{30}$ PSV, with ultra-thin $L1_0$-FePt alloy free layer possessing high PMA (> 2.1×10^7 erg/cm^3) and thermal stability (> 84), were successfully fabricated. The selection of room temperature grown Co/Pd multilayer as the top electrode also ensured minimal interlayer diffusion at the

interfaces of the FM layers and spacer. The PSV with ultra-thin $L1_0$-FePt free layer displayed a highest GMR of 0.74 %.

7.4 Recommendations for Future Work

As discussed in Section 1.5.4, one of the key challenges faced by STT-MRAM is the persistently high STT critical current density which remains in the range of 10^6 -10^7 A/cm^2. This makes STT-MRAM unrealistic for practical usage due to overheating and high power consumption. Recently, it has been reported that the application of an external electric field to assist STT has immense potential in overcoming this issue, thus shaping the prospects of ultra-low energy switching in STT-MRAM devices [1-3]. This concept of electric field assisted reversible STT switching was first demonstrated in perpendicular anisotropy CoFeB/MgO/CoFeB MTJs, where the magnetic anisotropy and coercivity of the ferromagnetic CoFeB layer were reduced with a negative bias voltage supplied by a battery [2]. This enabled the magnetic configuration of the CoFeB layer to be switched by STT at a much smaller J_c, resulting in a reduction of 100 times from the range of 10^6 to 10^4 A/cm^2. Y. Shiota *et al.* also showed that by applying a voltage pulse to the CoFe/MgO/Fe MTJ, a reduced J_c of 1.1×10^5 A/cm^2 was realized [3]. Future work should be geared towards the study of an electric field assisted reversible switching in $L1_0$-FePt MTJs as a means to realize ultra-low power STT-MRAM devices. As mentioned in Section 1.5.6, the $L1_0$-FePt ferromagnet is a favourable candidate for memory devices as it offers a high PMA of 10^7 erg/cm^3, as compared to CoFeB and CoFe (10^6 erg/cm^3), consequently allowing a greater extent of miniaturization of the bit while maintaining a stronger thermal stability. At the same time, the TMR signal attained from the $L1_0$-FePt/MgO/$L1_0$-FePt MTJ is comparable to that in the CoFeB based MTJs, which makes $L1_0$-FePt an equally competitive candidate in

terms of the strength of the reading signal in STT-MRAM. In addition, the ultra-thin $L1_0$-FePt layer has been reported to exhibit voltage induced alteration of its magnetic anisotropy and coercivity, which gives hope for the realization of electric field induced reduction of J_c in $L1_0$-FePt STT-MRAM [4-6]. An electric field assisted reversible switching in $L1_0$-FePt MTJ promises the combined characteristics of high MR signal, low J_c and sufficiently high thermal stability with high areal density, and would thus be a breakthrough for the STT-MRAM.

While $L1_0$-FePt is set to be a potential candidate for next generation STT-MRAM, there are several concerns of this material which have to be addressed. The high deposition temperature or post annealing temperature required of high PMA $L1_0$-FePt alloy affects the MR performance and is one of the main disadvantages for the MRAM. The metastable $L1_1$-CoPt alloy phase, which is formed with a Co:Pt composition of 50:50 at% at a temperature range of 250 – 300 °C, could be an alternative alloy to be explored due to its lower deposition temperature requirements compared to $L1_0$-FePt. The alternately stacked close-packed atomic planes of Co and Pt normal to the (111) plane provides the high PMA of approximately 4×10^7 erg/cm^3. However, a systematic optimization of the alloy composition and fabrication temperature is necessary to achieve a complete growth of the $L1_1$-CoPt phase as any slight deviation in conditions will result in the formation of the A1 fcc disordered or $L1_0$-CoPt phase.

Another teething issue with the use of high PMA $L1_0$-FePt alloys lies in the poor spin transport characteristics. The heavy element Pt in the alloys leads to strong spin orbit scattering which results in spin flip, thus giving rise to poorer MR performance. The poor MR can be addressed with the use of a band structure compatible non-metallic spacer or the addition of spin polarizer layers such as Fe,

CoFe and CoFeB. However, the diffusion of Pt into the polarizer, due to the elevated deposition temperatures, will also be a cause of concern.

The fabrication of the $L1_0$-FePt based PSVs/MTJs into useful working devices is essential for the study of the STT switching and CPP MR behaviour of the $L1_0$-FePt based PSVs/MTJs. As such, another important aspect of the future work lies in the development of a simple and reliable fabrication process for micro to nano-scale $L1_0$-FePt based CPP/STT devices grown on MgO substrates. The conventional fabrication method for devices with the structure of bottom metal electrode/MR cell/top metal electrode typically requires one cycle of lithography and dry-etch procedures for every layer. This is a challenging process marked with high failure rates due to the multiple steps involved. The development of a simple process with shortened fabrication steps and minimal transfer defects is very much needed. The crossbar design, involving a simple two-step method of forming the top and bottom electrodes, allows the easy creation of $L1_0$-FePt based PSVs/MTJs rectangular devices of various dimensions (Figure 7.1). This proposed fabrication process reduces the processing steps to merely two cycles of lithography and dry-etch procedures. An outline of the simple fabrication process has been proposed for future study.
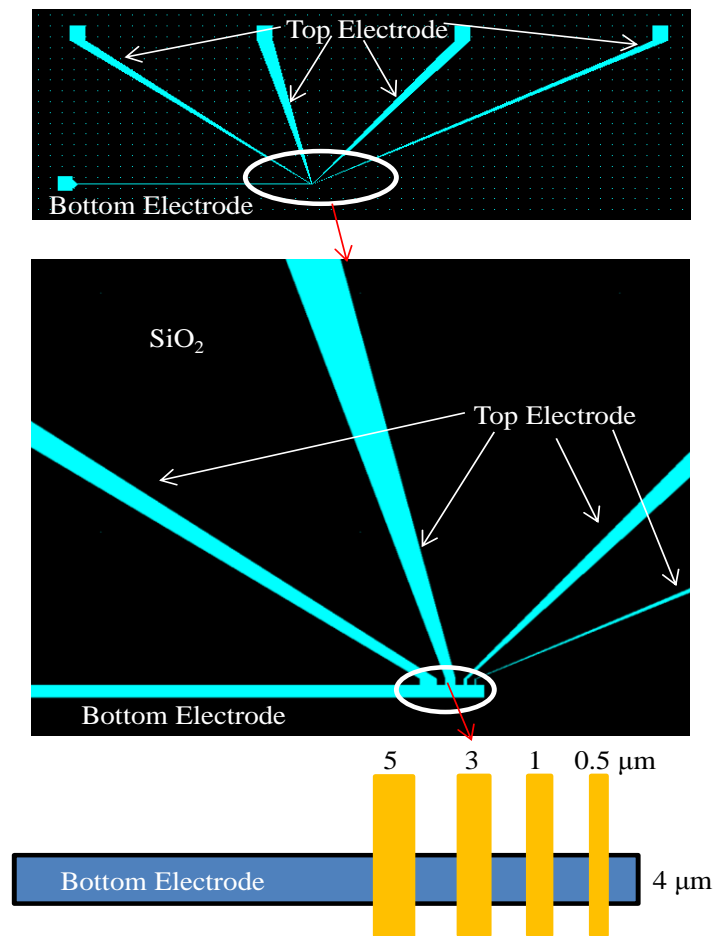
Figure 7.1 Schematic illustration of the crossbar with sensor of varying dimensions 0.5, 1, 3 and 5 $\times$ 4 μm^2 at the point of intersection.

The device fabrication involving the two-step crossbar fabrication is described as follows (Figure 7.2).

Step 1: Bottom Electrode Fabrication [From Figures 7.2(a) to (b)]

1) Soft bake at 100 ˚C for 1 ' on hotplate and cool for 1 '.

2) Spin coat with negative resist maN-2402 at 3000 rpm for 60 ".

3) Soft bake at 100 ˚C for 1 ' on hotplate and cool for 1 '.

4) EBL to create bottom electrode pattern.

5) Soft bake at 100 ˚C for 1 ' on hotplate and cool to room temperature.

6) Develop using ma-D525 for 90 ", rinse with water and dry blow with N_2.

7) Ion mill till MgO substrate and in-situ deposit SiO_2 to refill ion-milled regions.

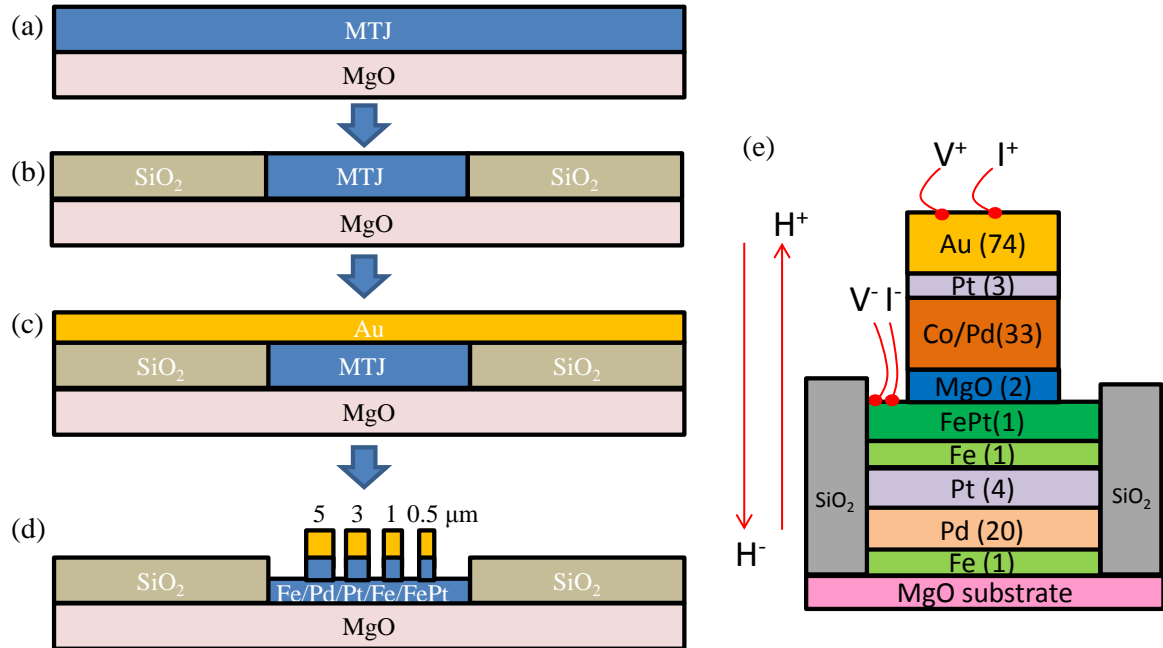8) Lift-off using PG removal, rinse with water and dry blow with N_2.

Figure 7.2 (a)-(d) Schematic illustrations of the bottom and top electrode crossbar fabrication process and (e) CPP measurement.

Step 2: Top Electrode Fabrication [From Figures 7.2(c) to (d)]

1) Cover alignment marks with tape, deposit 64 nm Au.

2) Remove tape to expose alignment marks, deposit Au 10 nm.

3) Soft bake at 100 °C for 1 ' on hotplate and cool for 1 '.

4) Spin coat with negative resist maN-2402 at 3000 rpm for 60 ".

5) Soft bake at 100 °C for 1 ' on hotplate and cool for 1 '.

6) EBL to create top electrode pattern.

7) Soft bake at 100 ˚C for 1 ' on hotplate and to room temperature.

8) Develop using ma-D525 for 60 ", rinse with water and dry blow with N_2.

9) Extend bottom electrode and top electrode pads manually with resist (marker) and ion mill beyond MgO spacer to $L1_0$-FePt layer.

10) Lift-off using PG removal, rinse with water and dry blow with N_2.

References

1.   T. Nozaki, Y. Shiota, S. Miwa, S. Murakami, F. Bonell, S. Ishibashi, H. Kubota, K. Yakushiji, T. Saruya, A. Fukushima, S. Yuasa, T. Shinjo, and Y. Suzuki, Nature Physics **8**, 491 (2012).

2.   W. G. Wang, M. Li, S. Hageman, and C. L. Chien, Nature Materials **11**, 64 (2011).

3.   Y. Shiota, S. Miwa, T. Nozaki, F. Bonell, N. Mizuochi, T. Shinjo, H. Kubota, S. Yuasa, and Y. Suzuki, Appl. Phys. Lett. **101**, 102406 (2012).

4.   M. Weisheit, S. Fahler, A. Marty, Y. Souche, C. Poinsignon, and D. Givord, Science **315**, 349 (2007).

5.   T. Seki, M. Kohda, J. Nitta, and K. Takanashi, Appl. Phys. Lett. **98**, 212505 (2011).

6.   M. Tsujikawa, and T. Oda, Phys. Rev. Lett. **102**, 247203 (2009).